Copyright Warning & Restrictions

The copyright law of the United States (Title 17, United States Code) governs the making of photocopies or other reproductions of copyrighted material.

Under certain conditions specified in the law, libraries and archives are authorized to furnish a photocopy or other reproduction. One of these specified conditions is that the photocopy or reproduction is not to be "used for any purpose other than private study, scholarship, or research." If a, user makes a request for, or later uses, a photocopy or reproduction for purposes in excess of "fair use" that user may be liable for copyright infringement,

This institution reserves the right to refuse to accept a copying order if, in its judgment, fulfillment of the order would involve violation of copyright law.

Please Note: The author retains the copyright while the New Jersey Institute of Technology reserves the right to distribute this thesis or dissertation

Printing note: If you do not wish to print this page, then select "Pages from: first page # to: last page #" on the print dialog screen

ABSTRACT

III-NITRIDE NANOSTRUCTURES: PHOTONICS AND MEMORY DEVICE APPLICATIONS

by
Barsha Jain

III-nitride materials are extensively studied for various applications. Particularly, III-nitride-based light-emitting diodes (LEDs) have become the major component of the current solid-state lighting (SSL) technology. Current III-nitride-based phosphor-free white color LEDs (White LEDs) require an electron blocking layer (EBL) between the device active region and *p*-GaN to control the electron overflow from the active region, which has been identified as one of the primary reasons to adversely affect the hole injection process. In this dissertation, the effect of electronically coupled quantum well (QW) is investigated to reduce electron overflow in the InGaN/GaN dot-in-a-wire phosphor-free white LEDs and to improve the device performance. With the incorporation of electronically coupled quantum well, it is demonstrated that light output power and external quantum efficiency (EQE) are increased, and efficiency droop is reduced. It is attributed to the significant reduction of electron overflow primarily responsible for efficiency degradation through the near-surface GaN region. In addition, a blue-emitting InGaN QW is incorporated between the quantum dot (QD) active region and *p*-GaN, wherein electrons escaping from the device active region can recombine with holes to contribute to white-light emission.

Moreover, different device design approaches are presented in this dissertation to mitigate the electron overflow in AlGaN deep ultraviolet (DUV) LEDs. A novel EBL-based LED structure is demonstrated instead of conventional EBL-based LED which

shows enhancement in the output power by ~3.5 times at 254 nm wavelength. Additionally, another novel approach is presented to mitigate the electron overflow problem in AlGaN DUV LEDs using concave quantum barriers (QBs) instead of conventional QBs. These concave QB structures are favorable for cooling down the hot electrons before entering into the QWs thus achieving lower velocity and mean free path, and resulting in remarkably reduced electron leakage. Further, an EBL-free approach is demonstrated to improve the performance of the AlGaN DUV LEDs at ~284 nm wavelength. The proposed LED design provides the solution for the electron leakage problem and opens a new path for the realization of high-power UV light emitters. Next, another III-nitride material-based UV LED has been studied which is relatively unexplored though it holds the potentiality and optical tuning capability from UV to infrared region. In particular, a detailed study of the light extraction efficiency (LEE) of AlInN nanowires in the UV wavelength range is performed using the three-dimensional finite-difference time-domain (FDTD) simulation method. Here the improvement in the EQE of AlInN based UV nanowire LEDs is demonstrated by enhancing the LEE using a periodic array of nanowires and different photonic crystal structures.

Consequently, resistive switching capabilities of AlN-based resistive random-access memory (RRAM) devices are investigated and demonstrated in this dissertation. The results suggest that AlN-based RRAM devices can be utilized for low power applications due to the switching capabilities at a very low compliance current (CC) of 10 nA.

III-NITRIDE NANOSTRUCTURES: PHOTONICS AND MEMORY DEVICE APPLICATIONS

by
Barsha Jain

A Dissertation
Submitted to the Faculty of
New Jersey Institute of Technology
in Partial Fulfillment of the Requirements for the Degree of
Doctor of Philosophy in Electrical Engineering

Helen and John C. Hartmann Department of
Electrical and Computer Engineering

December 2021

APPROVAL PAGE

III-NITRIDE NANOSTRUCTURES: PHOTONICS AND MEMORY DEVICE APPLICATIONS

Barsha Jain

Dr. Hieu Pham Trung Nguyen, Dissertation Advisor — Date
Associate Professor of Electrical and Computer Engineering, NJIT

Dr. Marek Sosnowski, Committee Member — Date
Professor of Electrical and Computer Engineering, NJIT

Dr. Dong-Kyun Ko, Committee Member — Date
Associate Professor of Electrical and Computer Engineering, NJIT

Dr. Xuan Liu, Committee Member — Date
Associate Professor of Electrical and Computer Engineering, NJIT

Dr. Eon Soo Lee, Committee Member — Date
Associate Professor of Mechanical and Industrial Engineering, NJIT

BIOGRAPHICAL SKETCH

Author: Barsha Jain

Degree: Doctor of Philosophy

Date: December 2021

Undergraduate and Graduate Education:

- Doctor of Philosophy in Electrical Engineering,
  New Jersey Institute of Technology, Newark, NJ, 2021

- Master of Technology in Computer Science and Engineering,
  ABV Indian Institute of Information Technology and Management,
  Gwalior, MP, India, 2017

- Bachelor of Technology in Electronics and Communication Engineering,
  Biju Patnaik University of Technology, Rourkela, Odisha, India, 2014

Major: Electrical Engineering

Presentations and Publications:

Peered Reviewed Papers:

B. Jain, R. T. Velpula, M. Patel, and H. P. T. Nguyen, "Controlled carrier mean free path for the enhanced efficiency of III-nitride deep-ultraviolet light-emitting diodes," *Applied Optics*, vol. 60, no. 11, pp. 3088-3093, 2021.

B. Jain, R. T. Velpula, H. Q. T. Bui, M. Patel, S. Md. Sadaf, and H. P. T. Nguyen, "Improved performance of electron blocking layer free AlGaN deep ultraviolet light-emitting diodes using graded staircase barrier," *Micromachines*, vol. 12, no. 3, p. 334, 2021.

B. Jain, R. T. Velpula, M. Patel, and H. P. T. Nguyen, "High performance electron blocking layer free ultraviolet light-emitting diodes," *Proceedings of SPIE*, p. 11680, 2021.

R. T. Velpula, **B. Jain**, T. R. Lenka, and H. P. T. Nguyen, "Polarization engineered III-nitride deep-ultraviolet light-emitting diodes for the enhanced carrier transport," Accepted *in Journal of Electronic Materials*.

R. T. Velpula, **B. Jain**, T. R. Lenka, and H. P. T. Nguyen, "Controlled electron leakage in electron blocking layer free InGaN/GaN nanowire light-emitting diodes," *Facta Universitatis, Series: Electronics and Energetics*, vol. 34, no. 3, pp. 393-400, 2021.

M. Patel, **B. Jain**, R. T. Velpula, and H. P. T. Nguyen. "Effect of HfO_2 passivation layer on light extraction efficiency of AlInN nanowire ultraviolet light-emitting diodes," *ECS Transactions*, vol. 102, no. 3, pp. 35-42, 2021.

R. Singh, R. T. Velpula, **B. Jain**, T. H. Q. Bui, H. P. T. Nguyen, and T. R. Lenka, "A novel $\beta - Ga2O3$ HEMT with f_T of 166 GHz and X-band POUT of 2.91 W/mm," *International Journal of Numerical Modelling: Electronic Networks, Devices and Fields*, vol. 34, no. 1, p. e2794, 2021.

H. Q. T. Bui, D. T. Tuyet, R. T. Velpula, **B. Jain**, H. P. T. Nguyen, and H. D. Nguyen, "Enhancing efficiency of AlGaN ultraviolet-B light-emitting diodes with graded p-AlGaN hole injection layer," *Physica Status Solidi A*, 2021.

B. Jain, R. T. Velpula, M. Tumuna, H. Q. T. Bui, J. Jude, T. T. Pham, A. V. Hoang, R. Wang, and H. P. T. Nguyen, "Enhancing the light extraction efficiency of AlInN nanowire ultraviolet light-emitting diodes with photonic crystal structures," *Optics Express*, vol. 28, no. 15, pp. 22908 - 22918, 2020.

B. Jain*, R. T. Velpula*, S. Velpula, H.-D. Nguyen, and H. P. T. Nguyen, "Enhanced hole transport in AlGaN deep ultraviolet light-emitting diodes using a double-sided step graded superlattice electron blocking layer," *Journal of the Optical Society of America B*, vol. 37, no. 9, pp. 2564 - 2569, 2020. (* Equal Contribution)

B. Jain, R. T. Velpula, H. Q. T. Bui, H.-D. Nguyen, T. R. Lenka, T. K. Nguyen, and H. P. T. Nguyen, "High performance electron blocking layer free InGaN/GaN nanowire white light-emitting diodes," *Optics Express*, vol. 28, no. 1, pp. 665-675, 2020.

R. T. Velpula*, **B. Jain***, H. Q. T. Bui, F. M. Shakiba, J. Jude, M. Tumuna, H.-D. Nguyen, T. R. Lenka, and H. P. T. Nguyen, "Improving carrier transport in AlGaN deep-ultraviolet light-emitting diodes using a strip-in-a-barrier structure," *Applied Optics*, vol. 59, no. 17, pp. 5276-5281, 2020. (* Equal Contribution)

R. T. Velpula, **B. Jain**, S. Velpula, H.-D. Nguyen, and H. P. T. Nguyen. "High-performance electron-blocking-layer-free deep ultraviolet light-emitting diodes implementing a strip-in-a-barrier structure," *Optics Letters*, vol. 45, no. 18, pp. 5125-5128, 2020.

R. T. Velpula, **B. Jain**, M. R. Philip, H. D. Nguyen, R. Wang and H. P. T. Nguyen, "Epitaxial growth and characterization of AlInN based core-shell nanowire light-emitting diodes operating in the ultraviolet spectrum," *Scientific Reports*, vol. 10, no. 1, p. 2547, 2020.

R. T. Velpula, **B. Jain**, T. H. Q. Bui, T. T. Pham, V. T. Le, H.-D. Nguyen, T. R. Lenka, H. P. T. Nguyen, "Numerical investigation on the device performance of electron blocking layer free AlInN nanowire deep ultraviolet light-emit-ting diodes," *Optical Materials Express*, vol. 10, no. 2, pp. 472-483, 2020 (Standout as one among 15 notable Fluorescent and Luminescent Materials papers from Optical Materials Express in 2020).

R. T. Velpula, **B. Jain**, T. H. Q. Bui, H. P. T. Nguyen, "Full-color III-nitride nanowire light-emitting diodes," *Journal of Advanced Engineering and Computation*, vol. 3, no. 4, pp. 551-588, 2020.

H. Q. T. Bui, R. T. Velpula, **B. Jain**, and H. P. T. Nguyen, "III-nitride based narrow band far-UVC LEDs for airborne and surface disinfection," *ECS Transactions*, vol. 98, no. 6, p. 83, 2020.

H. Q. T. Bui, R. T. Velpula, **B. Jain**, M. R. Philip, H. D. Tong, T. R. Lenka, and H. P. T. Nguyen, "High performance nanowire ultraviolet light-emitting diodes with potassium hydroxide and ammonium sulfide surface passivation," *Applied Optics*, vol. 59, no. 24, pp. 7352-7356, 2020 (Editor's Pick).

R. Singh, T. R. Lenka, R. T. Velpula, **B. Jain**, T. H. Q. Bui, and H. P. T. Nguyen, "Investigation of current collapse and recovery time due to deep level defect traps in β − Ga2O3 HEMT," *Journal of Semiconductors*, vol. 41, no. 10, p. 102802, 2020.

R. Singh, D. K. Panda, T. R. Lenka, R. T. Velpula, **B. Jain**, T. H. Q. Bui, and H. P. T. Nguyen, "The dawn of Ga2O3 HEMTs for high power electronics - a review," *Materials Science in Semiconductor Processing*, vol. 119, p. 105216, 2020.

D. K. Panda, R. Singh, T. R. Lenka, R. T. Velpula, **B. Jain**, T. H. Q. Bui, T. T. Pham, S. M. Sadaf, and H. P. T. Nguyen, "Single and double gate based GaN MOS-HEMTs for design of low noise amplifier: a comparative study," *IET Circuits, Devices & Systems*, vol. 14, no. 7, pp. 1018-1025, 2020.

B. Jain, C.-S. Huang, D. Misra, K. Tapily, R. D. Clark, S. Consiglio, C. S. Wajda and G. J. Leusink, "Multilevel resistive switching in Hf based RRAM," *ECS Transactions*, vol. 89, no. 3, pp. 39-44, 2019.

H. Q. T. Bui, R. T. Velpula, **B. Jain**, O. H. Aref, H.-D. Nguyen, T. R. Lenka, and H. P. T. Nguyen, "Full-color InGaN/AlGaN nanowire micro light-emitting diodes Grown by molecular beam epitaxy: a promising candidate for next generation micro displays," *Micromachines*, vol. 10, no. 8, p. 492, 2019.

B. Jain, K. V. Kumar, B. S. Bhushan, M. Pattanaik and A. Srivastava, "Tetracene based single electron transistor as chlorine sensor," *Journal of Computational Electronics (JCEL)*, vol. 17, no. 4, pp. 1515-1520, 2018.

D. Misra, S. Sultana, **B. Jain**, N. Bhat, K. Tapily, R. D. Clark, S. Consiglio, C. S. Wajda and G. J. Leusink, "Bilayer dielectrics for RRAM devices," *ECS Transactions*, vol. 86, no. 2, pp. 77-83, 2018.

Conferences:

B. Jain, R. T. Velpula, and H. P. T. Nguyen, "Phosphor free III-nitride red micro-light emitting diodes for display applications," *Presented in CLEO: Applications and Technology, Optical Society of America*, 2021.

B. Jain, R. T. Velpula, M. Patel, and H. P. T. Nguyen, "High-performance electron-blocking layer-free ultraviolet light-emitting diodes," *Physics and Simulation of Optoelectronic Devices XXIX, vol. 11680. International Society for Optics and Photonics*, 2021.

R. T. Velpula, **B. Jain**, T. R. Lenka, and H. P. T. Nguyen, "InGaN/GaN nanowire white color light-emitting diodes without electron blocking layer," *2021 Springer International Conference on Micro/Nanoelectronics Devices, Circuits, and Systems (MNDCS-2021)*. (Invited Talk)

M. Patel, **B. Jain**, R. T. Velpula, and H. P. T. Nguyen. "Effect of HfO_2 passivation layer on light extraction efficiency of AlInN nanowire ultraviolet light-emitting diodes," *In 239th ECS Meeting with the 18th International Meeting on Chemical Sensors (IMCS)(May 30-June3, 2021). ECS*, 2021.

H. P. T. Nguyen, R. T. Velpula, and **B. Jain**, "High efficiency AlInN nanowire light-emitting diodes grown by molecular beam epitaxy," *Presented in 2021 IEEE Latin America Electron Devices Conference (LAEDC)*.

B. Jain, R. T. Velpula, H. Q. T. Bui, M. Tumuna, J. Jude, and H. P. T. Nguyen, "Electron blocking layer free AlGaN deep-ultraviolet light emitting diodes," *CLEO: Applications and Technology*, pp. AF1I-3. Optical Society of America, 2020.

B. Jain, R. T. Velpula, H. Q. T. Bui, M. Patel, and H. P. T. Nguyen, "Electron blocking layer free full-color InGaN/GaN white light-emitting diodes," *PRiME 2020 (ECS, ECSJ, & KECS Joint Meeting)*.

R. T. Velpula, **B. Jain**, H. Q. T. Bui, and H. P. T. Nguyen, "Ultraviolet light-emitting diodes using aluminium indium nitride nanowire structures," *PRiME 2020 (ECS, ECSJ, & KECS Joint Meeting)*.

R. T. Velpula, **B. Jain**, H. Q. T. Bui, and H. P. T. Nguyen, "High-efficiency ultraviolet emission from AlInN/GaN nanowires grown by molecular beam epitaxy," *CLEO: Science and Innovations*, pp. STu3P-4. Optical Society of America, 2020.

H. Q. T. Bui, R. T. Velpula, **B. Jain**, and H. P. T. Nguyen, "Full-color microLEDs for display technologies," *CLEO: Applications and Technology*, pp. ATh3I-4. Optical Society of America, 2020.

B. Jain, K. K. Jha, and M. Pattanaik "Comparative analysis of MOSFET and STBFET based amplifier for analog application," *2018 4th International Conference on Devices, Circuits and Systems (ICDCS), IEEE*, pp. 198-202, 2018.

I would like to dedicate my dissertation to my immediate family comprising of my husband (Ravi Teja Velpula), father (Subash Jain), mother (Nirmala Devi Jain) and parents in law (Rajshekhar Velpula and Usha Rani Velpula) in token of their earnest prayers, love and support, they have showered on me.

ACKNOWLEDGMENT

Give thanks to the LORD, for he is good; his love endures forever.
(Psalm 136:1)

First and foremost, I would like to express my deepest gratitude to my dissertation advisor, Dr. Hieu Pham Trung Nguyen, who is a great mentor and supporter. He always encouraged and provided the freedom to explore new ideas. He really understands and supports his students unconditionally. It was a pleasure working, learning, and researching in his lab. Dr. Hieu provided many opportunities such as research collaborations from electronic to photonic devices, working with interns to graduate students, working in the cleanroom environment for the device fabrication, supporting internship opportunities. I could reach the final phase of my Ph.D. due to his invaluable guidance and knowledgeable discussions.

Next, I would like to thank my dissertation committee members: Dr. Marek Sosnowski, Dr. Dong-Kyun Ko, Dr. Xuan Liu, and Dr. Eon Soo Lee for providing me valuable suggestions and advice on my Ph.D. research work. I am grateful to Dr. Durgamadhab Misra, who was my academic advisor and supported my research during the initial days of my Ph.D. program.

I also acknowledge the Teaching Assistantship funding from the Department of Electrical and Computer Engineering. I am grateful to the National Science Foundation (ECCS-1944312) for supporting my research and providing Research Assistantship. I would also like to thank Cornell Nanoscale Science and Technology Facility, a member of the National Nanotechnology Coordinated Infrastructure (NNCI) for providing the fabrication facility for the research.

I want to thank my colleagues: Ravi Teja Velpula and Ha Quoc Thang Bui; master students Moulik Patel; and undergraduate students Omar Hamed Aref, Moses Tumuna, Jeffrey Jude, and Andressa Marangon at the Nano-Optoelectronic Materials and Devices Lab for their valuable discussions and contribution of some of the work in this dissertation. I would also like to acknowledge Dr. Trupti Ranjan Lenka and his group for the collaborative work. I would further like to thank Dr. Peter Paliwoda and Dr. Nasir Uddin Bhuyian for the gracious support and technical discussion. I also take this opportunity to thank staff administrators in my department, especially Joan Mahon, Ellen Stark, and Teri Bass. I am grateful to my mentors and managers at Intel Corporation: Dr. Roman Sancho, Dr. Vinod Ambrose, Biju Paremeshwaran, Dr. Zakariae Chbili, Dr. Zhenghao Gan, for their support and guidance on my intern projects.

I would like to thank Ms. Clarisa Gonzalez-Lenahan and Dr. Sotirios Ziavras from the Office of Graduate Studies, for the dissertation document review process and for helping me with the degree completion paperwork.

Importantly, I would like to express my deepest love to my parents, Subash Jain and Nirmala Devi Jain, brother Gyanendra Jain, his wife Shibani Jain, uncle Ganesh Agrawal and other family members. They are always on my side, encouraging and motivating me to achieve my dream. I would like to especially express my gratitude to my father, Subash Jain for providing his boundless love and support at every stage of my life and always encourage me to pursue my dream. I also wish to thank my parents-in-law, Rajashekhar Velpula and Usha Rani Velpula for their support and encouragement. Last but not the least, I would like to express my love to my husband, Ravi Teja Velpula who was and is always by myside during the most difficult time of this journey, shared my burden,

and walked through with me, without whose support I would not have achieved what I have today.

CONTRIBUTIONS OF AUTHORS

This dissertation contains a collection of research articles published by the candidate and her dissertation advisor Prof. Hieu P T Nguyen with the collaboration of other co-authors. In Chapter 2, phosphor-free InGaN/GaN nanowire white color LED device optimization using theoretical model, simulations using Crosslight APSYS software, structural (scanning electron microscopy), and electrical (Electroluminescence intensity, I-V, power) characterizations were performed primarily by the candidate. The candidate contributed to the optical (Photoluminescence intensity) characterizations with the assistance of Ravi Teja Velpula and Dr. Ha Quoc Thang Bui. The molecular beam epitaxial growth and device fabrication of these LEDs were performed by Prof. Hieu P T Nguyen. From Chapter 3 to Chapter 5, band-engineering of all AlGaN UV LED device structures, theoretical modeling, simulations using Crosslight APSYS, data curation and analysis were primarily done by the candidate. In Chapter 6, Dr. Moab Rajan Philip, Dr. Renjie Wang, and Prof. Hieu P T Nguyen contributed to the molecular beam epitaxial growth and device fabrication of AlInN nanowire UV LED. The structural (scanning electron microscopy), optical (Photoluminescence intensity) and electrical (Electroluminescence intensity, I-V) characterizations were mainly performed by the candidate with the help of Ravi Teja Velpula. Further, FDTD simulations were primarily performed by the candidate. Photonic band diagrams were calculated using the MEEP software by the candidate with assistance from Moses Tumuna. Lastly, AlN RRAM device design, fabrication and electrical characterization were primarily performed by the candidate, presented in Chapter 7. Also, Prof. Hieu P T Nguyen was listed as the corresponding author on the research articles reflecting his supervision role throughout the candidate's work.

STATEMENT OF ORIGINALITY

This dissertation is the collection of five journal papers which are published in Optics Express, Journal of the Optical Society of America B, Applied Optics, and Micromachines. As III-nitride-based LEDs are a key part of the current solid-state lighting technology, this dissertation has made several unique contributions to the field of photonics and nanotechnology by addressing the critical issues of the current LEDs in visible and UV regions. One of the primary issues in the current LEDs is the electron leakage from the active region which affects the hole injection process adversely and reduces the efficiency of the LEDs. To address this issue, in this dissertation we have band-engineered various epilayers and demonstrated significant improvement in the device performance by reducing the electron overflow. Further, a promising approach for fabricating high-efficiency UV nanowire LEDs using AlInN semiconductors is demonstrated.

To address the issue of electron overflow in phosphor-free nanowire white LEDs, we have introduced coupled quantum well in the LED structure; consequently, the efficiency of the InGaN/GaN nanowire LEDs is increased to 58.5% without any efficiency droop up to 1000A/cm^2 and with a remarkably stable white-light emission. In addition, to address the issue of electron overflow in UV LEDs, we have demonstrated various designs with an impressive improvement in the device performance. For instance, the enhanced carrier transportation in the reported structure could reduce the electron leakage by ~12 times as compared to conventional EBL-based LEDs operating at ~254 nm wavelength. These demonstrated LED designs provide the solution for the electron leakage problem and open a new path for the realization of high-efficiency and high-power UV light emitters for practical applications.

In addition, the high crystalline quality of AlInN nanowire LED structures with stable and strong EL emission at ~299 nm peak wavelength is demonstrated. Next, the light extraction efficiency of the reported AlInN nanowire LEDs is improved to ~63% using photonics crystal structures out of which almost ~60% of the light could be extracted from the top surface of the LEDs. Moreover, the switching capability of AlN memory devices is demonstrated for the first time for low-power applications in the range of 20 nWatts.

In conclusion, the work demonstrated in this Ph.D. dissertation has a significant contribution to the field of optoelectronic and electronic devices by developing high-performance light emitters and low-power memory devices.

TABLE OF CONTENTS

TABLE OF CONTENTS
(Continued)

TABLE OF CONTENTS
(Continued)

LIST OF TABLES

LIST OF FIGURES

List of Figures
(Continued)

LIST OF FIGURES
(Continued)

LIST OF FIGURES
(Continued)

LIST OF SYMBOLS

LED	Light-Emitting Diodes
SSL	Solid-state Lighting
CFL	Compact Fluorescent Lighting
MBE	Molecular Beam Epitaxy
MOCVD	Metal Organic Chemical Vapor Deposition
LEEBI	Low-Energy Electron Beam Irradiation
QW	Quantum Well
SQW	Single Quantum Well
EQE	External Quantum Efficiency
UV	Ultraviolet
HEMT	High Electron Mobility Transistors
MQWs	Multi-Quantum Wells
QCSE	Quantum Confined Stark Effect
EBL	Electron-Blocking Layer
QD	Quantum Dots
PAMBE	Plasma-Assisted Molecular Beam Epitaxy
LEE	Light Extraction Efficiency
TE	Transverse Electric
TM	Transverse Magnetic
FDTD	Finite Difference Time Domain
QB	Quantum Barrier
LO	Longitudinal Optical
APSYS	Advanced Physical Models of Semiconductor Devices
IQE	Internal Quantum Efficiency
MFP	Mean Free Path

STEM	Scanning Transmission Electron Microscope
SEM	Scanning Electron Microscopy
ITO	Indium Tin Oxide
SL	Superlattice
DSGS	Double-sided Step Graded Superlattice
DSG	Double-sided Step Graded
LQB	Last Quantum Barrier
SRH	Shockley-Read-Hall
EL	Electroluminescence
PL	Photoluminescence
VBBH	Valence Band Barrier Height
CBBH	Conduction Band Barrier Height
RRAM	Resistive Random-Access Memory
BE	Bottom Electrode
TE	Top Electrode
HRS	High Resistance State
LRS	Low Resistance State

CHAPTER 1

INTRODUCTION

1.1 Solid-State Lighting

Over the last few years, semiconductor light-emitting diodes (LEDs) have become the major component of the current solid-state lighting (SSL) technology. With the continuous improvement in performance and cost reduction in the last decades, SSL has emerged to be a realistic replacement for incandescent and fluorescent lamps for our homes and offices. LED light bulbs or lamps can, in principle, be 20 times more efficient than incandescent lighting and five times more efficient than florescent lighting [1-3]. In incandescent lighting, electric current flows through a tungsten filament to heat it up sufficiently enough that it glows. In this process, a substantial amount of input energy or power is converted to heat and infrared emission rather than the desired visible light emission. Associated with this process is an energy loss of ~90% or more (only about 10% of the energy is used to make visible light).

An alternative to this inefficient incandescent lighting, compact fluorescent lighting (CFL), has been on the market for quite some time. But CFL usage has also been limited due to toxic mercury-related complexity in their design prototype; it also suffers from parasitic energy losses [4]. Furthermore, both incandescent and CFL lighting contribute to increased emissions of pollutants such as CO_2 and SO_2 and nuclear waste [4]. These are identified as critical roadblocks for efficient SSL technology. Therefore, there has been a

growing demand for low-cost, highly efficient, environment-friendly and phosphor-free (to avoid down conversion loss) visible light sources.

These long-standing critical problems can potentially be solved by adopting energy-efficient LEDs. In solid-state LEDs, electrons (from *n*-type semiconductors) recombine radiatively with holes (*p*-type semiconductors) to emit photons or visible light (blue, green, red or white), directly converting electricity into light. Compared with any other existing lighting technology, SSL possesses two highly desirable features: (1) it is highly energy-efficient with tremendous potential to generate visible light with reduced heat generation and much less energy consumption and reduction in carbon emissions;
(2) it is an extremely versatile light source with many controllable properties including the emission spectrum, direction, color temperature, modulation and polarization [5].

Nowadays, SSL based on LEDs is already commercialized and widely used, for example, as traffic signals, large outdoor displays, interior and exterior lighting in aircrafts, cars and buses, as bulbs in flashlights and as backlighting for cell phones, liquid-crystal displays, radio frequency (RF) electronics, power electronics and many more. The beneficial impact of LEDs on the economy, environment and our quality of life is so evident and well recognized that the 2014 Nobel Prize in Physics was awarded to the inventors of efficient blue LEDs: Isamu Akasaki, Hiroshi Amano and Shuji Nakamura. Current energy-efficient, environment-friendly SSL technology largely depends on the development of emerging LED technology.

1.1.1 LED History

The first, red light-emitting device was developed and demonstrated by Nick Holonyak and coworkers at General Electric's Solid-State Device Research Laboratory in Syracuse,

New York, the U.S. in 1962 [6]. This demonstration was based on GaAsP on a GaAs substrate. During the time or even earlier, green emission was demonstrated based on GaP [7]. Since then, the efficiency of GaP and GaAsP advanced significantly in the 1960s and 1970s. In the early 1990s, relatively high-efficiency GaAlAsP and AlInGaP LEDs were demonstrated with yellow and red emissions. Interestingly, early GaP or GaAsP based LEDs showed luminous efficacy of about 0.02 lm/W whereas later GaAlAs(P) based LEDs showed luminous efficacy of about 10 lm/W. Finally, current AlInGaP LEDs show luminous efficacy of about >150 lm/W. The development of the nitride material system (GaN, InN, AlN and their alloys) in the last two decades has enabled efficient light emission to expand into the blue and green spectral region.

Efficient and cost-effective white light emission has been severely limited by several factors. First, phosphor-assisted down conversion needs relatively shorter wavelength blue LEDs, but existing efficient (at yellow and red spectral regions) GaAlAsP and AlInAsP LEDs and/or semi-efficient GaAs and InP based materials cannot emit at such a short wavelength range (blue spectral region). The material that enabled the production of white light (blue is the high-energy end of the visible spectrum and therefore enables the production of white light using blue light plus phosphors). However, the development of GaN-based blue LEDs had been limited due to GaN crystal growth/deposition and inefficient *p*-type doping.

In 1969, Maruska and Tietjen at Radio Corporation of America Laboratories (Princeton, New Jersey, USA) demonstrated the successful growth of single-crystal GaN film on a sapphire substrate by chemical vapor deposition (CVD) technique [8]. Later, Yoshida et al. developed GaN films using an AlN buffer layer on sapphire by reactive

molecular beam epitaxy (MBE) in 1983 [9]. A few years later in 1986, Amano et al. achieved crack-free GaN films with good surface morphology and crystallinity by growing a thin AlN buffer layer on sapphire at low-temperature by using metal-organic chemical vapor deposition (MOCVD) [10]. After successful demonstration of high-quality GaN films by MBE and MOCVD, in 1989, Amano et al. demonstrated that a low-energy electron beam irradiation (LEEBI) treatment in a scanning electron microscope could cause a previously highly resistive Mg-doped GaN layer to show distinct *p*-type conductivity, enabling the first GaN *p*-*n* junction LED [11]. Later, Nakamura et al. achieved better *p*-type GaN films with improved hole concentration and mobility using post thermal annealing under an NH_3 ambient gas [12].

After the successful demonstration of GaN growth and efficient *p*-type doping, Nakamura et al. developed GaN *p*-*n* junction blue light LED in 1991 [13]. Although *p*-*n* junction GaN LEDs showed 10 times higher output power as compared to the conventional SiC blue LEDs, it was limited to ~ 42 μW and external quantum efficiency ~0.18% at 430 nm emission wavelength. Subsequently, Nakamura et al. demonstrated *p*-GaN/*n*-InGaN/*n*-GaN double-heterostructure blue LEDs in 1993 with improved performance of output power of 125 μW and external quantum efficiency of 0.22% [14]. In 1994, Nakamura et al. demonstrated commercially available blue LEDs with a *p*-AlGaN electron blocking layer (EBL) where their group demonstrated the output power of 1500 μW and external quantum efficiency (EQE) of 2.7% at 450 nm emission wavelength [15]. In 1995, Nakamura et al. demonstrated bright blue, green, and yellow emission LEDs with InGaN quantum-well (QW) structure [16]. Later, they showed super bright green single quantum

well (SQW) LEDs with an output power of 3 mW and EQE of 6.3% at the peak wavelength of 520 nm [17].

The invention of efficient blue LEDs has enabled a white light source for illumination. White light was demonstrated for the first time by combining a blue GaN LED with a yellow-emitting phosphor in 1997 [18]. After the successful demonstration of LEDs, many corporates' industries have developed and continued to use GaN-on-sapphire, GaN-on-SiC and GaN-on-GaN technologies.

1.1.2 LED Basics

The simplest LED structure is a *p*-*n* junction, consisting of *p*-type doped semiconductor material connected to a *n*-type doped semiconductor material to form a diode with a thin active region at the junction. The principle for light emission in a *p*-*n* junction is illustrated in Figure 1.1. The *n*-type region is rich in negatively charged electrons, while the *p*-type region is rich in positively charged holes. When a voltage is applied to the junction (called forward bias), the electrons are ejected from the *n*-type region and holes are ejected from the *p*-type region across the junction as shown in Figure 1.1(b). When the electrons and holes subsequently meet and recombine radiatively, the energy released is given out as light with an emission wavelength close to the bandgap of the material incorporated in the active region. For high efficiency, a heterojunction (consisting of two semiconductor materials with different bandgap) is usually preferred to a homojunction (consisting of single semiconductor material) due to better carrier confinement, as shown in Figure 1.1(c), i.e., the electrons and holes are spatially confined together in the active region with lower bandgap energy, which increases the chance of radiative recombination to produce light.

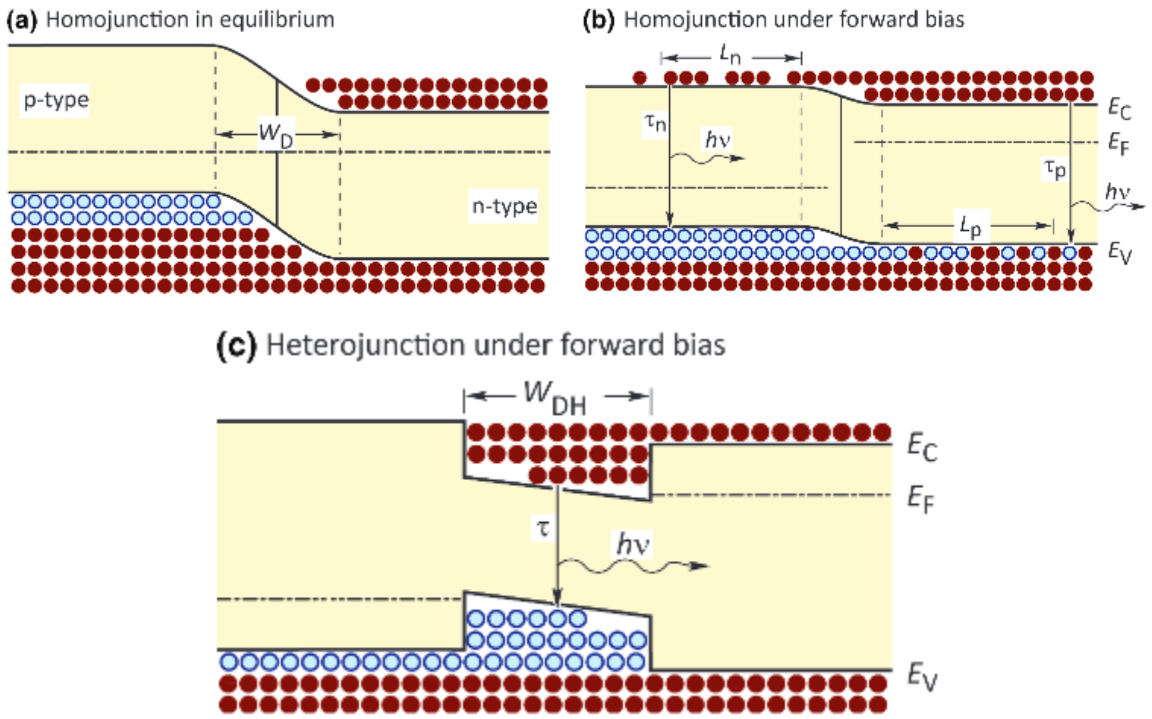

Figure 1.1 A *p-n* homojunction under (a) equilibrium, (b) forward bias, (c) A *p-n* heterojunction under forward bias. E_C, E_F and E_V are the conduction band, Fermi and valence band energy. The filled circle and open circle represent electrons and holes, respectively.
Source: [19]

For most optoelectronics devices such as LEDs, laser diodes, and photodetectors, a direct bandgap is essential for efficient device performance. This is because the optical emission process in a indirect bandgap semiconductor requires phonons for momentum conservation. The involvement of the phonon makes this radiative process much less likely to occur in a given timespan, which allows non-radiative processes to effectively compete, generating heat rather than light. Therefore, semiconductors with an indirect bandgap are not suitable for efficient LEDs [5].

1.1.2.1 White LEDs. Traditional LEDs emit monochromatic light. However, white LEDs emit polychromatic light. There are several viable approaches to producing white LEDs. The first approach is a multi-LED-chip approach in which the light emitted from three LED chips emitting the three primary colors (red, green, and blue (RGB)) are mixed to generate white light as shown in Figure 1.2(a). In this process, photon down-conversion loss can be potentially avoided [20]. However, this process requires a complicated balancing of RGB output over the temperature and over the optical lifetime that further requires sophisticated optical feedback driver electronics.

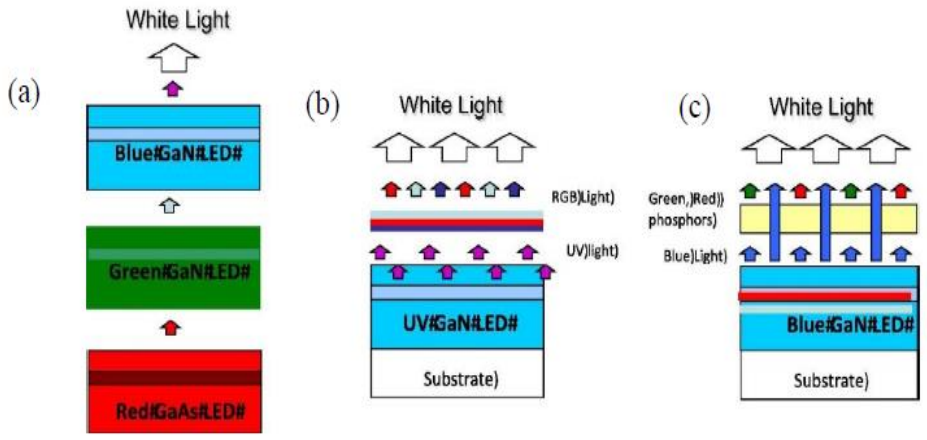

Figure 1.2 Different ways of generating white light from GaN LEDs: (a) combination of red, green and blue LEDs, (b) UV GaN LED plus three phosphors, and (c) blue GaN LED plus yellow phosphor.
Source: [21]

The second approach is based on using an ultraviolet (UV) or violet LED chip and a phosphor that absorbs the UV or violet light and converts it to a broadband white light as shown in Figure 1.2(b). This approach suffers from a low efficiency because the down-conversion of UV or violet light involves a relatively large wavelength shift [20]. The third approach is the combination of a blue-LED chip and phosphor converter with the phosphor

emitting green and red light as shown in Figure 1.2(c). The blue light from the LED chip is partially absorbed by the phosphor while the other part of the blue light is transmitted through the phosphor. As a result, the blue, green and red lights together form white light. However, the phosphor-converted white light sources have several disadvantages including a short lifetime and lower color rendering index value and that makes such devices undesirable for indoor use.

1.1.2.2 Ultraviolet LEDs. These days, as the demand for various applications of UV light such as sterilization, disinfection, water and air purification, and biological sensors increases, the previously used UV sources such as mercury and xenon lamps are found to be unsatisfactory as they are bulky, expensive and have a short life time. It has become increasingly important to investigate a new advanced technology as a source of UV emission for these applications. The UV LEDs are a tunable, long life, and environmentally friendly alternative to traditional UV sources [5].

1.2 III-Nitride Based LEDs

Conventional cubic III-V compound semiconductors, such as arsenides and phosphides, show a direct-to-indirect bandgap transition towards higher energies. Therefore, high-efficiency devices can be achieved in the infrared and red-to-yellow visible spectral regions, but the efficiency decreases drastically for conventional III-V semiconductors in the UV region as the bandgap becomes indirect.

In contrast, the nitrides have the hexagonal wurtzite structure, and the bandgap remains direct across the entire composition range from AlN to InN. Unique to this material system is that its energy bandgap can be tuned from the deep UV (~ 6.2 eV for AlN) to the near-infrared (~ 0.65 eV for InN) [22]. This makes the group-III nitrides system

particularly suitable for LEDs. Although tremendous progress has been made in the III-nitride materials system, the applications of III-nitride planar devices have been limited predominantly because of different challenges, which limit the efficiency of the planar devices.

1.2.1 Challenges in III-nitride Based Thin Film LEDs

1.2.1.1 Polarization fields. III-nitride materials system including InN, GaN, AlN and their ternary alloys crystallize in wurtzite and zinc-blende crystal structure. However, compared to zinc-blende, thermodynamically stable wurtzite crystal structure with alternating planes of metal (Ga, In, Al) and N atoms are preferred for device applications. Due to the large electronegativity and small size of N atoms compared to metal atoms, the bonds formed between Ga/Al/In and N show polar (large ionicity) characteristics along with the [0001] direction.

As shown in Figure 1.3, each GaN unit cell is defined by the edge length of the basal hexagon, the height c of the hexagonal prism and an internal parameter u as the anion-cation bond length along the (0001) axis in units of c. Each GaN unit cell contains a charge dipole formed due to the spatial separation of negative charge (electron cloud) and positive charge (the nuclei). Due to these minute displacements of the electron cloud and positively charged nuclei, a surface polarization charge as high as $P_{sp}/e \sim 1.8\times10^{13}/cm^2$ was estimated for GaN, whereas for AlN, a charge density of $\sim 5\times10^{13}/cm^2$ was estimated. Given the sheet charge density in semiconductors is $\sim10^{15}/cm^2$, roughly one out of 100 atoms can be assumed to be contributing to the polarization charge. An electric field of ~1-10 MV/cm is associated with these polarization sheet charges [23]. These polar dipoles cancel each other in the bulk material yet form negative/positive sheet charges at the surfaces.

Wurtzite hexagonal close-packed crystal structures exhibit spontaneous polarization, due to the non-centrosymmetric nature of the ions. Conversely, spontaneous polarization is negligible in symmetric zinc-blende crystal structures. The Ga atom terminated surface (Ga-polar) develops a negative sheet charge, and alternatively, the N atoms terminated surface (N-polar) shows a positive sheet charge at the interface.

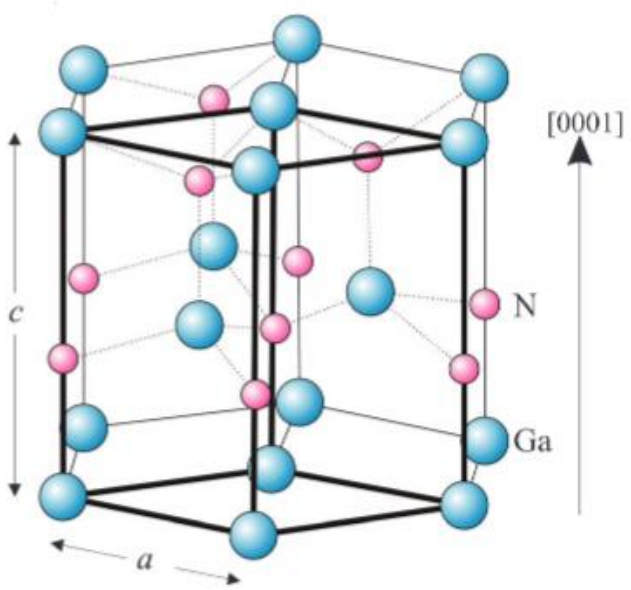

Figure 1.3 Crystal structure of GaN.
Source: [24]

Table 1.1 Effect of Lattice Non-Ideality on the Magnitude of Spontaneous Polarization in III-Nitrides

Material	AlN	GaN	InN
c_0/a_0	1.6010	1.6259	1.6116
P_{sp} (C/m^2)	-0.081	-0.029	-0.032

Source: [23]

Table 1.2 Piezoelectric Constants of Wurtzite AlN and GaN Used in the Calculations

Material	e_{31} (C/m^2)	e_{33} (C/m^2)	C_{13} (Gpa)	C_{33} (Gpa)
GaN	-0.49	0.73	103	405
AlN	-0.6	1.46	108	373

Source: [23]

In addition to the spontaneous polarization, there is a net charge (positive or negative) due to the piezoelectric polarization at the strained AlGaN/GaN or InGaN/GaN heterointerfaces. Such strain-induced piezoelectric polarization can be calculated with the piezoelectric constants in Table 1.2 and the following Equation:

$$P_{pz} = e_{33}\varepsilon_3 + e_{31}(\varepsilon_1 + \varepsilon_2) \tag{1.1}$$

Where e_{31} and e_{33} are the two components of piezoelectric tensor (in C/m^2), $\varepsilon_3 = (c-c_0)/c_0$ represents the strain along the c-axis or [0001] direction, and $\varepsilon_1 = \varepsilon_2 = (a-a_0)/a_0$ is the in-plane isotropic strain. Here, c_0 and a_0 are the final out of the plane and in-plane lattice parameters of the strained crystal. However, in the wurtzite crystal structure, out of the plane and in-plane lattice parameters are related and can be expressed by the following Equation:

$$\frac{c_0 - c}{c} = -\frac{2c_{13}}{c_{33}\dfrac{a_0 - a}{a}} \tag{1.2}$$

Where C_{13} and C_{33} are the in-plane and out-of-plane elastic constants, respectively (Table 1.2). By combining Equations. (1.1) and (1.2) the net strain-induced piezoelectric polarization along the [0001] can be expressed by the following formula:

$$P_{pz} = \frac{2(a_0 - a)}{a}\left(e_{31} - e_{33}\frac{c_{13}}{c_{33}}\right) \tag{1.3}$$

As shown in Table 1.2, in wurtzite III-nitrides, e_{31} is always negative, while e_{33}, c_{13} and c_{33} are always positive, therefore (e_{31}-$e_{33}\frac{c_{13}}{c_{33}}$) will always be a negative number. Hence, Ppz in III-N is always negative for layers under tensile stress ($a>a_0$), and positive for layers under compressive stress ($a < a_0$) as shown in Table 1.1. However, spontaneous polarization, Ps in III-N is always negative. For layers under tensile stress, Ps and Pz are parallel to each other and for layers under compressive stress, the two polarizations are anti-parallel. This polarization (spontaneous + piezoelectric) charge further leads to a high polarization field that is a prerequisite for developing nitride-based high electron mobility transistors (HEMTs) and recent polarization engineered tunnel junctions. The charges related to piezoelectric polarization arise at the interface of lattice-mismatched materials.

Piezoelectric polarization associated with large strain at the heterointerfaces leads to anion to cation displacement. The piezoelectric polarization field is stronger than the spontaneous polarization field in visible InGaN-based LEDs and lasers, and such a strong field plays an important role in device performance. These piezoelectric charges and resulting large piezoelectric fields (of about 2 MV/cm) have been exploited in many devices using III-nitrides. In the InGaN/GaN-based LEDs, this piezoelectric polarization becomes more problematic since it largely facilitates electron escape from the active region to the p-side region. As shown in Figure 1.4, polarization-induced sheet charge-related band bending in the InGaN/GaN active region favors electron leakage or overflow from the active region reducing radiative recombination.

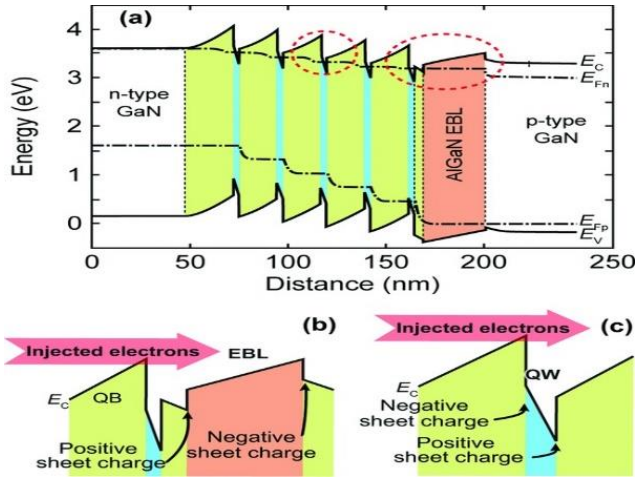

Figure 1.4 (a) Effect of spontaneous and piezoelectric polarization on the band diagram of InGaN/GaN multi quantum wells (MQW), (b) and (c) origin of negative and positive sheet charges at the EBL and at the last GaN barrier layer.
Source: [25]

This electron leakage further leads to the efficiency droop problem [25]. Furthermore, the presence of the polarization field in InGaN/GaN multi-quantum wells (MQW) causes the quantum confined stark effect (QCSE) that reduces the overlap potential (spatial separation) of electron and hole (band bending in the opposite direction) wave function in the LED active region [26, 27]. This QCSE effect reduces the radiative recombination probability and leads to increased carrier loss and degrades the overall performance of the LED [27].

1.2.1.2 Defects and dislocations. The large lattice mismatch between the nitride-based materials and the substrates such as sapphire, SiC and Si generally leads to the generation of very large crystalline defect densities in LED heterostructures. These defects include unwanted foreign atoms, native defects [28, 29], and any complexes of defects, foreign atoms, or dislocations [19]. All such defects have energy level structures that are different

from substitutional semiconductor atoms. It is quite common for such defects to form one or several energy levels within the forbidden gap of the semiconductor and these are a good source of non-radiative recombination. The resulting non-radiative recombination at these defect energy levels is called as the Shockley-Read-Hall (SRH) non-radiative recombination and these can significantly degrade the device efficiency. Frequently, defects group into clusters of defects or extended defects. Such extended defects are, for example, threading dislocations and misfit dislocations generated in the layers grown epitaxially on the substrate due to lattice mismatch. The dislocation density for GaN based heterostructures is typically reported in range of ~108 to 1010 cm-2 [30-33]. If we assume unity electrical injection efficiency, the internal quantum efficiency (ηi) is typically modeled by the ABC model:

$$\eta_i = \frac{BN^2}{AN + BN^2 + CN^3 + f(N)} \tag{1.4}$$

In Equation (1.4), N represents the carrier density and A, B, and C are the SRH nonradiative recombination, radiative recombination, and Auger recombination coefficients, respectively. f(N) represents the carrier leakage outside of the active region [34, 35]. Based on the above ABC model, parameter A is related to the crystal defects which generally influence the maximum achievable efficiency [1]. Therefore, it is crucial to reduce the lattice mismatch of LEDs and minimize the performance degradation in the optical and electrical performance of these devices.

1.2.1.3 Auger recombination. Another important non-radiative recombination mechanism is Auger recombination. In this process, the energy becoming available through electron-hole recombination (approximately E_g), is dissipated by the excitation of a free-electron high into the conduction band, or by a hole deeply excited into the valence band [19]. The excited carrier can subsequently release its energy thermally and relax to the band edge. The Auger recombination rate is typically higher for narrow bandgap semiconductor materials as compared to the wide bandgap semiconductor materials. The expected Auger recombination coefficient in GaN (bandgap ~ 3.4 eV) is ~ 10^{-34} cm^6s^{-1} [36], whereas for InGaN alloys, its reported to be much higher (in the range of ~ 10^{-30} cm^6s^{-1}) [37-39]. In the ABC model as well, if we neglect other effects, evidently, efficiency droop can increase as the Auger coefficient C becomes larger.

1.2.1.4 Electron overflow. Electron overflow refers to the leakage or flow of electrons from the active region without being captured or radiatively recombined in the active region. This is also one of the major problems causing efficiency droop in III-nitride LEDs.

One of the primary reasons for electron overflow is the reduction of the energy barrier due to the built-in polarization field [40]. The polarization field causes the band energy to tilt, which results in the separation of electrons and holes. Because of this, carrier recombination is also reduced. The overflowed electrons can recombine with holes in the *p*-GaN region before the holes can reach the active region, resulting in the degradation of radiative recombination in the active region [1]. In this context a large bandgap material. i.e., AlGaN EBL is often incorporated between the last quantum well and the *p*-GaN region to reduce the electron leakage [41, 42]. However, a high Al content-based EBL may form a high barrier, resulting in the further reduction of hole injection in the LED active region.

Also, at relatively high carrier injection, EBL usually cannot completely block the electron overflow in GaN LEDs and as a result, causes the efficiency droop in the devices. In dot-in-a-wire QDs structures, it was proposed that the optimum quantum efficiency is limited by electron leakage rather than Auger recombination. By incorporating a *p*-doped large bandgap AlGaN (low Al%) EBL, Nguyen et al. improved the efficiency droop significantly [41].

1.2.1.5 Poor hole injection and transportation efficiency. Hole injection and transportation in the active region is Hole injection and transportation in the active region is highly inefficient due to the heavy effective mass and low mobility [43]. Due to this, injected holes are located mostly close to the quantum wells or dots close to the *p*-side and hole concentration is significantly reduced toward the *n*-doped GaN side. Therefore, reasonable photon emission is delivered from the quantum wells or dots close to the *p*-side only. Conversely, electrons have lower effective mass, due to which electron distribution is expected to be more uniform across the quantum well [43]. The typical electron mobility in AlGaN based optoelectronic devices is ~ 200 cm^2/V-sec or more and a high concentration of electron carriers is readily achievable due to high ionization efficiency and low ionization energy. However, holes in GaN typically have ~ 20 times lower mobility than electrons i.e., 10 cm^2/V.sec, due to the large *p*-type dopant (Mg) ionization energy. This non-uniform flow causes electron overflow and Auger recombination and reduces radiative recombination. Some solutions have been suggested to overcome this problem such as the *p*-doped active region. The hole concentration uniformity has been improved by varying the barrier thickness [44, 45].

1.2.1.6 Inefficient *p*-type doping. When GaN film was first demonstrated using MBE and MOCVD methods by Yoshida et al. in 1983[9, 10], it was found to be unintentionally *n*-type doped due to the presence of oxygen vacancies and nitrogen vacancies. After that, many efforts have been put to develop *p*-type GaN using Mg doping via different methods. In 1989, Amano et al. first demonstrated Mg-doped *p*-type GaN by post-growth LEEBI treatment where he demonstrated the measured hole concentration and mobility to be ~ 2×10^{16} cm^{-3} and 8 cm^2/V.s., respectively [11].

In 1992, Nakamura et al. demonstrated *p*-doped GaN films using NH_3 free post thermal annealing in N_2 ambient and measured hole concentration and mobility to be 3×10^{17} cm^{-3} and 10 cm^2/V.s. Nakamura explained after this study that, in environments containing NH_3, atomic hydrogen (NH_3 dissociation) as interstitial defects impedes the activation of Mg acceptors by forming Mg-H complexes and in conventional MOCVD GaN growth, Mg dopant activation was hindered because of this [46]. In the post-growth treatment in N_2 ambient, Hydrogen atoms were dissociated and removed from complex Mg-H [12]. Still, *p*-type doping density is low (~10^{17} cm^{-3}) in conventional MOCVD growth techniques due to the high ionization energy of holes (~170 meV) [47]. Later Bhattacharya et al. have successfully demonstrated low-temperature growth of *p*-doped GaN in nitrogen-rich plasma-assisted molecular beam epitaxy (PAMBE) and achieved a doping density as high as ~ 2×10^{18} cm^{-3} [48]. In MBE growth, electrically active hole concentrations in GaN have been limited to a low range (~10^{18} cm^{-3}) with a doping efficiency of ~5%. Such a low doping efficiency is due to the high activation energy of Mg acceptor level, lower solubility, and compensation from defects present in the structure.

Current lighting technology still relies on the efficient activation of the *p*-type Mg dopants in GaN by forming shallow acceptor levels in GaN.

1.2.1.7 Highly resistive *p*-Al(Ga)N contact. To make perfect ohmic contact with a *p*-type semiconductor, ideally, the metal work function must be greater than the semiconductor work function. GaN also has a large bandgap (~3.4eV) and electron affinity (~4.1 eV), and the *p*-GaN work function can be as high as ~ 7.5eV. Therefore, it is challenging to make an ohmic contact using existing low work function metals.

1.2.2 III-Nitride Nanowire LEDs

Commercially available III-nitride planar devices are mostly grown on expensive sapphire or SiC substrates and applications of these planar devices are limited because of all the above-mentioned challenges. To this end, III-nitride nanowires can potentially mitigate some of the problems associated with current nitride planar devices.

1.2.2.1 Motivation and current status. III-nitride nanowires in the form of wurtzite crystal (growth direction c-axis, <0001>) structure grow vertically, perpendicular to the substrates. It shows a unique tendency to relax the strain through the free sidewalls (m-planes) even though significantly lattice-mismatched heterostructures are formed [49, 50]. Nanowire LEDs can be grown spontaneously using MBE on low-cost, CMOS compatible Si substrate with much-reduced defect densities [51, 52]. Selective area growth is another method to achieve nanowire LEDs with well-defined positions and sizes [53]. The emission characteristics of nanowire LEDs grown by the selective area method can be controlled by the position and size of the nanowire array on pre-patterned substrates.

Nanowire LEDs offer an efficient light emission across nearly the entire visible spectral range. The different In composition in InGaN/GaN active regions lead to the

different color emissions. White light LEDs can be achieved by mixing multiple color emissions from a single nanowire [54]. The nanowire structure, having a high surface-to-volume ratio, offers more area for the photons to escape. This results in a higher light extraction which will be described later. Further, to these potential benefits, due to their small size, III-nitride nanowires hold tremendous promise for integration in state-of-the-art optoelectronic and electronic applications. Although the large surface-to-volume ratio of nanowires is advantageous for high light extraction efficiency (LEE), it also causes a high density of surface states. The defect states are introduced in the forbidden bandgap of the semiconductor due to the termination of the crystal structure periodicity at the surface. The performance of a nanowire is limited by the surface states, which can reduce the carrier injection efficiency by capturing carriers from the active region [55]. Currently, EQE and LEE of III-nitride nanowire LEDs have some drawbacks and need to be properly improved.

1.3 Light Extraction Efficiency

Generally, the output power of LEDs is defined by the EQE of the device, which is determined by the LEE together with the internal quantum efficiency (IQE), described previously. To date, however, the LED device performance is severely limited by the low EQE. In the case of planar LEDs, the light extraction is significantly reduced by the total internal reflection, due to the refractive index contrast between the semiconductor material and the air. Recently, various techniques have been developed to increase the LEE, including chip shaping [56], surface roughness [57, 58], patterned sapphire substrate [58], photonic crystal structures [59], graded refractive index material [60], and surface plasmon resonance [61]. The basic principle behind these approaches is to increase the escape cone by expanding the escape surface, or to enable multiple photon entry into the escape cone by surface roughening.

The nanowire structure, having a high surface-to-volume ratio, offers more area for the photons to escape, resulting in a reduction in the total internal reflection. The LEE can be enhanced by guiding the photons towards the nanowire surface. However, in the deep UV LEDs, EQE remains significantly lower than that of the visible LEDs.

The valence band profile of GaN and AlN present different band orders. Although Transverse Electric (TE) emission, perpendicular to the c-axis (E $\perp$ c), is dominant in GaN-based visible LEDs, the portion of Transverse Magnetic (TM) emission, parallel to the c-axis (E || c), in AlGaN based UV LEDs increases significantly with the higher Al composition [62], due to the different band structures of the AlN and GaN at the Γ-point of the Brillouin zone. For the ternary compound $Al_xGa_{1-x}N$, the polarization of the emitted light changes from TE to TM with increasing Al composition. As TM emission gets dominant, it largely prevents light extraction from the top surfaces. For AlGaN LEDs, TM emission becomes dominant for ~ 280 nm or shorter wavelengths. In this case, light can only propagate in-plane and cannot escape from the large area top surface and causes the LEE to be ~10%, or less in the deep UV wavelength range [63]. By careful design of the nanowires, considering several design parameters such as the nanowire diameter, spacing and thickness of the surface passivation layer [64], LEE of ~ 70% is achievable [59].

1.4 Numerical Simulation Methods

The optical and electrical properties of GaN LEDs, including the output power, the electron and hole distributions, and the electric mode profile are numerically calculated using different simulation tools and models. Finite Difference Time Domain (FDTD) has been successfully applied to optimize the design of the nanowire LEDs and calculated the Poynting vectors to determine the light extraction efficiency of GaN LEDs. Further studies

on the unique characteristics of nanowire LEDs are performed using the advanced LED device simulation software Advanced Physical Models of Semiconductor Devices (APSYS) by simulating the energy band diagram and carrier distribution in the device active region. Using APSYS, critical parameters related to the device performance can be calculated, which includes energy band diagram, wave functions, carrier distribution, electron overflow, recombination rate of various processes, power, etc.

1.5 Organization of Dissertation

This dissertation focuses on improving the performance of nanowire-based LEDs in the visible and UV regions by studying the optical and electrical characteristics intensively. Moreover, the III-nitride-based resistive random-access memory (RRAM) is studied to understand the switching capability of III-nitride materials. Chapter 1 provides an overview of LEDs where the need of III-nitride LEDs along with the challenges in the III-nitride-based planar LEDs are presented. The advantages of III-N nanowire LEDs as compared to planar LEDs are described. Additionally, the current status of the nanowire LEDs is presented. Further, an overview of the theoretical methods utilized for the simulation is included.

The improvement in the performance of phosphor-free InGaN/GaN-based white light nanowire LEDs is demonstrated by replacing the EBL with coupled quantum wells in Chapter 2. The light output power and EQE of white LEDs were increased and efficiency droop was reduced due to a significant reduction of electron overflow.

In Chapters 3, 4, and 5 electron leakage problem, a primary reason for efficiency droop in deep-UV LEDs is addressed by engineering the LED structures. In Chapter 3, the electron leakage problem is addressed by engineering the EBL, whereas in Chapter 4, the

concave quantum barriers (QBs) are introduced to overcome this problem. In Chapter 5, an EBL-free AlGaN deep UV LED structure is designed using graded staircase QBs instead of conventional QBs without affecting the hole injection efficiency. As a result, all three structures reduce the electron leakage to the *p*-GaN region and improve the device performance by enhancing the radiative recombination in the active region.

In Chapter 6, the high crystalline quality of AlInN nanowire LED structures with stable and strong EL emission in the UVB region is demonstrated. Further, an improved LEE for these LEDs is demonstrated using different photonic crystal structures.

In Chapter 7, III-nitride, particularly AlN-based RRAM devices are studied to analyze the switching capability of AlN for different device sizes and various thicknesses of the AlN layers.

Finally, Chapter 8 presents the conclusion and future outlook of this dissertation.

CHAPTER 2

HIGH-PERFORMANCE InGaN/GaN NANOWIRE WHITE LIGHT-EMITTING DIODES WITHOUT AN ELECTRON-BLOCKING LAYER

2.1 Introduction

InGaN compound semiconductor alloys have been intensively studied for SSL technology. InGaN-based white color LEDs (white-LEDs) have attracted great attention because of their tremendous energy saving potentials [4, 65], well suitable for liquid crystal displays [66, 67] and lighting. Typically, white LEDs can be created with the combination of discrete monochromatic LEDs [68], and color rendering can be controlled by their light mixing. One main approach for white LEDs is based on phosphor conversion [69], typically realized by the luminescence down conversion using phosphor converters such as cerium-doped yttrium aluminum garnet. The conversion efficiency of phosphor-based white LEDs is typically poor due to the Stokes effect.

As compared to the conventional planar structures, III-nitride nanowires exhibit significant advantages including greatly reduced dislocation densities and polarization fields, due to the effective lateral stress relaxation. Additionally, nanowire LED with the incorporation of quantum dots (QDs)/disks in the active region lead to high efficiency with tunable emission [70, 71]. However, nanowire LEDs still contain several challenges for further improving the quantum efficiency and light output power, which may include the inefficient carrier confinement in the active region, nonuniform carrier distribution [72], electron overflow [41], and the presence of large densities of states and defects along the wire lateral surfaces [73]. Recently, the presence of electron overflow and its effect on the nanowire LED performance are addressed [41]. It is understood that at high injection

current levels, one of the primary reasons for the efficiency droop is electron overflow and it strongly influences the output characteristics of white LEDs. For the emerging nanowire LED technologies, the device performance is more susceptible to carrier leakage/electron overflow than those based on conventional planar heterostructures, due to very large surface-to-volume ratios. Recent research shows the role of carrier leakage and electron overflow in the efficiency droop of GaN planar LEDs [74]. It is even worse in nanowire ones due to highly non-uniform Indium distribution along the lateral dimension and consequently flowing the current in the near-surface GaN region. Due to the heavy effective mass and small mobility, the hole injection in the InGaN/GaN nanowire heterostructures is highly non-uniform. The holes reside close to the *p*-doped GaN layer, while electrons have a relatively uniform distribution in the active region. Auger recombination and electron overflow are enhanced by highly non-uniform carrier distribution, and consequently adversely affect the device performance. Non-radiative recombination occurs in *p*-type GaN region due to the recombination of inefficient holes injected and electron leakage.

Recently, some different methods were proposed to prevent electron overflow, including *p*-type modulation-doped active region to enhance the hole transport, thin InGaN barrier [75], inserting a *p*-type AlGaN layer between the *p*-type GaN layer and active region known as an EBL [76]. However, *p*-type AlGaN with a high Al content may form a high barrier and positive sheet polarization charges at the heterointerface of the last QB/EBL [77, 78], resulting in the low hole injection into the LED active region. To reduce electron overflow without using an AlGaN EBL, it is obvious that the electron should be slowed down before injecting it to the active region. The structure with stepwise increased In

composition was utilized between the *n*-side and the active region of LED to reduce the electron overflow [79]. Inserting a layer with the lower In composition reduces the kinetic energy and velocity of the injected electron. Moreover, by inserting this layer before the active region, hot electrons are thermalized by interacting with longitudinal optical (LO) phonons [80]. In this context, a new method is proposed which utilizes InGaN quantum well between the QD active region and *n*-GaN to reduce electron overflow. Incorporating different compositions of InGaN QDs results in an intrinsic white LED. The blue, green and red light from self-organized QDs incorporated in a single GaN nanowire with various In compositions emit stable white light emission. A detailed study has been performed, both theoretically and experimentally, of electron overflow in InGaN/GaN dot-in-a-wire white LEDs, wherein an InGaN well is incorporated between *n*-GaN and device active region to effectively control electron overflow. Furthermore, to utilize the electrons escaped from the active region, a second InGaN quantum well is employed between the active region and *p*-GaN to reduce electron loss to the *p*-GaN and contribute blue light emission to relatively control the white light emission from the LED device. Consequently, high internal quantum efficiency InGaN/GaN nanowire LEDs of 58.5% with stable white-light emission was demonstrated.

2.2 Device Design and Simulation

The effect of coupled quantum wells incorporated in InGaN/GaN white LEDs is studied using Crosslight APSYS 2018 simulation software. For this study, a total of three InGaN/GaN nanowire LED structures are considered, schematically illustrated in Figure 2.1. The first device is denoted as LED1, consists of a 200 nm thick *n*-GaN nanowire template, 10 MQWs of 3 nm GaN QB/ 3 nm InGaN QW in the active region and a 100 nm thick *p*-GaN. The second structure is denoted as LED2, has a similar structure as LED1 except that an EBL of 10 nm thick *p*-doped $Al_{0.1}Ga_{0.9}N$ is introduced in between the active region and *p*-GaN layer. Finally, the proposed structure, LED3 has the same structure as LED1, but with an extra 30 nm thick *n*-doped $In_{0.20}Ga_{0.8}N$ layer incorporated in between the *n*-GaN template and the active region. Moreover, it has an extra 10 nm thick *p*-doped $In_{0.2}Ga_{0.8}N$ quantum well in between the active region and *p*-GaN layer.

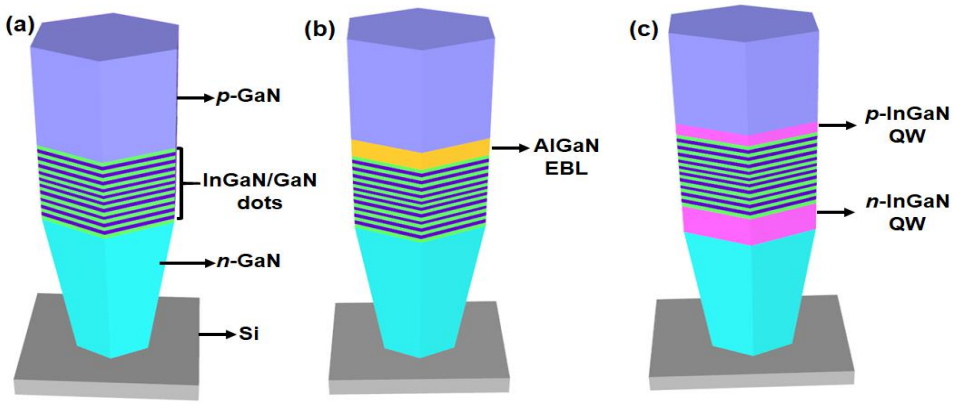

Figure 2.1 Schematic structures of (a) LED1, (b) LED2, and (c) LED3.

The *n*-doped QW incorporated before the active region helps to control the electron transportation into the active region. Detailed studies further confirm that the InGaN QW can significantly reduce electron overflow through the near-surface GaN region. Compared

to the commonly used AlGaN EBL between the device active region and *p*-GaN, the incorporation of a suitable *p*-doped InGaN quantum well between *p*-GaN and the active region does not adversely affect the hole injection process. Moreover, the overflowed electrons from the active region can be utilized by *p*-doped QW to recombine with holes and contribute to white light emission. As the electron effective masses are much lighter than those of holes and consequently have higher thermal velocities, some electrons are not captured and recombine in the active layer and resulting in efficiency reduction. To increase the efficiency of the proposed LED structure, the capture rates for electrons and holes in the active layer should be accelerated. The first quantum well which is closed to the *n*-GaN segment is employed to control electron flow in the active region while another is used to utilize electron leakage out of the active region for the blue light emission. The *n*-GaN section as an electron emitter is coupled to the active region via a barrier. Electron current flows from the *n*-GaN section into the electron injector QW which acts as a current spreading layer, then electrons tunnel through the barrier into the active region and recombine with the holes. The electron injector QW suppresses the electron leakage into the *p*-GaN segment and eliminates the undesired light generated outside the active region.

Figures 2.2(a) and (b) present the distribution of electron and hole concentrations across the device structures, respectively. Figure 2.2(c) shows the radiative recombination rates in different LED structures at 750 A/cm^2. It is consistent with the previous findings that in typical MQWs active region based InGaN/GaN LEDs, both electrons and holes concentrations are high in the QW closest to the *p*-doped region and dominant radiative recombination also occurs therein [77]. In the case of LED2, EBL mitigates the electron overflow into the *p*-region up to some extent and carrier concentration in the active region

is slightly higher compared to LED1. However, in the case of LED3, the *n*-doped QW is able to trap the electrons which leads to slower electron flow and can be observed from Figure 2.2(a). Moreover, in this LED, the carrier transportation is controlled by both QWs and leads to having additional radiative recombination in these QWs along with the active region as shown in Figure 2.2(c). The total radiative recombination of LED3 is $6.33\times10^{30}/cm^3s$ which is higher than other LEDs as the total radiative recombination of LED1, and LED2 are $4.59\times10^{30}/cm^3s$, and $5.74\times10^{30}/cm^3s$, respectively.

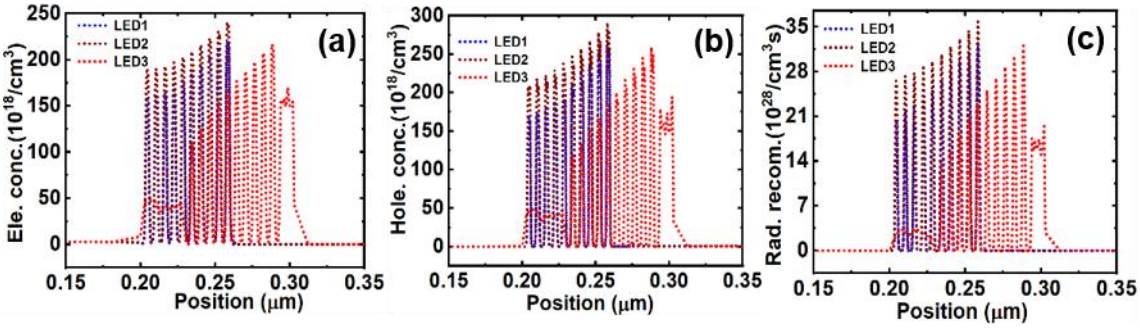

Figure 2.2 (a) Electron concentration, (b) hole concentration, (c) radiative recombination of different simulated LED structures.

It is well known that in nitride-based LEDs, electrons have relatively low effective mass as compared to holes and thus very high mobility and insufficient carrier confinement capability of QW barriers [81] cause electrons to easily escape from the QW active region and enter the *p*-type region. To estimate the electron leakage current, the electron current density of LEDs is calculated and is shown in Figure 2.3(a). LED3 has less electron leakage from the active region compared to other devices, which supports the above-mentioned results. Hence consumption of holes in the *p*-region is reduced due to less electron overflow into the *p*-region that enhances the hole injection efficiency into the active region, which can be understood from Figure 2.3(b). Due to the reduction of electron overflow and

improvement of hole injection efficiency in the case of electronically coupled quantum well LED (LED3), the IQE and output power are also improved compared to other cases and shown in Figures 2.3(c) and 2.3(d).

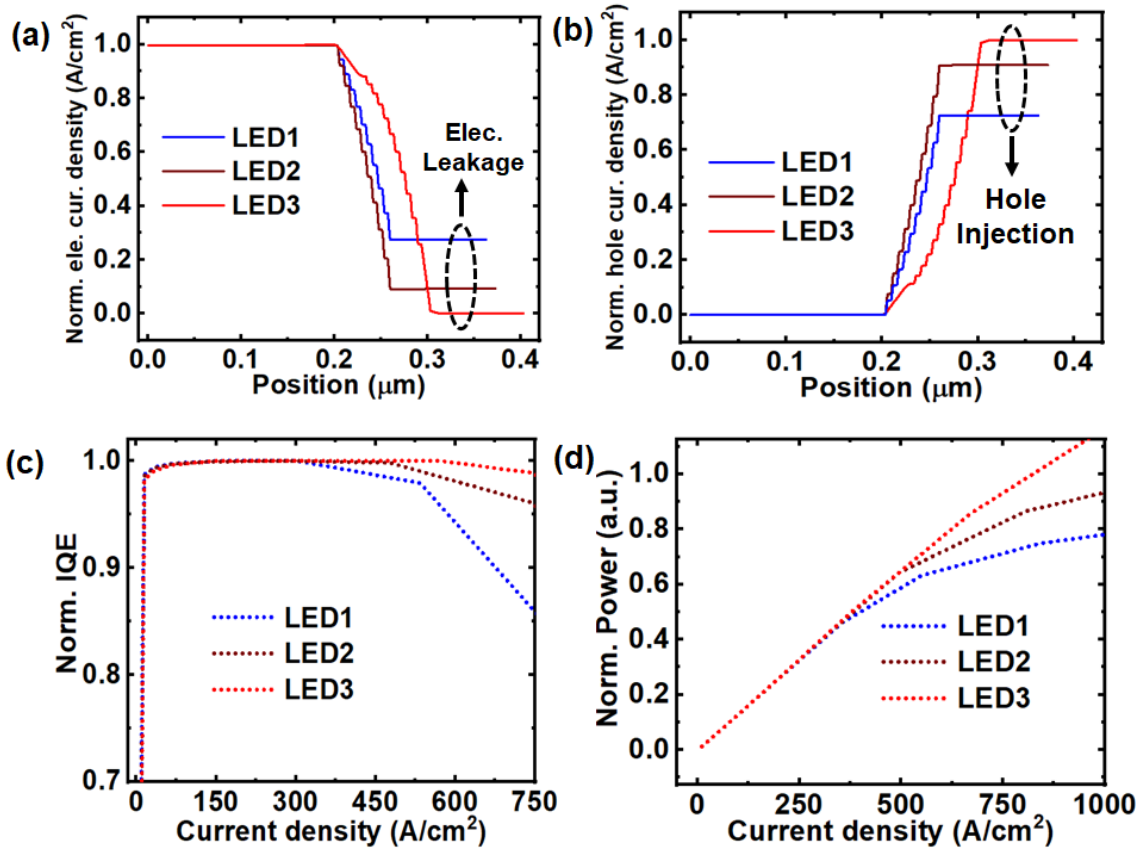

Figure 2.3 Normalized (a) electron current density, (b) hole current density, (c) internal quantum efficiency, (d) L-I characteristics of different simulated LED structures.

2.3 Theoretical Model

The detailed mechanisms of the InGaN coupled quantum wells on the improvement of the LED performance are theoretically investigated through the mean free path (l_{MFP}) model. For this study, LED1 and LED3 are considered. The schematics of the energy band diagrams of LED1 and LED3 are depicted in Figures. 2.4(a) and 2.4(b), respectively, along with four electron transport processes in the active region. Illustrated in Figure 2.4, the incoming electrons are scattered and fall into the quantum wells denoted by process 1.

Some of those fallen electrons recombine with the holes radiatively as well as with the crystal defects as depicted by process 2, while remaining electrons escape from the QWs and become free again as illustrated by process 3. In addition, some electrons with longer l_{MFP} travel to a remote position without being captured by the quantum wells as depicted by process 4. The l_{MFP} of these electrons needs to be reduced so that the carrier concentration in the QWs would be increased that would favor the higher radiative recombination rate in the active region by reducing the electron overflow. Here, we have considered the total number of electrons injected into the *n*-GaN region to be N_0 for both LED structures.

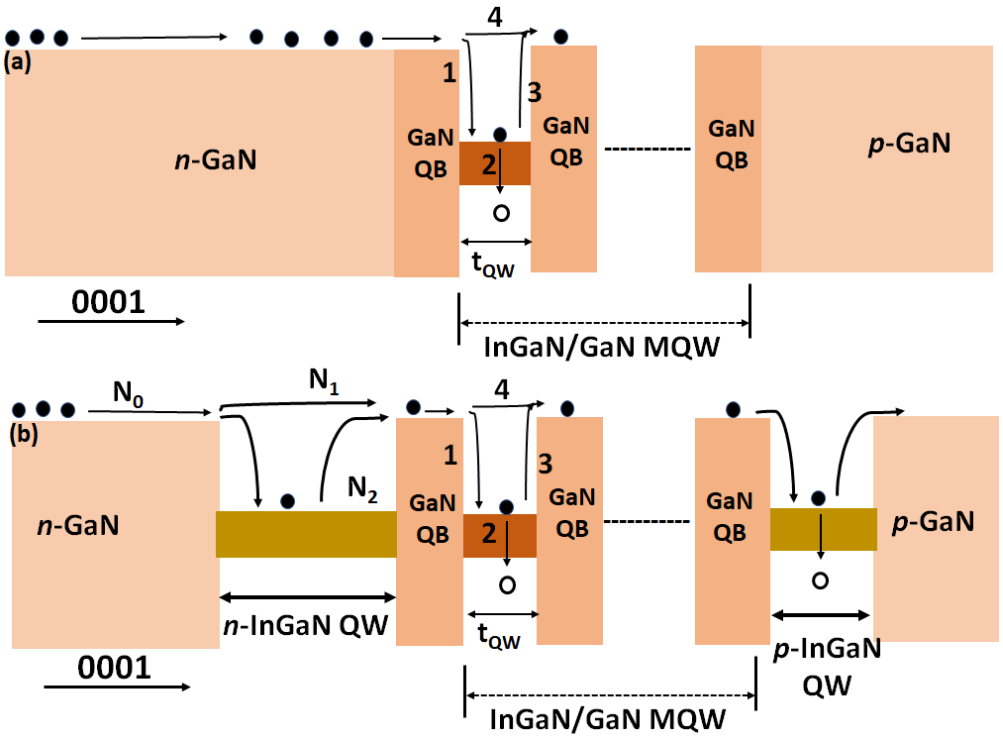

Figure 2.4 Schematic energy band diagrams for (a) LED1 and (b) LED2.

For the simplicity of the model, electron loss through non-radiative recombination is neglected. Also, the hole concentration in the *n*-InGaN layer between *n*-GaN and active

region in the case of LED3 is much lower than the electron concentration, so the electron loss through radiative recombination with holes is also negligible. It is assumed that out of N_o electrons, N_2 electrons captured by the first extra QW undergo thermalization with LO phonon emission, while remaining electrons denoted as N_1, directly travel over the extra QW layer without undergoing thermalization. The captured electrons in the quantum wells are correlated with the electron l_{MFP} [82]. To increase the number of the quantum well-captured electrons, the electron l_{MFP} within the InGaN/GaN MQWs region must be reduced. To understand the working mechanism of the extra QW before the active region in LED3 in reducing l_{MFP}, electron l_{MFP} in both the LEDs are calculated, which is a function of thermal velocity (v_{th}) and the scattering time (τ_{sc}) set to 0.0091ps [83, 84], as shown in Equation (2.1). v_{th} can be further expressed as shown in Equation (2.2). For LED3 with an extra QW *n*-InGaN before the active region, the expression for v_{th} will be as shown in Equation (2.3).

$$l_{MFP} = v_{th} \times \tau_{sc} \tag{1.5}$$

$$v_{th} = \sqrt{2 \times [E]/m_e} \tag{1.6}$$

$$v_{th\_eQW} = \sqrt{2 \times [E + \Delta E_c + qV - \hbar\varpi_{LO} - \Delta E_c]/m_e]}$$

$$= \sqrt{2 \times [E + qV - \hbar\varpi_{LO}]/m_e]} \tag{1.7}$$

In Equations (2.2) and (2.3), E represents the energy of the electron before getting into the QW i.e., electron energy in the *n*-GaN layer, m_e is the effective mass of electrons. $-\hbar\omega_{Lo}$ means the energy loss by phonon emission, qV is the work done to the electrons by the polarization induced electric field in the extra QW. The first ΔE_c in Equation (2.3) represents the kinetic energy received by the electrons when jumping over the conduction

band offset between *n*-GaN and *n*-$In_{0.2}Ga_{0.8}N$ extra QW and $-\Delta E_c$ represents the energy loss by the electrons when climbing over the conduction band offset between *n*-$In_{0.2}Ga_{0.8}N$ and the GaN layer. Here it is assumed that the thermionic emission process dominates over the intra-band tunneling during the electrons transport into the active region, thus ΔE_c can be eliminated, as shown in Equation (2.3). The energy loss through LO phonon emission i.e., $-\hbar\omega_{Lo}$ is considered to be 92 meV [85] and qV = $\int_0^{t_{eQW}} q \times E(y)dy$ is calculated from the electric field as shown in Figure 2.5. Value of qV is found to be 47 meV. To understand the effect of extra QW to reduce the electron MFP, it can be understood from Equations (2.2) and (2.3) that $E + qV - \hbar\omega_{LO} < E$. As qV is 47 meV and $\hbar\omega_{Lo}$ is 92 meV, overall $E + qV - \hbar\omega_{LO} < E$ due to which $v_{th\_eQW} < v_{th}$ and $l_{MFP\_eQW} < l_{MFP}$. This shows that the extra quantum well before the active region has a significant effect in reducing the electron l_{MFP} in the active region, and consequently increasing capture efficiency of electrons in the QW and reducing the possibility of electron leakage as shown in Figure 2.3 (a) above.

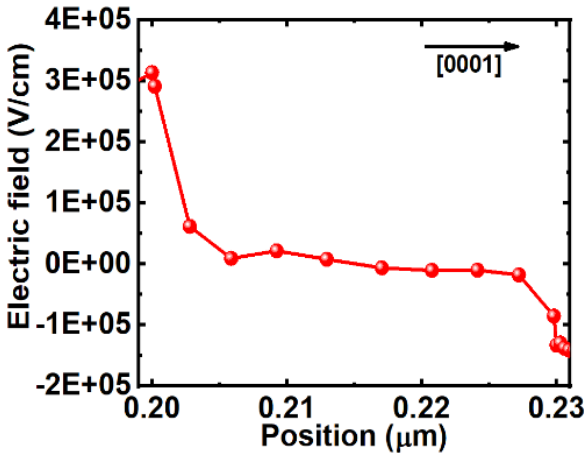

Figure 2.5 Calculated electric field as a function of position within the n-InGaN layer at 900 mA.

2.4 Molecular Beam Epitaxial Growth of InGaN/GaN Nanowire Heterostructures on Si (111) and Fabrication

The experiment throughout this study was designed according to the results obtained from the simulation. Vertically aligned InGaN/GaN dot-in-a-wire heterostructures, illustrated in Figure 2.1, were grown on Si (111) substrates by radio-frequency Veeco Gen II MBE under nitrogen-rich conditions. GaN nanowires were grown at ~ 730°C; nitrogen flow rate was kept at 1 sccm with a forward plasma power of ~ 350W. The grown nanowires are vertically aligned to the substrate and exhibit uniform height. The device's active region contains ten InGaN/GaN QDs which were grown at relatively lower temperatures (550–600°C) to enhance In incorporation in the dots. InGaN QD thickness is ~ 3 nm and capped by ~ 3 nm GaN layer. For LED2, the AlGaN EBL layer was grown at 800^{o}C with the same conditions of plasma power and nitrogen flow rate as that for LED1. For LED3, the device active region is sandwiched by two InGaN/GaN quantum wells which were grown at 630^{o}C to control electron flow in the active region and utilize electron leakage out of the active region for the blue light emission. As shown in Figure 2.6(a), a 45^{o} tilted scanning electron microscopy (SEM) image of the LED3 grown on Si (111), the wire diameters and densities are in the range of 60 nm to 100 nm and ~1×10^{10} cm^{-2}, respectively. The scanning transmission electron microscope (STEM) (inset in Figure 2.6(b)) clearly shows two InGaN quantum wells and ten QDs in the device active region. The scanning electron dispersive spectra of the red line in the inset were shown in Figure 2.6(b), and the distribution of indium in quantum wells and ten dots were confirmed. Strong photoluminescence (PL) intensity has been measured for these nanowire LEDs as shown in Figure 2.7(a). The peak emission wavelength at ~430 nm originates due to the emission

from the electronically coupled quantum wells while the emission peak at ~550 nm corresponds to the emission from the QD active region.

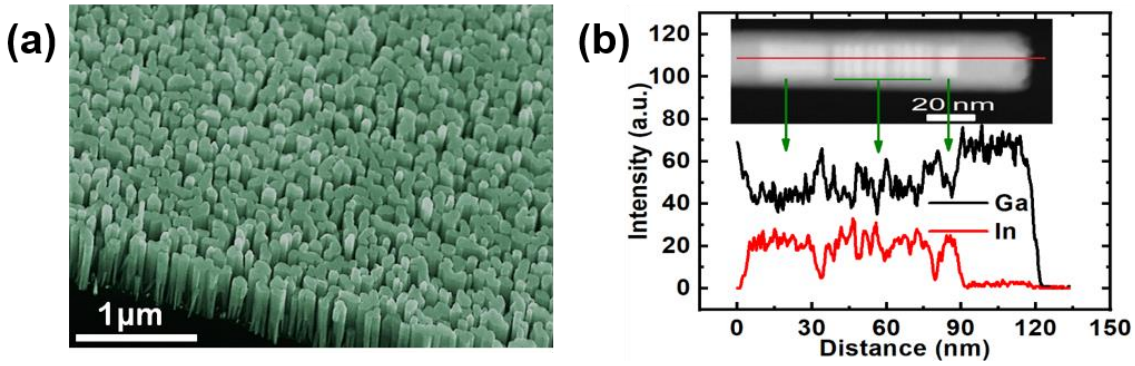

Figure 2.6 (a) 45^{o} tilted SEM image of LED3 on Si substrate. (b) annular dark-field STEM image and EDXS signals for In and Ga of LED3.

The nanowire LED fabrication process includes the following steps. First, a polyimide resist was spin-coated to fully cover the nanowires, followed by O_2 plasma etching process to expose the top portion of nanowires. Thin Ni(5nm)/Au(5nm) and Ti(20nm)/Au(120nm) layers were deposited on the nanowire surface and backside of the Si substrate, respectively. A 200 nm indium tin oxide (ITO) layer was coated on the device top surface to serve as a transparent electrode and current spreading layer. The fabricated devices with Ti/Au and Ni/Au contacts were annealed at 500^{o}C for 1 min in a nitrogen ambient, while the complete devices with ITO contacts were annealed at 300^{o}C for 1 hour in a vacuum. The device area is ~ 300×300 μm^2.

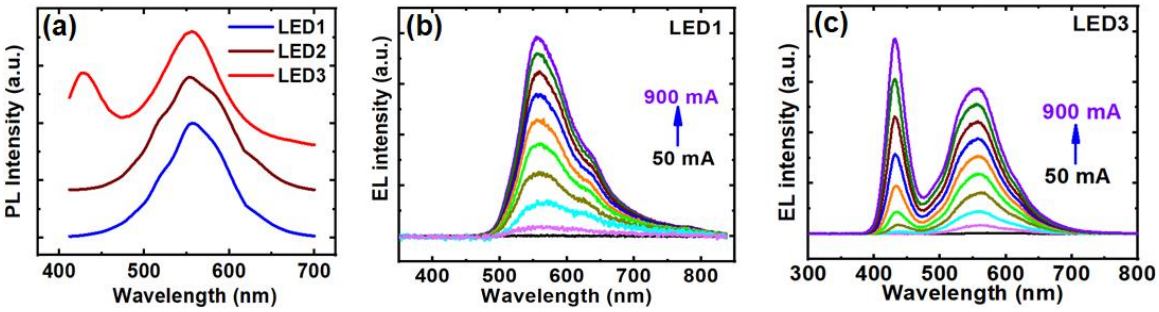

Figure 2.7 (a) Normalized photoluminescence spectra of four LEDs measured at 300K. (b) room temperature electroluminescence spectra of LED1 measured at different injection currents. (c) room temperature electroluminescence spectra of LED3 measured at different injection currents.

Figures 2.7(b) and 2.7(c) shows the normalized electroluminescence (EL) spectra of LED1 and LED3 under various injection currents, respectively. The peak at ~550 nm related to the emission from the QD active region well coincides with the photoluminescence results shown in Figure 2.7(a). It is obvious that the emission at ~430 nm becomes progressively stronger with increasing current due to the carrier recombination in the InGaN/GaN QWs at a higher current. This shows the role of InGaN/GaN QWs in emission characteristics of the LED; at higher current, more injected electrons can escape from the QD active region and have more chance to recombine with holes in InGaN/GaN QWs. The electroluminescence spectra cover the whole visible range and show the balanced RGB distribution. Under the different applied currents, the spectroscopic shape is slightly changed, exhibiting acceptable stability. Experimentally, we have also demonstrated electron overflow can be effectively controlled in those nanowire LEDs. In addition, a blue-emitting InGaN quantum well is incorporated between the QD active region and *p*-GaN, wherein electrons escaping the device active region can

recombine with holes to contribute to white-light emission. The resulting device exhibits highly stable emission characteristics, illustrated in Figure 2.7(c) which is for LED3.

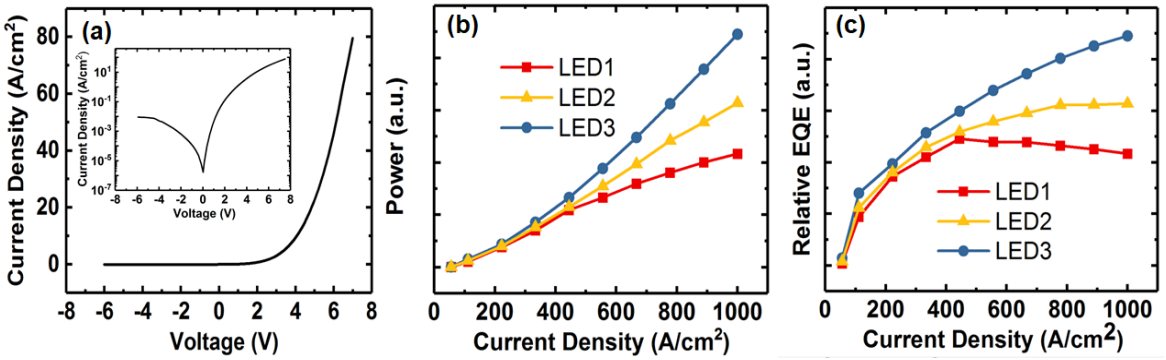

Figure 2.8 (a) Room temperature current-voltage curve of LED3. (b) Light-current curves measured for LED1 and LED3 at room temperature. (c) Normalized EQEs measured for LED1 and LED3 at room temperature.

The fabricated LED3 devices exhibit excellent current-voltage characteristics with a very small leakage current which is just ~8 μA at -6 V, presented in Figure 2.8(a) which is for LED3. The output powers of LED1, LED2 and LED3 are shown in Figure 2.8(b). It is seen that LED3 demonstrates the highest output power which agrees well with the simulation results presented in Figure 2.3(d). Moreover, no efficiency droop was observed in LED3 up to injection current density of 1000 A/cm^2, shown in Figure 2.8(c). In addition, shown in Figure 2.9, the IQE of LED3 was measured to be ~ 58.5% by comparing the PL intensity of this LED at 300K and 10K by assuming that the emission of the LED at 10K is unity. The loss mechanism in this LED is further studied by using ABF model which is described by Equation (2.4).

$$\eta_i = \frac{BN^2}{AN + BN^2 + f(N)} \tag{1.8}$$

where N, A, B and $f(N)$ are the carrier density of the active region, the SRH nonradiative recombination, radiative recombination coefficients, and other higher-order effects such as Auger recombination and carrier leakage outside of the active region, respectively [34, 35]. The values of A, B, and C are calculated as 2.9×10^{8} s^{-1}, 5×10^{-10} $cm^{3}s^{-1}$, and 1×10^{-35} $cm^{6}s^{-1}$ at 300K, respectively. These values agree well with those calculated for other nanowire LEDs, previously proposed [41]; compared to that LED, the value of C is smaller which confirms the drastic reduction of electron overflow by the electron injector quantum well.

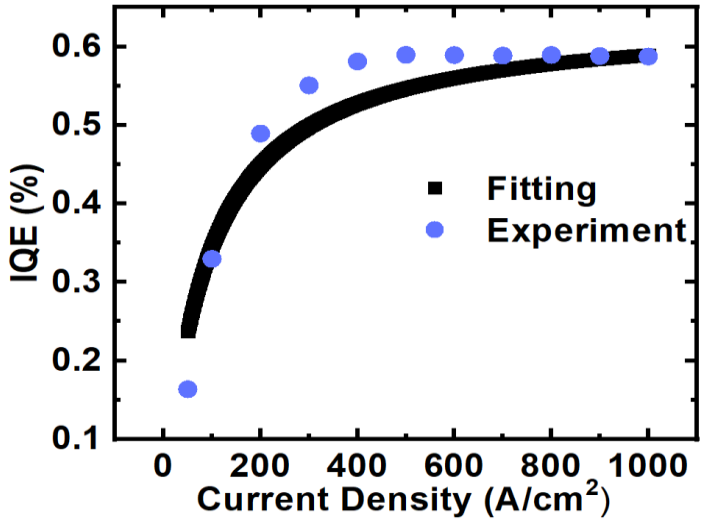

Figure 2.9 Internal quantum efficiency of LED3 and its fitting curve (black square) using ABF model.

The quantum efficiency of proposed LEDs reaches its peak value at significantly higher current densities ~300A/cm^2, compared to that of conventional InGaN/GaN quantum well blue-emitting LEDs ~20A/cm^2 [86, 87]. Nonradiative surface recombination caused by the very large surface-to-volume ratio of nanowires results in a higher SRH recombination coefficient as compared to InGaN/GaN quantum well blue-emitting LEDs [38, 39].

2.5 Conclusion

In summary, we have demonstrated highly efficient and truly white LEDs using InGaN/GaN dot-in-a-wire structure with the usage of two additional InGaN quantum wells. The coupled *n*-InGaN QW incorporated between the *n*-GaN and active region improves the electron capture efficiency in the multiple quantum wells by reducing l_{MFP} after electrons undergo thermalization by phonon emission in the *n*-InGaN QW. Further, the *p*-InGaN after the active region captures the leaked electrons and contributes to the white light emission by radiatively recombining with the holes. In conclusion, using the coupled InGaN quantum wells allows reducing electron leakage into the *p*-GaN segment, enhancing the electron capture into the active region and eliminating the undesired light generated outside the active region; consequently, increasing the efficiency of the InGaN/GaN dot-in-a-wire LEDs with remarkably stable white-light emission.

CHAPTER 3

ENGINEERING THE ELECTRON-BLOCKING LAYER FOR AlGaN DEEP-ULTRAVIOLET LIGHT-EMITTING DIODES

3.1 Introduction

AlGaN UV-LEDs have been explored extensively due to the possibility of several applications including water purification, food/air sterilization, biochemical detection, analytical sensing, polymer curing, phototherapy and others [88-90]. These LEDs exhibit many advantages including compact in size, low power consumption, long-lifetime, very quick response time, optical tunability across the entire UV region, non-toxic material composition, making them a potential alternative candidate to the traditional bulky and toxic mercury-based UV-light sources [91, 92]. Though AlGaN UV LEDs are well studied, their performance in terms of optical output power and efficiency in deep UV regime (wavelength below 280 nm) is still poor and needs to be improved to utilize them in practical applications. The anticipated reasons behind diminished performance could be a poor material quality causes the presence of defects and dislocations, extremely inefficacious *p*-doping [93], increased polarization fields, poor hole injection, electron overflow [41] from the active region, and others.

To address all the above-mentioned issues, better epitaxial growth techniques have been evolved with reduced dislocation density [94]. Also, different band-engineered structures such as staggered quantum wells [95], semi-polar structures [96], and intrinsic strip-in-a-barrier structures [97, 98] have been proposed to address electron overflow. On the other hand, EBL which is a *p*-doped higher Al composition AlGaN layer has been

introduced between the active region and *p*-region to improve the electron confinement in the active region and reduce the electron leakage from the active region [99, 100]. However, if this EBL is not designed appropriately, it can affect the hole injection into the device active region severely due to the large valence band offset at the hetero-interface and formation of positive polarization sheet charges [97, 98, 101]. Therefore, engineering or optimizing EBL is crucial to have reduced electron leakage without affecting the hole injection.

The EBL has been optimized in different ways to achieve suppressed leakage and better hole injection efficiency. Superlattice (SL) structures were demonstrated to improve the hole activation efficiency by reducing the Mg activation energy which is by utilizing the band offset and strong built-in spontaneous and piezoelectric polarization fields instead of thermal energy [102-105]. Moreover, parabolic graded structures are implemented to result in low resistances for transport across the barriers when compared to interfaces with abrupt composition changes [102]. Here, a double-sided step graded superlattice EBL (DSGS-EBL) LED structure is designed, operating at 254 nm wavelength which is effectively used for germicidal disinfectants, water/air sterilization and other applications [106, 107].

3.2 Device Structure

The reference structure for this study is a conventional EBL-based LED as shown in Figure 3.1(a), denoted as LED1. Grown on a *c*-plane AlN template, LED1 consists of a 3 μm thick *n*-$Al_{0.7}Ga_{0.3}N$ layer (Si: 5×10^{18} cm^{-3}), followed by an active region containing five pairs of 3 nm intrinsic $Al_{0.6}Ga_{0.4}N$ QW and 12 nm intrinsic $Al_{0.7}Ga_{0.3}N$ QB layers, then a 20 nm *p*-$Al_{0.85}Ga_{0.15}N$ EBL (Mg: 3×10^{19} cm^{-3}), succeeded by a 100 nm *p*-$Al_{0.7}Ga_{0.3}N$ hole

injection layer (Mg: 2×10^{19} cm^{-3}), and finally a 20 nm *p*-GaN contact layer (Mg: 1×10^{20} cm^{-3}). Figures 3.1(b)-3.1(d) illustrate the Al composition profile in the conduction band for the conventional EBL of LED1, double-sided step graded (DSG) EBL of LED2, and double-sided step graded superlattice (DSGS) EBL of LED3.

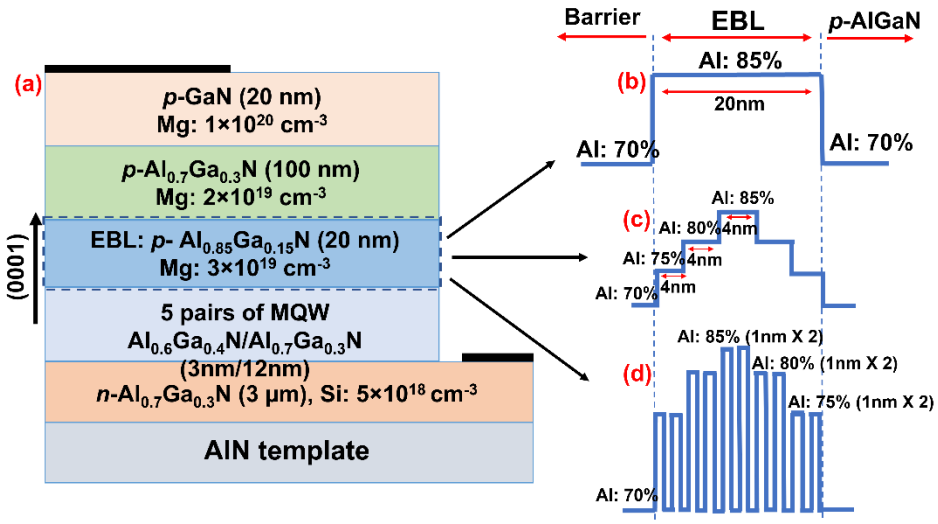

Figure 3.1 (a) Schematic diagram of LED1, Al composition in the conduction band of (b) conventional EBL in LED1, (c) DSG-EBL in LED2, (d) DSGS-EBL in LED3.

The double-sided step graded (DSG) EBL of LED2 consists of three symmetrical steps on both the last QB (LQB)/EBL interface and EBL/ *p*-$Al_{0.7}Ga_{0.3}N$ interface sides as shown in Figure 3.1(c). The Al composition of three symmetrical AlGaN steps are 75%, 80% and 85% and the thickness of each step is 4 nm. The novel double-sided step graded superlattice (DSGS) EBL is integrated into LED3 as shown in Figure 3.1(d). The DSGS comprises of three symmetrical steps on both LQB/EBL interface and EBL/ *p*-$Al_{0.7}Ga_{0.3}N$ interface sides, in which each step has a two-period of a superlattice of $Al_xGa_{(1-x)}N$/QB layers. The values of x are 0.75, 0.80, and 0.85 and the thickness of each layer is 1 nm. It is expected that the DSGS EBL would reduce the polarization at the interface of LQB and EBL due to the reduced lattice mismatch between the layers. The chip area of all LED

structures is considered as 400 μm × 400 μm and designed to emit 254 nm wavelength UV light.

3.3 Device Parameters

The following parameters have been considered in this work. The considered value of the bandgap for AlN is 6.3 eV and for GaN is 3.42 eV [108]. The bowing parameter and band offset ratio of AlGaN are assumed to be 0.94 eV, and 0.67/0.33, respectively [109]. The energy band diagrams of all three LEDs are estimated using 6×6 *k.p* model [110]. The non-radiative and radiative recombination have been taken into account by considering the SRH recombination lifetime, radiative recombination coefficient, Auger recombination coefficient and light extraction efficiency are considered as 15 ns, 2.13×10^{-11} cm^3/s, 2.88×10^{-30} cm^6/s, and 15%, respectively [111]. Also, the activation energy of Mg-doped *p*-$Al_{0.85}Ga_{0.15}N$, *p*-$Al_{0.7}Ga_{0.3}N$ and *p*-GaN is considered as 459 meV, 408 meV and 170 meV, respectively [112, 113]. The activation energy of Si-doped *n*-$Al_{0.7}Ga_{0.3}N$ is set as 15 meV [114]. In addition, the tunneling model is incorporated in LED2 and LED3. The degree of polarization due to spontaneous and piezoelectric polarization is estimated using the methods proposed by Fiorentini *et al.* [115] and considered 50% of the theoretical value in our model. The internal absorption loss is assumed as 2000 m^{-1} and all simulations are performed at room temperature.

3.4 Results

To understand the carrier transport improvement in LED3 i.e., the proposed DSGS EBL structure, the performance of LED1, LED2 and LED3 are studied and corresponding EQE and output power are presented in Figure 3.2. As illustrated in Figure 3.2(a), a maximum

EQE of 5.83% is exhibited by LED3, where EQE in LED1 and LED2 are only 2.99% and 5.7%, respectively. Moreover, the minimum EQE droop, defined as $(\eta_{peak}- \eta_{60mA})/ \eta_{peak}$, is found in the case of LED3 which is only 9.1% at 60 mA injection current as compared to 49.8% and 32.1% for LED1 and LED2, respectively. The reason behind this improved radiative recombination and reduced carrier leakage in LED3, due to the superior carrier confinement [52] provided by the DSGS structure. As shown in Figure 3.2(b), the output power as a function of injection current, LED3 shows 3.56 times higher output power as compared to LED1 at 60 mA injection current. Different output parameters for the three structures are compared in Table 3.1.

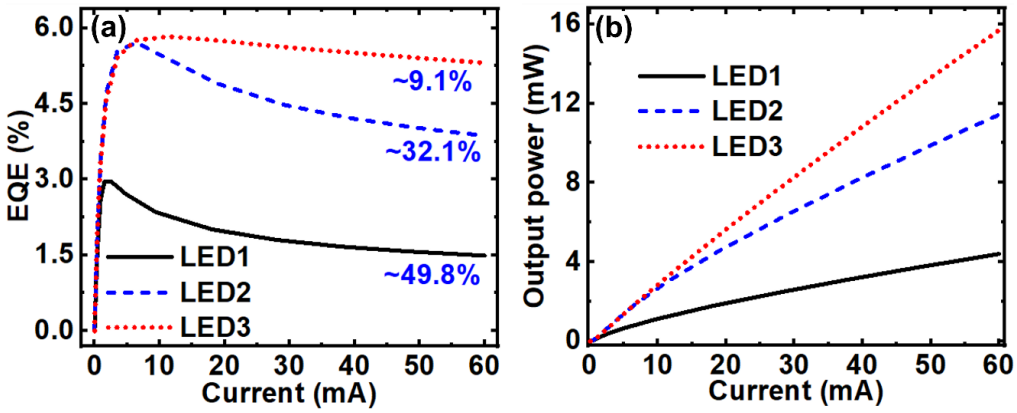

Figure 3.2 (a) EQE and (b) output power for LED1, LED2 and LED3 as a function of injection current.

Table 3.1 Comparison of EQE and Output Power of LED1, LED2 and LED3

LED Structures	Max. EQE (%)	EQE (%) at 60 mA	EQE droop (%)	Output power (mW) at 60 mA
LED1	2.99 at 2.55 mA	1.5	49.8	4.4
LED2	5.7 at 6.49 mA	3.87	32.1	11.42
LED3	5.83 at 11.54 mA	5.3	9.1	15.68

The underlying mechanism behind the improved EQE and output power in the proposed structure is further analyzed using the energy band diagram and the quasi-fermi level of the three simulated structures at an injection current of 60 mA as shown in Figures 3.3(a)-3.3(c). The effective conduction band barrier height (φ_e) for LED1, LED2 and LED3 is found to be 231 meV, 259 meV and 288 meV, respectively. The large value of φ_e in LED3 compared to LED1 and LED2 effectively prevents the electron overflow and efficiently reduces the electron leakage into the *p*-region. In addition, as shown in Figure 3.3(d), the proposed structure, LED3 shows the smallest parasitic electron reservoir volume at the interface of LQB and EBL. This is because of the reduction in the piezoelectric polarization field at the interface due to the superlattice structure, which can further suppress the electron overflow [116]. This improves the hole concentration in the *p*-region because of reduced non-radiative recombination. Further, superlattice structure in LED3 facilitates improved hole activation by utilizing the band offset and strong built-in spontaneous and piezoelectric polarization fields within the EBL layer instead of thermal energy as shown in Figure 3.4, thus reducing the acceptor activation energy [102, 105, 117]. In the superlattice structure of sufficiently thin layers, Mg atoms are ionized in the $Al_xGa_{1-x}N$ and holes tend to accumulate in the $Al_yGa_{1-y}N$ layers for the structure of $Al_xGa_{1-x}N/Al_yGa_{1-y}N$ layers with x>y. This allows hole transport both in vertical and lateral directions [117]. Also, LED3 supports reduced cracks and dislocations as the layer thickness is below the critical thickness so that elastic strain is not relieved by the formation of cracks and dislocations, thus improving the crystal quality of the layer and reducing the defects and dislocations [118]. All together LED3 would improve the hole concentration in the *p*-region for the injection into the active region. Moreover, the effective valence band

barrier height (φ_h) is reduced in the case of LED3 to 340 meV as compared to others, where φ_h in LED1 and LED2 is 390 meV and 376 meV, respectively. This supports the enhanced hole transportation in the proposed structure, LED3.

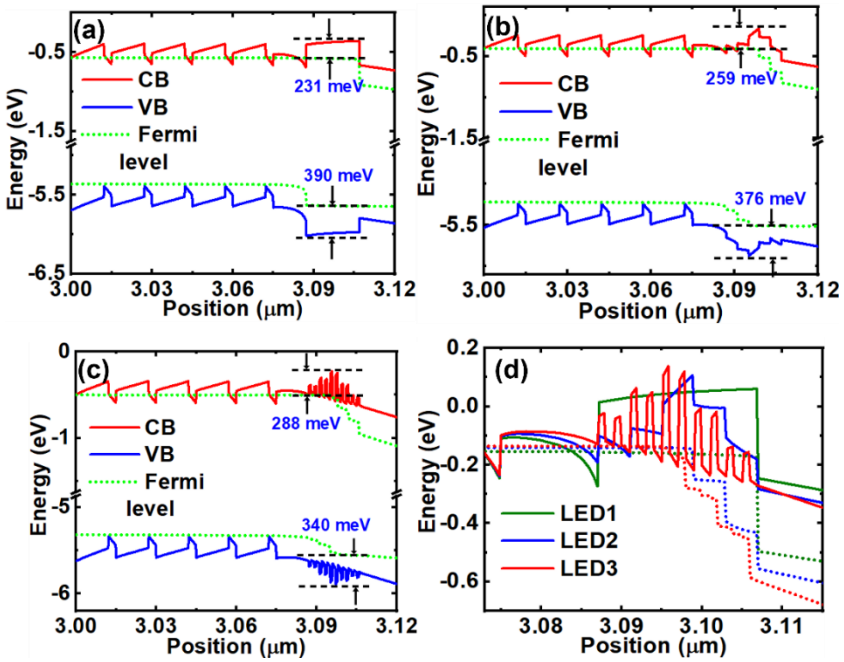

Figure 3.3 Energy band diagrams of (a) LED1, (b) LED2, (c) LED3, (d) conduction band around the EBL region for LED1, LED2 and LED3 at an injection current of 60 mA.

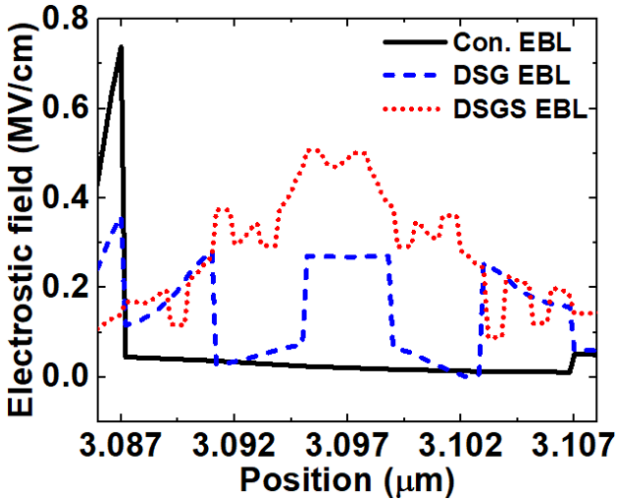

Figure 3.4 Magnitude of electrostatic field profile of Con. EBL (conventional EBL) in LED1, DSG EBL (double-sided step graded EBL) in LED2 and DSGS EBL (double-sided step graded superlattice EBL) in LED3.

Next, the electron concentration, hole concentration, and radiative recombination rate for the three LED structures have been calculated at an injection current of 60 mA. For a better comparison of carrier concentration and radiative recombination rates, horizontal positions of LED1, LED2 and LED3 are slightly shifted. Figure 3.5(a) illustrates the electron concentration profile after the active region, which shows the electron leakage in LED3 is significantly less i.e., ~12 times compared to LED1 and LED2. This is due to higher effective conduction band barrier height (φ_e) in the case of LED3 to reach the *p*-region, which confines the electrons in the active region in a better way. Due to this, non-radiative recombination of leaked electrons with the holes in the *p*-side is reduced and more holes are available for injection into the active region.

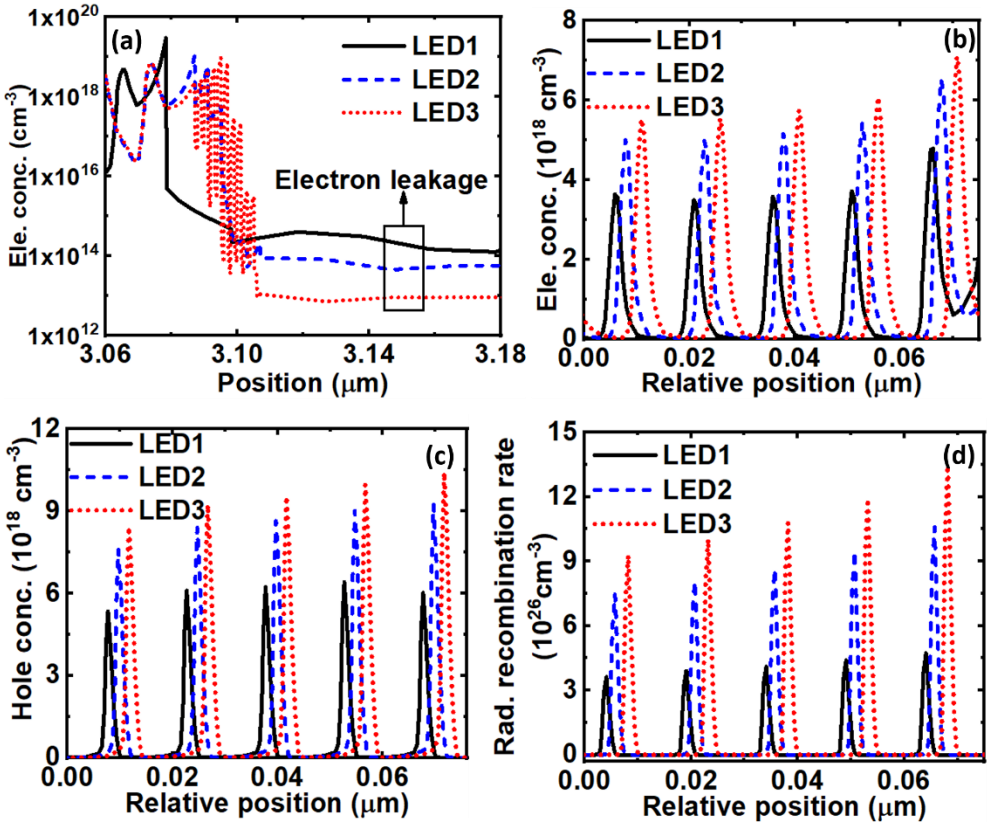

Figure 3.5 (a)-(b) Electron Concentration, (c) hole concentration and (d) radiative recombination of LED1, LED2, and LED3 at an injection current of 60 mA.

Further, the effective valence band barrier height (φ_h) for hole injection is less in LED3 as compared to LED1 and LED2. This improved the electron and hole concentration in the active region for LED2 as compared to LED1 and reached its maximum value in LED3, as shown in Figures 3.5(b) and 3.5(c), respectively. As a result, the radiative recombination rate in the case of LED3 is enhanced as compared to LED1 and LED2 as shown in Figure 3.5(d). The electrostatic field profile of LED1, LED2 and LED3 are shown in Figure 3.6(a) at an injection current of 60 mA. The electrostatic field is directly proportional to the net polarization charge density as shown in Equations (3.1) and (3.2) [119].

$$E_b \approx (l_{EBL}.\Delta P)/(l_{EBL}.\varepsilon_b + l_b.\varepsilon_{EBL}) \tag{2.1}$$

$$\Delta P(z) = \sigma_s^{Pol}/_{z=0} - \rho_B^{Pol}.z \ \ (z < l_b) \tag{2.2}$$

where, E_b is the electrostatic field in the barrier, l_b and l_{EBL} are the thicknesses of the barrier and EBL, respectively and ε_b and ε_{EBL} represent the dielectric constant of the barrier and EBL, respectively. σ_s^{Pol} is polarization induced sheet charge density and ρ_B^{Pol} is polarization induced bulk charge density. ΔP represents the net polarization charge density. The higher value of an electrostatic field in the quantum well region can restrict the overlapping of the electron and hole wave functions, thus can reduce radiative recombination in the active region and subsequently leading to have poor efficiency. Moreover, a stronger electrostatic field at the LQB/EBL interface can pull down the conduction band which can reduce the carrier confinement in the active region. That is why a lower electrostatic field is always desired in the active region. The polarization-induced electric field in the LQB can be reduced by decreasing the EBL thickness (l_{EBL}) or the net polarization-induced charge density (ΔP) as shown in Equation (3.1). The net polarization induced charge density is

determined by the combination of σ_s^{Pol} and ρ_B^{Pol} as shown in Equation (3.2). The σ_s^{Pol} for LED2 and LED3 is found to be lower because of the reduced spontaneous polarization discontinuity at the last barrier/EBL interface and suppressed piezoelectric polarization effect. Moreover, the polarization-induced bulk charge generation can be raised in LED2 and LED3 due to its compositionally graded profile as compared to LED1. Therefore, ΔP for LED2 and LED3 can be reduced due to the smaller value of σ_s^{Pol} and larger value of ρ_B^{Pol} which will reduce the electrostatic field in the barrier for LED2 and LED3. Moreover, in LED3 due to superlattice EBL structure, the thickness of l_{EBL} of the first superlattice layer is less as compared to LED1 where l_{EBL} is 20 nm and LED2 where l_{EBL} is 4 nm due to the first step. This would further reduce the electrostatic field in the barrier/EBL interface for LED3 as can be seen from Figure 3.6(a). Similar studies have been done for the QW region [119, 120]. It can be seen from Figure 3.6(a), an electrostatic field in the QW as well as at the LQB/EBL interface for LED2 is smaller as compared to LED1 and it is the smallest in the case of LED3.

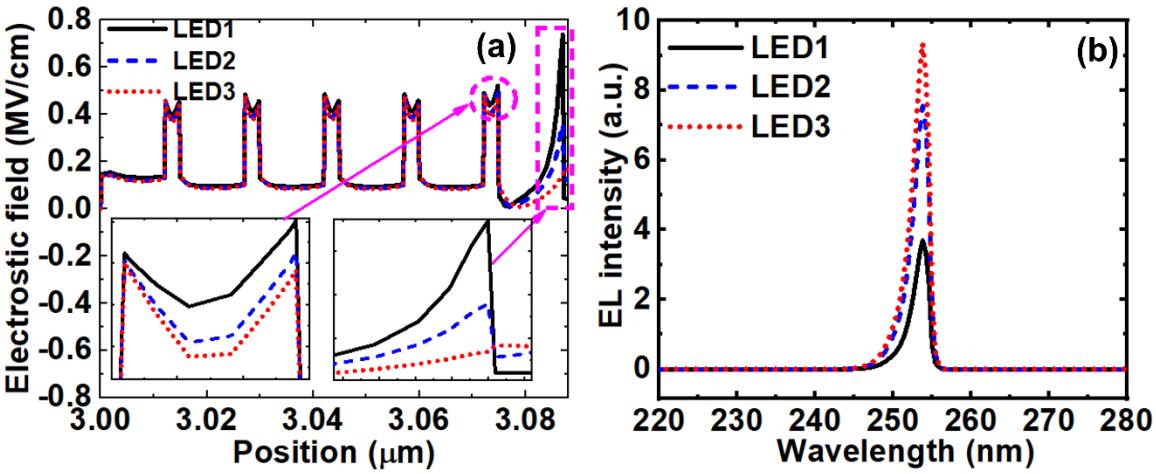

Figure 3.6 (a) Magnitude of electrostatic field in the active region, left inset figure depicts the electrostatic field in the LQW and right inset figure depicts the electrostatic field at the interface of LQB and EBL, (b) emission spectra of LED1, LED2, and LED3 at an injection current of 60 mA.

Figure 3.6(b) demonstrates the emission spectra of all three LED structures. Due to higher radiative recombination in the active region for LED3, as compared to LED1 and LED2, emission intensity is also increased significantly in the case of LED3 at the peak emission wavelength of 254 nm.

3.5 Conclusion

In summary, we have reported deep UV AlGaN LEDs with novel double-sided step graded superlattice (DSGS) EBL instead of conventional EBL operating at ~254 nm wavelength. The enhanced carrier transport in DSGS structure resulted in reduced electron leakage into the *p*-region by ~12 times, improved hole activation and hole injection, enhanced output power and external quantum efficiency. The calculations show that the output power of the DSGS structure is ~3.56 times higher as compared to the conventional structure. Moreover, the efficiency droop at 60 mA injection current in the DSGS LED is found to be ~9.1% that is ~4.5 times lower than the regular LED structure. The reported structure provides a promising approach for achieving high-efficiency UV light emitters for practical applications.

CHAPTER 4

CONTROLLED CARRIER MEAN FREE PATH IN AlGaN DEEP-ULTRAVIOLET LIGHT-EMITTING DIODES

4.1 Introduction

In this chapter, a novel approach is studied to mitigate the electron leakage problem in AlGaN deep UV LEDs using concave QB structures instead of conventional QBs. Extensive research has been performed and different approaches have been introduced to improve the carrier confinement in the active region and control the electron leakage or overflow to the *p*-region. For instance, integration of the *p*-doped higher Al composition EBL after the active region is a common approach to stop the electron overflow [121]. Further, the EBL is re-engineered using a graded layer [122], polarization modulated layers [123], superlattice structure [124], graded superlattice structure [125, 126], and others to efficiently reduce the electron overflow. Alternatively, the electron overflow has been reduced by increasing the effective conduction band barrier heights (CBBH) with the re-design of QBs and promptly utilizing the higher Al composition [127-129]. In this work, another potential approach is introduced to alleviate the electron overflow without increasing the Al composition in the QBs and EBL by utilizing the concave QBs instead of conventional QBs in AlGaN UV LEDs. These specially designed QBs are composed of even lower Al composition than regular ones, which would slow down the hot electrons and reduce the electron mean free path (MFP) before entering the QWs. This leads to improve the electron capturing capability in the MQWs of an active region. In addition, such engineered QBs don't affect the hole transport, in fact, enhance the hole injection into

the active region. Altogether, radiative recombination, IQE, and output power of the concave QB LED could be improved significantly.

4.2 Device Structures

In this study, the reference structure is represented as LED0, which is the conventional QB-based AlGaN deep UV LED structure and reported experimentally by Yan *et al.* [130]. The schematic structure of LED0 is shown in Figure 4.1(a) and consists of a 3 μm *n*-$Al_{0.6}Ga_{0.4}N$ layer (Si doping concentration: 5×10^{18} cm^{-3}), the active region contains five undoped 3-nm $Al_{0.4}Ga_{0.6}N$ QWs sandwiched between six undoped 12-nm $Al_{0.5}Ga_{0.5}N$ QBs, a 20 nm *p*-$Al_{0.65}Ga_{0.35}N$ (Mg doping concentration: 2×10^{19} cm^{-3}) EBL, a 50 nm *p*- $Al_{0.5}Ga_{0.5}N$ (Mg doping concentration: 2×10^{19} cm^{-3}) hole injection layer, and a contact layer of 120 nm *p*-GaN (Mg doping concentration: 1×10^{20} cm^{-3}). Figure 4.1(b) shows the Al composition (%) profile information in the conduction band of LED0.

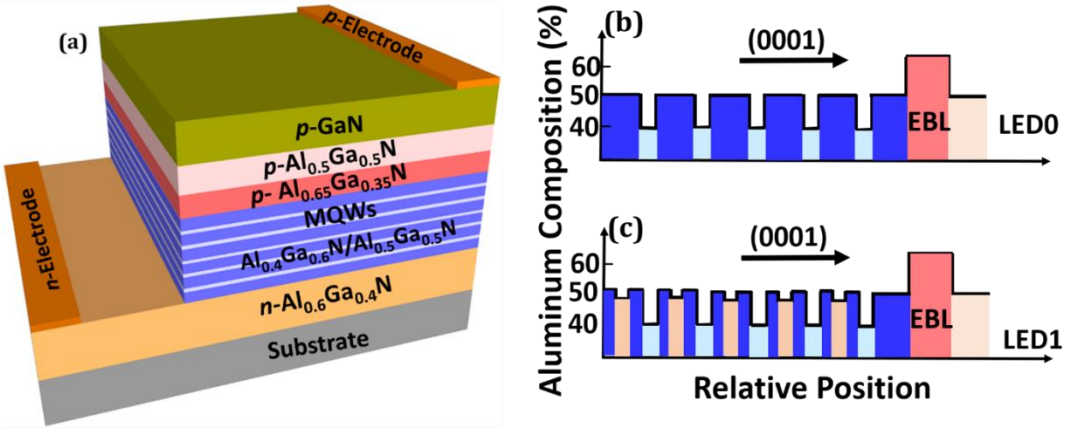

Figure 4.1 (a) Schematic diagram of LED0, Al composition (%) profile in the conduction band of (b) conventional structure, i.e., LED0, and (c) proposed structure, i.e., LED1.

The proposed and concave QB-based structure is denoted by LED1, is the same as LED0 except for QBs. The proposed concave QBs are composed of 4 nm $Al_{0.5}Ga_{0.5}N$/4 nm $Al_{0.47}Ga_{0.53}N$/4 nm $Al_{0.5}Ga_{0.5}N$ layers along the growth direction. This can be seen in Figure 4.1(c). The mesa area of both LEDs is 400 × 400 μm^2.

4.3 Device Parameters

The two LED structures i.e., LED0 and LED1 are modeled and their performance is carefully investigated. In this investigation, the energy bandgap of GaN and AlN is estimated using Equation (4.1) [131].

$$E_g(T) = E_g(0) - \frac{aT^2}{b+T} \tag{3.1}$$

In Equation (4.1), *a* and *b* are material constants, and the corresponding values are 0.909 meV/K, 830 K for GaN; 1.799 meV/K, 1462 K for AlN [131]. E_g (0) and E_g(T) are the energy bandgap at temperatures 0 and T K, respectively. The values of E_g(0) for GaN and AlN are 3.507 eV and 6.23 eV, respectively [131]. The energy bandgap of $Al_xGa_{1-x}N$ is determined using Equation (4.2), as given below.

$$E = x \cdot E^{AlN} + (1-x) \cdot E^{GaN} - b \cdot x \cdot (1-x) \tag{3.2}$$

In Equation (4.2), *b* represents the bowing parameter, the value of *b* is assumed as 0.94 [109]. We have considered the Mg activation energy in our model and set it as 170 meV and 510 meV for *p*-GaN and *p*-AlN, respectively. The Mg activation energy is estimated for *p*-$Al_xGa_{(1-x)}N$ alloy using linear approximation where $0<x<1$ [112]. The auger recombination coefficient, radiative recombination coefficient, SRH recombination coefficient, and light extraction efficiency values as 2.88×10^{-30} cm^6/s, 2.13×10^{-11} cm^3/s, 6.67×10^7 /s, and 15%, respectively [111]. The net polarization effect due to piezoelectric

and spontaneous polarization is considered to be 50% in the model. The band offset ratio for the III-nitride material hetero-junctions is taken as 0.67/0.33 [125]. The energy-band diagrams of two LED structures are calculated using the 6×6 *k.p* model [110].

4.4 Theoretical Model

For a better insight into the controlled electron MFP in LED1, the theoretical model is presented with the help of different electron transport schemes. The schematic energy band diagrams of LED0 and LED1 are shown in Figure 4.2.

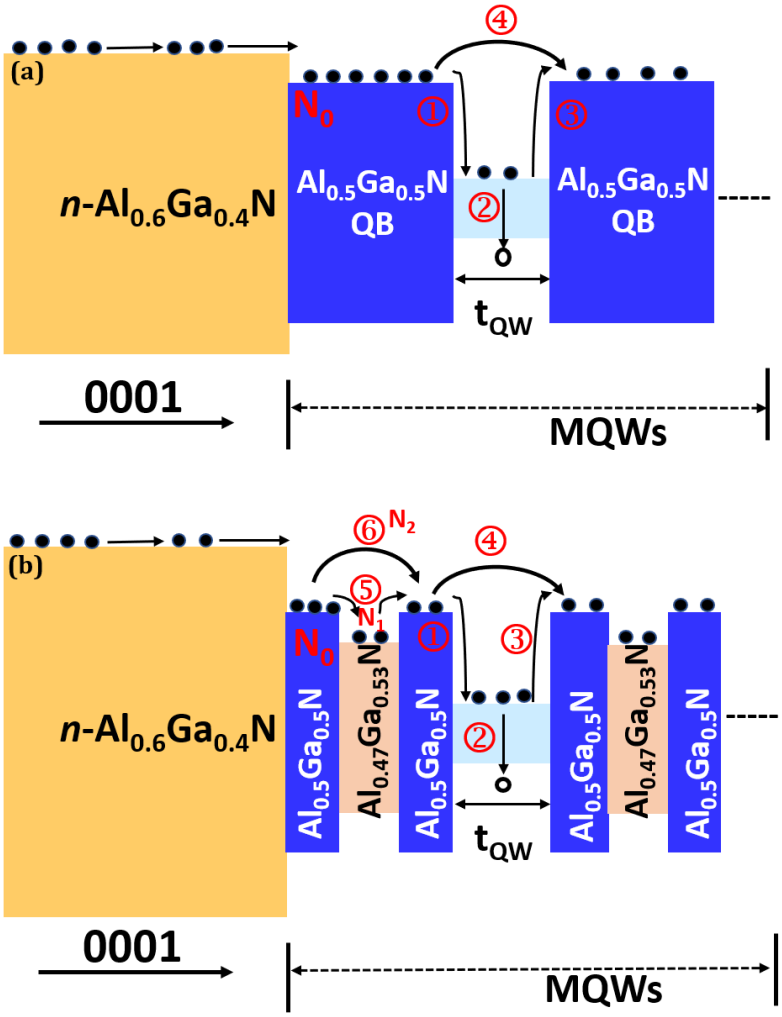

Figure 4.2 Schematic of energy band diagram of (a) LED0 and (b) LED1.

N_0 is assumed to be the number of electrons injected into QB in both LEDs. From Figure 4.2(a), electrons experience four different transport processes in the active region of LED0. The electron tunneling through barriers is not employed in this model for simplicity. A part of the electrons (N_{c0}) from N_0 are scattered and captured into the QW is denoted as a process ① and some of them are recombined radiatively/non-radiatively with holes, as illustrated in process ②. However, some of them can escape from the QW, as presented in process ③. Also, as shown in process ④, the electrons with longer electron MFP can directly jump over QW without being captured in it. It is clearly understood that processes ③ and ④ lead to electron leakage from the active region, which is undesired and needs to be mitigated. The captured electrons (N_{c0}) in QW of LED0 can be expressed as [82],

$$N_{C0} = N_0 \times [1 - \exp(-t_{QW} / l_{MFP0})] \tag{3.3}$$

where t_{QW} is the QW thickness, and l_{MFP0} is the electron MFP in LED0. As depicted in Figure 4.2(b), the electron transport processes in the proposed structure, LED1, are the same as LED0 except for processes ⑤ and ⑥ due to the concave QBs. Here, a part of electrons (N_1) from N_0 are trapped by the $Al_{0.47}Ga_{0.53}N$ layer with the interaction of LO phonons before being captured in QWs. The interaction of phonons with electrons usually creates perturbation in the motion of electrons by scattering them from one state to another state, which results in a reduction of carrier mobility and an increase in resistivity, and ultimately cools down the hot electrons [132]. Thereby, the thermal velocity of the electrons reduces. The reduction in the thermal velocity, v_{th1} due to electron-phonon interaction during process ⑤ is incorporated in Eq uation(4.7). At the same time, the rest of the electrons (N_2=N_0-N_1) can fly over the $Al_{0.47}Ga_{0.53}N$ layer. Overall, captured electrons (N_{c1}) in QW of LED1 can be estimated as

$$N_{C1} = N_1 \times [1 - \exp(-t_{QW} / l_{MFP1})] + N_2 \times [1 - \exp(-t_{QW} / l_{MFP2})] \tag{3.4}$$

where l_{MFP1} is the MFP of electrons that are undergone the process ⑤, and the electrons that participated in process ⑥ have MFP of l_{MFP2}. From Equations (4.3) and (4.4), one of the possible ways to improve the captured electron concentration in QWs is to reduce the electron MFP. Next, the calculation of electron MFP in both LEDs was done. The electron MFP (l_{MFP}) can be expressed as a function of thermal velocity (v_{th}) and the scattering time (τ_{sc})

$$l_{MFP} = v_{th} \times \tau_{sc} \tag{3.5}$$

$$v_{th0} = \sqrt{2 \times (E_0 + W_0)/m_e} \tag{3.6}$$

$$\begin{aligned} v_{th1} &= \sqrt{2 \times (E_1 + \Delta E + W_1 - \hbar\omega - \Delta E)/m_e} \\ &= \sqrt{2 \times (E_1 + W_1 - \hbar\omega)/m_e} \end{aligned} \tag{3.7}$$

$$v_{th2} = \sqrt{2 \times (E_1 + W_1)/m_e} \tag{3.8}$$

where E_0 = 83.11 meV and E_1 = 83.92 meV are additional kinetic energies (K.E.) in the previous layer of QB_2 with respect to its conduction band of LED0 and LED1. The W_0 = 88.78 meV and W_1 = 70.55 meV are work done to the electrons by the generated local electric field in QB_2 of LED0 and LED1, respectively. The work done values are estimated using electric field ($E(y)$, along the growth direction "y") of QB_2 from Figure 4.3(c) and can be written as

$$W = \int_0^{t_{QB}} q \times E(y) dy \tag{3.9}$$

In Equation (4.9), t_{QW} is the QB thickness. The v_{th0} represents the electron thermal velocity in LED0, while v_{th1} and v_{th2} are electron thermal velocities with undergone processes ⑤ and ⑥ in LED1. The $+\Delta E$ in Equation (4.7) represents the K.E. received by the electrons when crossing the band-offset between n-$Al_{0.5}Ga_{0.5}N$ and n-$Al_{0.47}Ga_{0.53}N$ layers. $-\Delta E$ is the energy lost by electrons while jumping from the n-$Al_{0.47}Ga_{0.53}N$ layer during process ⑤ in LED1. Also, $\hbar\omega \approx 102$ meV [133] is the energy lost due to LO phonon

emission during the scattering in process ⑤ of LED1. Here, the effective mass of the electrons is considered as m_e. Therefore, the calculated thermal velocity values of v_{th0}, v_{th1}, and v_{th2} are 4.82×10^7 cm/s, 2.66×10^7 cm/s, and 4.57×10^7 cm/s. It is clearly observed that electrons who undergo process ⑤ due to the proposed concave QB exhibit the lowest thermal velocity i.e., $v_{th1} < v_{th2} < v_{th0}$. Subsequently, the electron MFP at τ_{sc} = 0.0045 ps [134] for above all cases would be 2.169 nm, 1.197 nm, and 2.056 nm, respectively. As expected, electrons that have undergone process ⑤ also demonstrate the lowest MFP. In other words, process ⑤ is supporting to cool down hot electrons in the QBs before being captured in QWs. Also, the reduced electrostatic field in MQWs of LED1 due to concaved QBs reinforces the overlap of electron-hole wavefunctions spatially that supports the radiative recombination mechanism [135], as shown in Figure 4.3. Overall, the concave QB structure i.e., LED1 reports a lower electron MFP that definitely enhances the electron capture capacity in the QWs and is expected to mitigate the electron leakage from the active region eminently.

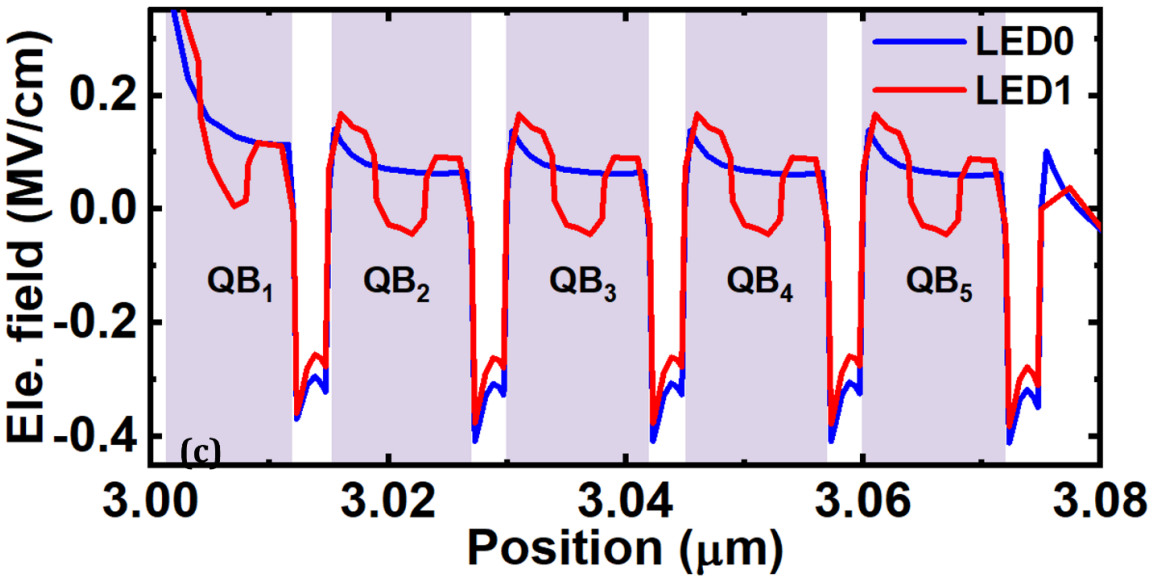

Figure 4.3 Estimated electrostatic field in MQWs of LED0 and LED1.

4.5 Results

To understand the performance and analyze the carrier transport in the AlGaN deep UV LED structures, first, the energy-band (E-B) diagrams of LED0 and LED1 are calculated and presented in Figure 4.4. These E-B diagrams are calculated at 60 mA current injection. As shown in Figure. 4.4, ϕ_{en} is the effective CBBH which is the maximum energy difference between the conduction band and its corresponding quasi-Fermi level for electrons in the QB (n).

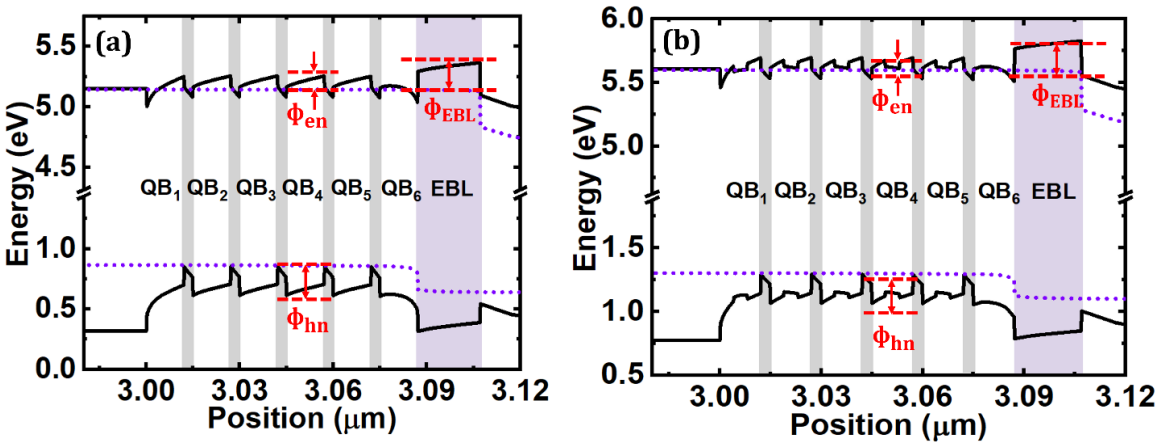

Figure 4.4 Calculated energy-band diagrams of LED0 and LED1 at 60 mA current injection.

Table 4.1 Effective CBBHs of QBs (ϕ_{en}) and EBL (ϕ_{EBL}) for LED0 and LED1

CBBH	LED0	LED1
ϕ_{e1}	107.5 meV	96.1 meV
ϕ_{e2}	114.3 meV	98.8 meV
ϕ_{e3}	113.8 meV	98.1 meV
ϕ_{e4}	112.6 meV	96.8 meV
ϕ_{e5}	110.1 meV	94.6 meV
ϕ_{e6}	31.2 meV	28.5 meV

Table 4.2 Effective VBBHs of QBs (ϕ_{hn}) for LED0 and LED1

VBBH	LED0	LED1
ϕ_{h2}	251.9 meV	237.4 meV
ϕ_{h3}	250.3 meV	236.7 meV
ϕ_{h4}	249.3 meV	235.6 meV
ϕ_{h5}	248.1 meV	234.7 meV

The CBBH values (ϕ_{en}) at the corresponding barrier (n) are assessed from conduction bands and presented in Table 4.1. It is found that the proposed structure, LED1, exhibits relatively lower ϕ_{en} values compared to the conventional structure, LED0. It has been reported that the higher ϕ_{en} values support the electron blocking capability in the active region and prevent severe electron leakage into the *p*-region [127]. However, irrespective of ϕ_{en} values, LED1 with concave QBs demonstrate less electron leakage due to reduced electron MFP in the active region. Moreover, the effective valence band barrier height (VBBH) values are denoted as ϕ_{hn}, which is the maximum energy difference between the quasi-Fermi level for holes and the valence band at the corresponding barrier (n). These values are estimated from valence bands and provided in Table 4.2. The ϕ_{hn} values are low in LED1 compared to LED0 because of the concave QBs, henceforth promoting better hole transportation into AlGaN/AlGaN MQWs region.

The electron concentration in the active region for both LEDs is shown in Figure 4.5(a). As anticipated and concluded in theoretical model, electron concentration in the active region of LED1 is improved due to the reduced electron MFP. This leads to reduce the electron overflow from the active region in the case of LED1 compared to LED0 and found to be lower electron leakage in the *p*-region of LED1, as shown in Figure 4.5(b).

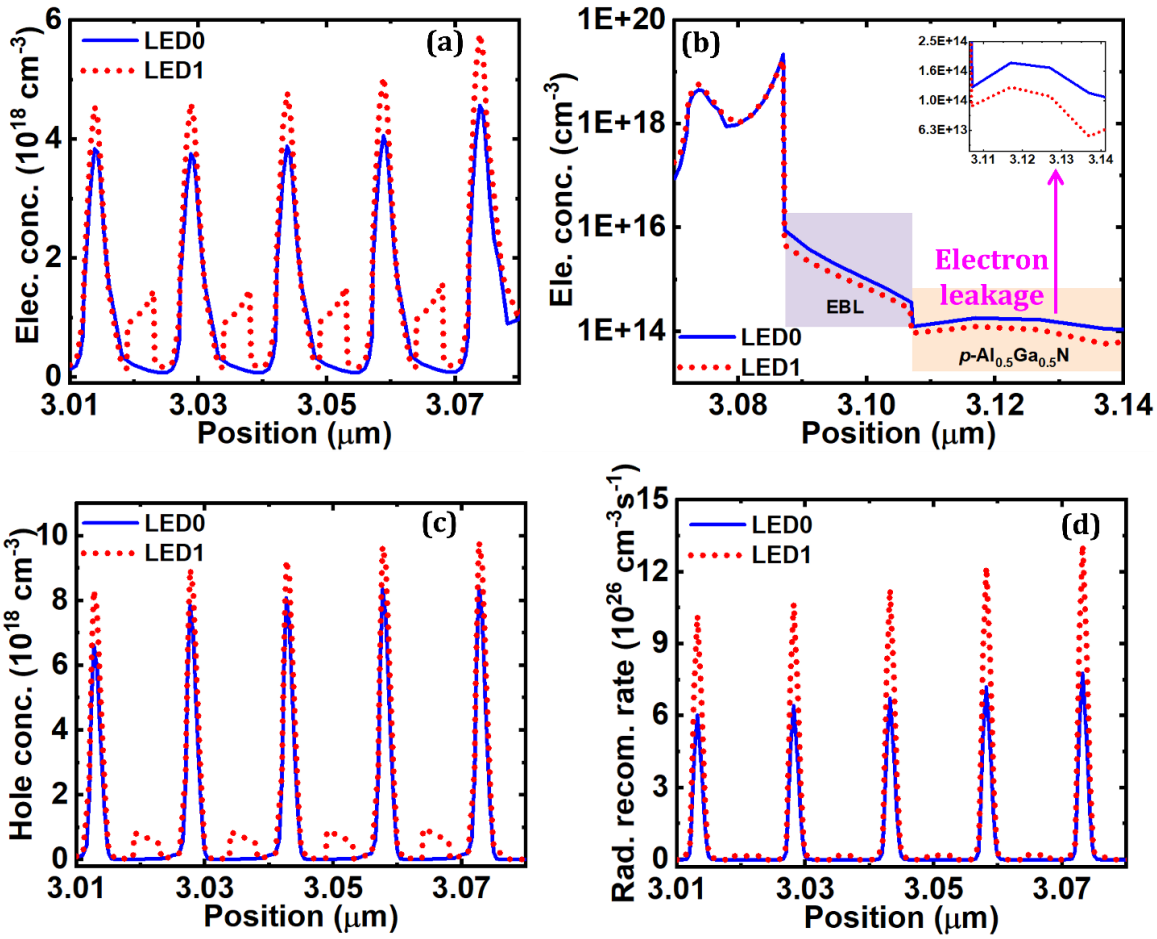

Figure 4.5 Calculated (a) electron concentration, (b) electron leakage, (c) hole concentration, and (d) radiative recombination rate in MQWs of LED0 and LED1.

Such reduced electron leakage also avoids the unwanted non-radiative recombination of leaked electrons with incoming holes in the *p*-region. Further, it helps for the efficient hole injection into the multi QWs. In addition, the reduced effective VBBHs in LED1 support better hole transportation among the QWs. Overall, hole concentration in the active region of LED1 is increased, as seen from Figure 4.5(c). The integrated hole density in the active region for LED0 and LED1 is calculated to be 7.2 $\times 10^{12}$ cm^{-2} and 9.25 $\times 10^{12}$ cm^{-2}, respectively. Subsequently, radiative recombination is also significantly

improved due to the higher carrier concentration in the MQWs of LED1 compared to LED0. This is provided in Figure 4.5(d).

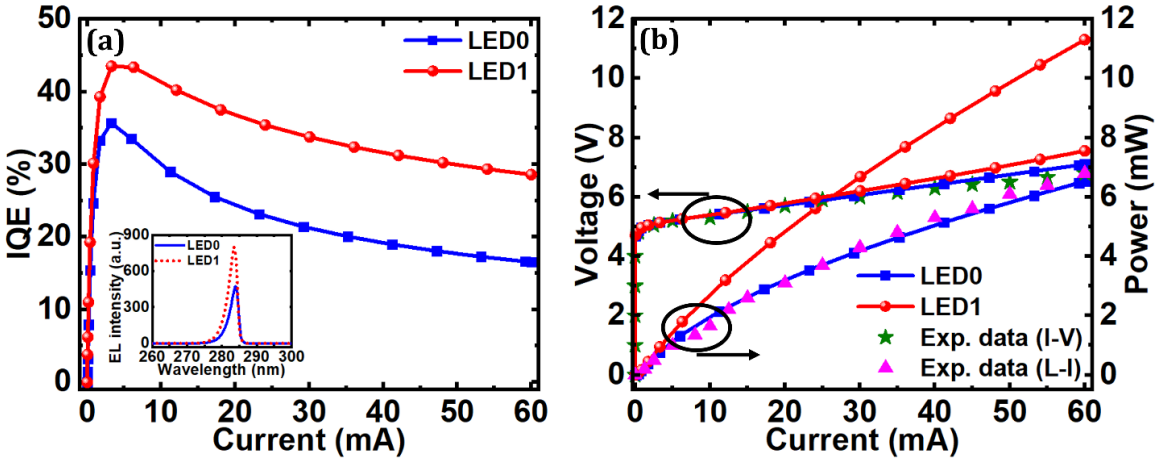

Figure 4.6 Calculated (a) IQE (inset figure: EL intensity), and (b) L-I and I-V characteristics of LED0 and LED1 as a function of injection current.

Next, the IQE of both the LEDs is calculated and provided in Figure 4.6(a). Due to the effective concave QB structure, LED1 exhibits enhanced electrical injection efficiency with reduced electron overflow and increased carrier distribution throughout the device active region. That significantly improved the radiative recombination in LED1, and reduced the electron overflow, due to which LED1 exhibits a maximum IQE of ~39%, while it is ~35% in the case of LED0. Importantly, the IQE of LED1 is improved by ~40.2% compared to LED0 at 60 mA current injection and the efficiency droop is reduced by ~23.3% in LED1 during 0-60 mA operation. Again, due to improved radiative recombination, the EL intensity of LED1 is higher than LED0 at the emission wavelength of ~284 nm, as shown in the inset of Figure 4.6(a). Figure 4.6(b) demonstrates the power vs. current (L-I) characteristics and voltage vs. current (I-V) characteristics of LED0 and LED1. The green stars and triangles are L-I and I-V characteristics of our reference structure that were experimentally reported by Yan *et al.* [130]. As depicted in Figure

4.6(b), the simulated L-I-V characteristics of LED0 are closely matching with the experimentally reported results, which validates the reliability of the simulation model and parameters. The turn-on voltage for LED1 is nearly the same as that of LED0, with a slightly higher operating bias voltage at 60 mA injection current. However, there is a tremendous improvement in the output power of LED1. The recorded output power of LED1 is 9.16 mW at 60 mA current injection which is boosted by ~40.5% compared to LED0 at the same current injection level.

4.6 Conclusion

In summary, we have systematically designed a unique concave QB-based AlGaN UV LED structure and investigated the performance. It is understood that the concave QB structures are favorable for cooling down the hot electrons before entering into the QWs thus achieving lower electron MFP and velocity, which can be resulted in remarkably reduced electron leakage.

CHAPTER 5

BANDGAP ENGINEERING OF ELECTRON-BLOCKING LAYER FREE AlGaN DEEP-ULTRAVIOLET LIGHT-EMITTING DIODES

5.1 Introduction

In this chapter, the design and performance of the EBL free AlGaN deep UV LEDs are studied by band engineering the QBs. The proposed structure significantly reduces thermal velocity and MFP of electrons in the active region, therefore greatly confines the electrons over there. This leads to reducing the electron leakage into the *p*-region tremendously. Moreover, these optimized QBs reduce the quantum-confined Stark effect in the active region, thereby improving the electron and hole wavefunctions overlap.

5.1.1 Problems with the conventional EBL

To eliminate the electron overflow, a *p*-doped Al-rich EBL has been introduced between the active region and *p*-region [136]. The schematic diagram of UV LED with the integration of EBL is presented in Figure 5.1. Definitely, EBL could suppress the electron leakage problem, but to an extent, not completely. At the same time, EBL supports the formation of positive polarization sheet charges at the interface of the LQB and EBL [129], which leads to the creation of a hole depletion region, illustrated in Figure 5.1. This reduces the hole injection efficiency into the active region. Another challenge is growing highly efficient EBLs. As the EBL is an Al-rich composition of AlGaN layers, Mg doping efficiency gets affected because of high acceptor activation energy, compensation by nitrogen vacancies, increased hole scattering, and limited acceptor solubility [112].

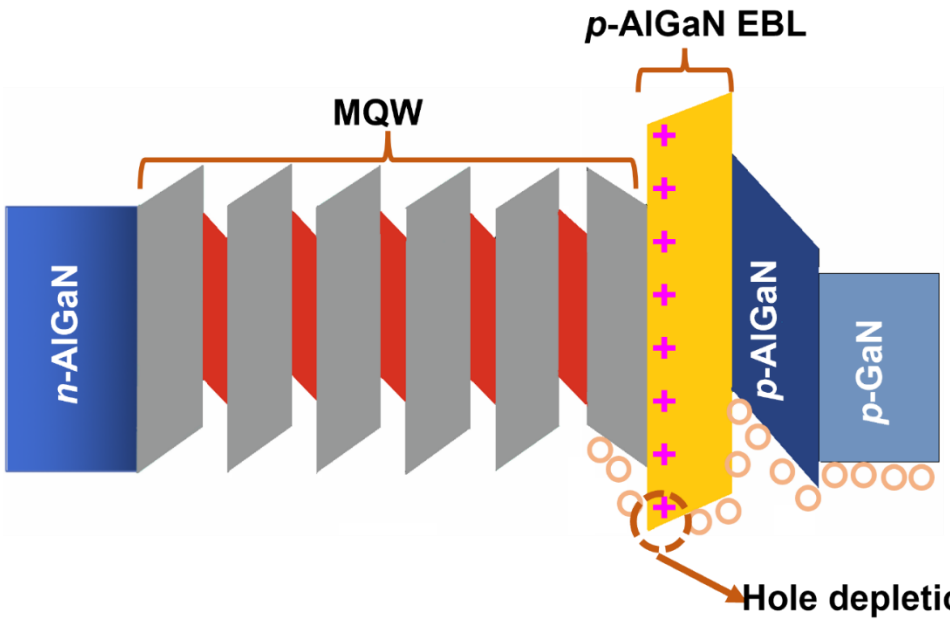

Figure 5.1 Schematic energy-band diagram of AlGaN UV LED with the conventional EBL.

5.1.2 Alternative to conventional EBL structure

To address the problems due to the integration of conventional EBL, QW or EBL is re-engineered using different approaches [125, 126, 137-139]. This would partially reduce the challenges generated by the integration of the EBL, but it is always desired to improve the LED efficiency by eliminating the EBL layer. In this regard, different EBL-free LED designs have been studied for III-nitride semiconductor LEDs. For instance, linear graded QB-based EBL-free AlGaN UV LEDs reported almost similar optical performance compared to conventional EBL LEDs [140], strip-in-a-barrier AlGaN UV LEDs without EBL have shown remarkably high performance compared to regular EBL LEDs [78]. Band engineered AlInN UV LEDs [141], lattice-matched InGaN/AlInN/InGaN QB visible LEDs are also reported better performance without EBL [77]. Superior performance was observed from the integration of coupled QWs before and after the active region of

InGaN/GaN nanowire LED for white light emission instead of AlGaN EBL-based devices [142] are some of the reported studies. However, to date, a study on high-performance EBL free AlGaN deep UV LEDs is limited. Therefore, it is necessary to further engineer the device structures to achieve high-performance without using EBL that obviates the EBL-related problem.

5.1.3 Proposed EBL free device design approach

EBL-free AlGaN UV-LEDs with the utilization of the graded staircase QBs (GSQBs) in the active region are designed in this study. It is expected that the incorporation of GSQBs reduces kinetic energy and the velocity of the electrons entering the active region. As a result, the electron MFP can reduce and improve the electron confinement in the active region. Another advantage of the proposed structure is having the efficient electron-blocking capability due to gradually increased effective CBBHs of each QB in the active region along the growth direction that effectively blocks the electron overflow into the *p*-region without using EBL. Therefore, the non-radiative recombination in the *p*-region could be dramatically reduced. Since the proposed structure does not require an EBL, it eliminates the formation of positive polarization sheet charges at the heterointerface of the last QB and EBL. Moreover, such specially designed QBs reduce the quantum-confined Stark effect in the active region, thereby improving the electron and hole wavefunction overlap. Due to having all the above-mentioned advantages, Carrier transport, radiative recombination, IQE and output power of the proposed structure are notably improved compared to the conventional EBL-based structure.

5.2 Device Structure

Firstly, the device model was validated by simulating and verifying the EBL-based AlGaN deep UV LED reference structure [130] which was grown on a *c*-plane AlN template with ~284 nm wavelength emission. The reference structure is denoted by LED 1, consists of a 3 µm thick *n*-$Al_{0.6}Ga_{0.4}N$ layer (Si doping concentration: 5×10^{18} cm^{-3}), succeeded by an active region of five intrinsic 3 nm $Al_{0.4}Ga_{0.6}N$ QWs sandwiched between six intrinsic 12 nm $Al_{0.5}Ga_{0.5}N$ QBs, followed by a 20 nm *p*-$Al_{0.65}Ga_{0.35}N$ EBL (Mg doping concentration: 2×10^{19} cm^{-3}), then capped by a 50 nm *p*-$Al_{0.5}Ga_{0.5}N$ hole injection layer (Mg doping concentration: 2×10^{19} cm^{-3}), and finally a 120 nm *p*-GaN contact layer (Mg doping concentration: 1×10^{20} cm^{-3}). The schematic diagram of LED 1 is presented in Figure 5.2(a) and the Al composition (%) profile related to the conduction band energy diagram of LED 1 is shown in Figure 5.2(b). The mesa area of the deep UV LED chip is 400 × 400 μm^2. As illustrated in Figure 5.2(c), LED 2 has the same structure as LED 1 except the QBs, where the Al composition of the QBs is gradually increasing from QB_2 to QB_6 as

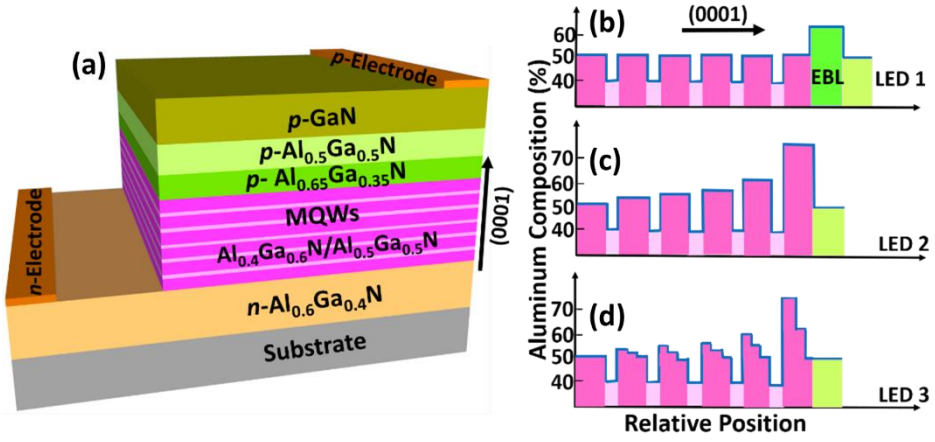

Figure 5.2 (a) Schematic diagram of LED 1, Al composition (%) profile of conduction band in (b) LED 1, (c) LED 2, and (d) LED 3.

0.51, 0.54, 0.57, 0.60, and 0.75, respectively. The proposed structure referred to as LED 3 is identical to LED 2 with the replacement of GSQBs instead of uniform Al composition QBs. As depicted in Figure 5.2(d), 12 nm thick each QB consists of $Al_xGa_{(1-x)}N$ (4 nm)/$Al_{(x+0.5)/2}Ga_{1-(x+0.5)/2}N$ (4 nm)/$Al_{0.5}Ga_{0.5}N$ (4 nm) step layers. The Al composition (x) in the last five QBs is 0.51, 0.54, 0.57, 0.60, and 0.75, respectively. The x values are chosen by carefully optimizing the structure, similar to our previous study [142].

5.3 Device Parameters

All the LED structures are designed and simulated using the APSYS tool. In this simulation model, the energy bandgap of GaN and AlN are estimated using the Varshni formula i.e., Equation (5.1) [131]

$$E_g(T) = E_g(0) - \frac{aT^2}{b+T} \tag{4.1}$$

In Equation (5.1), Eg(T) and Eg(0) are the energy bandgap at temperatures T and 0 K, respectively. a and b are material constants. The values of a, b, and Eg (0) for GaN are 0.909 meV/K, 830 K, and 3.507 eV [108]. The corresponding values for AlN are 1.799 meV/K, 1462 K, and 6.23 eV, respectively [108]. The bowing parameter for the energy bandgap calculation of AlxGa(1-x)N is considered as 0.94 eV. We have assumed the band offset ratio for AlGaN as 0.67/0.33 [109]. The carrier mobility is estimated using the Cauchy-Thomas approximation [143] and the energy band diagrams of LED structures are calculated by using the 6×6 k.p model [110]. Additionally, the Mg activation energy of AlxGa(1-x)N alloy for 0<x<1 is set to scale linearly from 170 meV to 510 meV [112]. The SRH recombination life-time, radiative recombination coefficient, Auger recombination coefficient, and light extraction efficiency are set as 15 ns, 2.13 × 10-11 cm^3/s, 2.88 × 10-

30 cm^6/s, and 15%, respectively [111]. Also, the built-in polarization due to spontaneous and piezoelectric polarization is estimated [115] and taken as 50% of the theoretical value in the model. All simulations are performed at room temperature and other band parameters can be found elsewhere [144].

5.4 Theoretical Model

As shown in Figure 5.3, the theoretical model is developed to understand the transportation of electrons in LED 1 and LED 3. N_0 is the total number of injected electrons into the *n*-$Al_{0.6}Ga_{0.4}N$ region of both LEDs. For the simplicity of the model, electron loss through non-radiative recombination in the *n*-$Al_{0.6}Ga_{0.4}N$ region is neglected. The captured electrons in the quantum well ($N_{capture}$) can be correlated with the electron MFP (l_{MFP}) as expressed in Equation (5.2) [82].

$$N_{capture} = N_0 \times [1 - e^{\frac{-t_{QW}}{l_{MFP}}}] \tag{4.2}$$

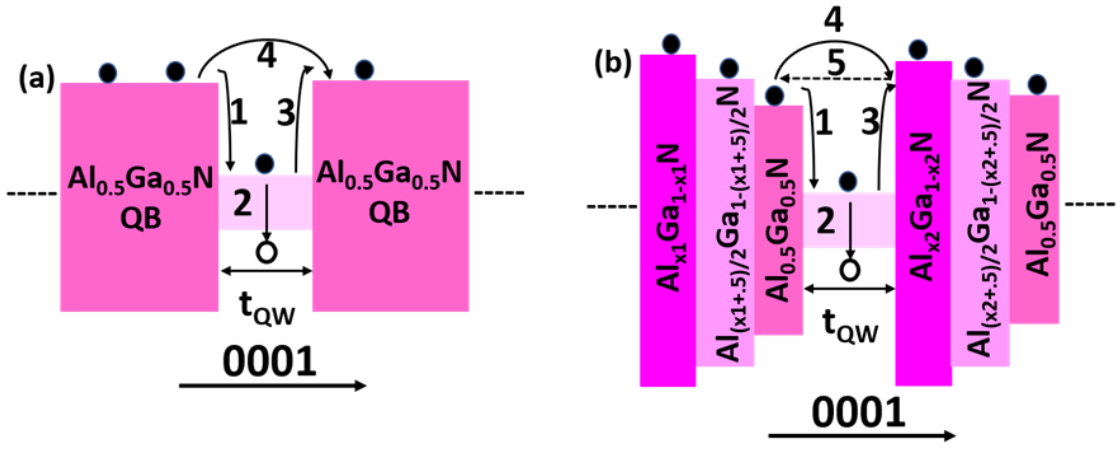

Figure 5.3 Schematic representation of carrier transport in (a) LED 1, and (b) LED 3.

In Equation (5.2), t_{QW} is the quantum well thickness. Illustrated in Figures. 3(a) and 3(b), process 1 represents the incoming electrons (N_0) that are scattered and fall into the quantum wells. Some of those fallen electrons can recombine with the holes radiatively or non-radiatively as denoted by process 2 while remaining electrons escape from the QWs as illustrated by process 3. In addition, some electrons with longer l_{MFP} travel to a remote position without being captured by the QWs as indicated by process 4. To increase $N_{capture}$, the l_{MFP} of these electrons needs to be reduced so that the electron concentration in the QWs would be increased that would favor the higher radiative recombination rate in the active region. At the same time, l_{MFP} depends on thermal velocity (v_{th}) and the scattering time (τ_{sc}) as shown in Equation (5.3). For LED 1, v_{th} can be further expressed as illustrated in Equation (5.4) [82].

$$l_{MFP} = \upsilon_{th} \times \tau_{sc} \tag{4.3}$$

$$\begin{aligned} \upsilon_{th} &= \sqrt{2 \times \frac{[E + \Delta E_c + qV_1 - \Delta E_c]}{m_e}} \\ &= \sqrt{2 \times \frac{[E + qV_1]}{m_e}} \end{aligned} \tag{4.4}$$

In Equation (5.4), E is the excess kinetic energy in the *n*-$Al_{0.6}Ga_{0.4}N$ layer, qV_1 is the work done to the electrons by the induced polarization electric field in QBs of LED 1, and m_e is the effective mass of electrons. $+\Delta E_c$ denotes the conduction band offset between QB_n and QW_n, while $-\Delta E_c$ represents the conduction band offset between QW_n and QB_{n+1}. On the other hand, the GSQB structure in LED3 forms discontinuity in the conduction band of QB layers due to which the probability of the electrons to be scattered increases. Therefore, electrons would be thermalized more efficiently by interacting with LO

phonons, thereby reducing the v_{th} and l_{MFP}, as a result, electron confinement in the active region increases [83]. Hence, the v_{th} in LED3 can be expressed as follows,

$$\upsilon_{th} = \sqrt{2 \times \frac{[E + \Delta E_{c1} + qV_2 - \Delta E_{c2} - \hbar\omega_{LO}]}{m_e}} \tag{4.5}$$

$$\hbar\omega_{LO} = \hbar\omega_{LO(step1)} + \hbar\omega_{LO(step2)} + \hbar\omega_{LO(step3)} \tag{4.6}$$

where $+\Delta E_{c1}$ represents the conduction band offset between QB_n and QW_n whereas $-\Delta E_{c2}$ is the conduction band offset between QW_n and QB_{n+1}. As the QB heights are varying in LED 3 along the growth direction, therefore, ΔE_{c1}- ΔE_{c2} cannot be eliminated. qV_2 is the work done to the electrons by the induced polarization electric field in GSQBs of LED 3. The $-\hbar\omega_{LO}$ denotes the total energy loss by phonon emissions due to each step layer in GSQBs. The values of qV due to each QB in LED1 and LED3 are listed in Table 5.1. Further, the values of $\hbar\omega_{LO}$ in each step of GSQBs for LED 3 are calculated [133] and presented in Figure 5.4.

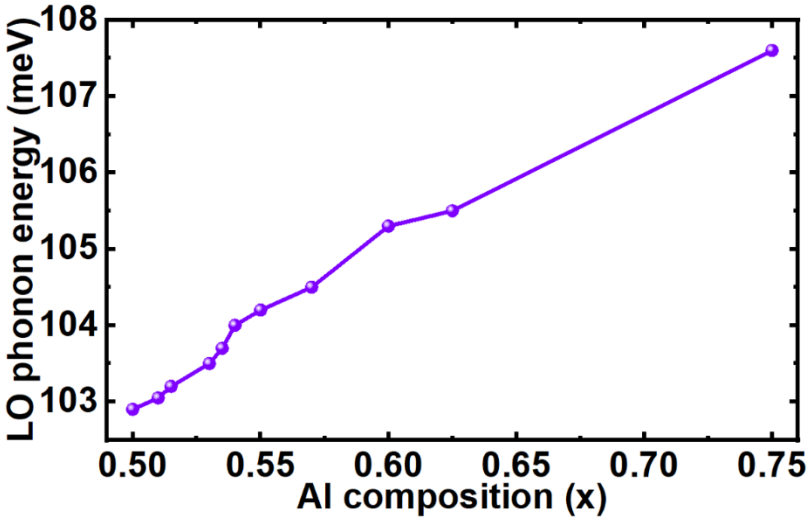

Figure 5.4 Calculated LO phonon energy in $Al_xGa_{1-x}N$ layer.

Table 5.1 Comparison of *qV1* and *qV2* Values of LED 1 and LED 3

	QB2	QB3	QB4	QB5
LED1	88.8 meV	87.2 meV	86.5 meV	85.0 meV
LED3	84.2 meV	100.6 meV	104.4 meV	78 meV

From Equations (5.4) and (5.5), it is understood that ($E+\Delta E_{c1}+qV_2-\Delta E_{c2}-\hbar\omega_{LO}$) < ($E+qV_1$). Consequently, v_{th} of LED3 would be less as compared to LED1. As a result, l_{MFP} would be reduced, which improves the electrons capture ($N_{capture}$) ability of the QWs in LED3. In addition, the electron overflow happening due to process 4 can also be reduced by increasing the barrier height as in the proposed structure shown in Figure 5.3(b). Here, the QB heights before and after the QWs are not at the same level, rather it is progressively increasing along the growth direction due to which some of the electrons from process 3 and 4 would bounce back denoted as process 5, which can also aid to improved electron concentration in the QWs in comparison with LED 1.

5.5 Results

The numerical device model and parameters are optimized in this study by simulating the reference structure i.e., LED 1 and validating the results with experimentally measured data of LED 1 published by Yan et al [130]. The numerically calculated and experimentally reported light-current and current-voltage characteristics of LED 1 are shown in Figure 5.5. It is observed that their results are closely matching with each other. This prevails the reliability of the utilized simulation model.

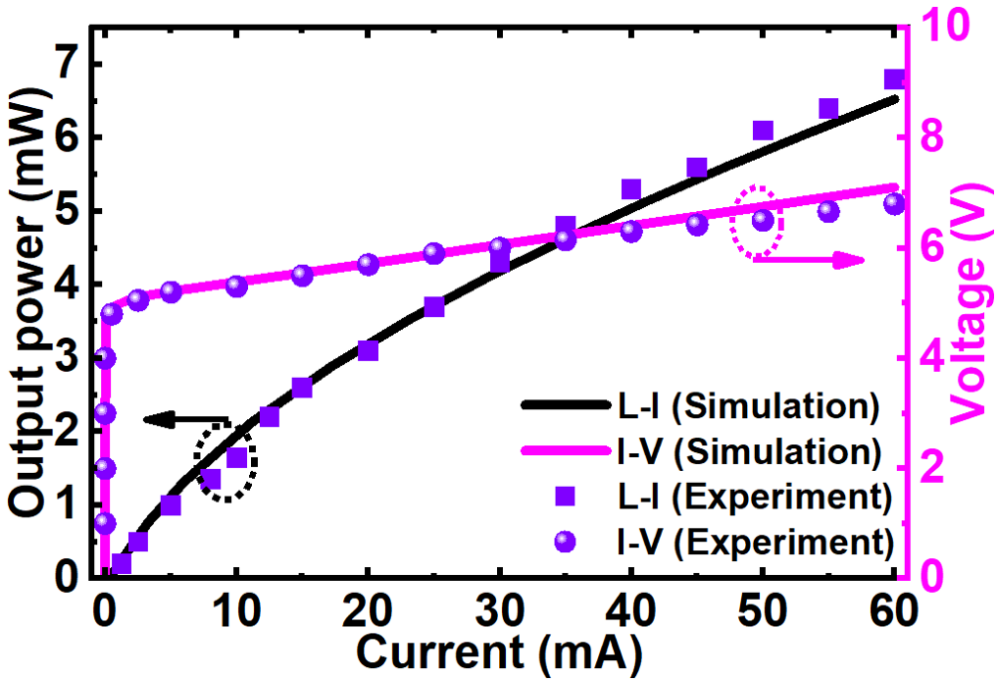

Figure 5.5 Measured and calculated light-current and current-voltage characteristics of LED 1 for model validation [130].

Next, the energy-band diagrams of LED 1, LED 2, and LED 3 are calculated at 60 mA current injection, as shown in Figure 5.6. ϕ_{en} and ϕ_{EBL} are the effective CBBHs at the corresponding barrier (n) and EBL, respectively. In the same way, the effective VBBHs at the corresponding barrier (n) are denoted as ϕ_{hn}. The CBBH values for each barrier are estimated from the energy band diagrams and listed in Table 5.2.

Table 5.2 Effective CBBHs of QBs (ϕ_{en}) and EBL (ϕ_{EBL}) for LED 1, LED 2, and LED 3

	LED 1	LED 2	LED 3
ϕ_{e2}	114.3 meV	167.3 meV	104.42 meV
ϕ_{e3}	113.8 meV	232.6 meV	134.77 meV
ϕ_{e4}	112.6 meV	300.6 meV	191.15 meV
ϕ_{e5}	110.1 meV	330.1 meV	230.22 meV
ϕ_{e6}	31.2 meV	242.2 meV	322.54 meV
ϕ_{EBL}	235 meV	-	-

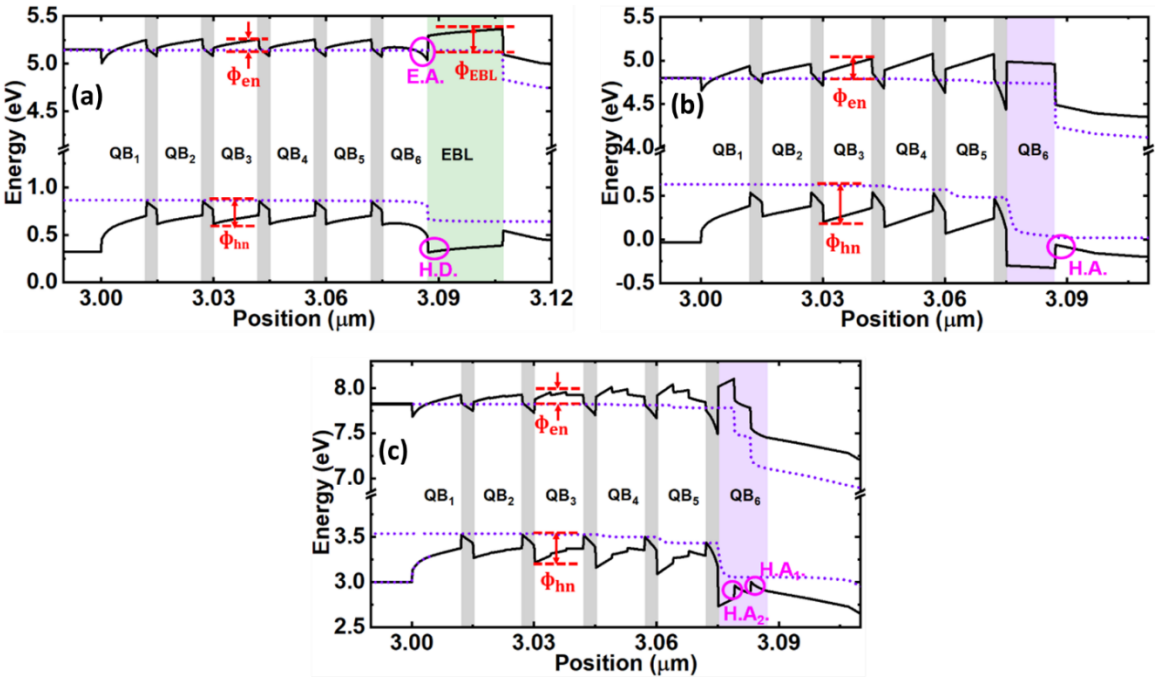

Figure 5.6 Calculated energy-band diagram of (a) LED 1, (b) LED 2, and (c) LED 3 at 60 mA current injection. E.A. represents the electron accumulation region, H.D. is the hole depletion region, and H.A. is the hole accumulation region.

The value of ϕ_{EBL} in LED 1 is 235 meV due to EBL, which is the maximum CBBH to block the electron overflow in LED 1. This value is comparatively low in contrast to LED 2 and LED 3 without EBL. The value of ϕ_{en} is progressively increasing with each QB and effectively blocking the electrons overflow by preventing the electrons from jumping out of the QWs in LED 2 and LED 3. Further, the value of maximum CBBH i.e., ϕ_{e6} in LED 3, is even higher than that of LED 2 from Table 5.2, demonstrating LED 3 is the optimal choice to confine the electrons in the active region. As a result, improved and maximum electron concentration in the active region for LED 3 was observed in comparison with other LEDs and is shown in Figure. 5.7(a). Though LED 2 has boosted electron concentration as compared to LED 1, but it is lower than LED 3. It is also noticed that due to improved electron confinement in the active region, electron leakage into the *p*-region

is significantly reduced in LED 3, as shown in Figure. 5.7(b). Subsequently, this would reduce the non-radiative recombination of the overflowed electrons and incoming holes in the *p*-region thereby, contributing to better hole injection efficiency into the active region. However, LED 2 has even higher electron leakage as compared to LED 1. Due to this, the non-radiative recombination in the *p*-region of LED 2 would increase and reduce the hole injection efficiency into the active region, irrespective of the creation of negative sheet polarization charges at the last QB and *p*-$Al_{0.5}Ga_{0.5}N$ interface.

Further, a sharp bending in the conduction band is formed due to induced positive polarization sheet charges at the heterointerface of the last QB and EBL in LED 1. This area accumulates a large number of electrons i.e., ~ 3.66×10^{16} cm^{-3}, which eventually contributes to non-radiative recombination [145]. In addition, due to this induced positive polarization sheet charges in LED 1, a hole depletion region is formed at the heterointerface of the last QB and EBL, as shown in Figure 5.6(a), which reduces the hole injection efficiency [129]. The formation of the hole depletion region problem is eliminated in LED 2 and LED 3 by removing the EBL. In the case of LED 2, a hole accumulation region is formed at the interface of the last QB and *p*-region, which generally should improve the hole injection efficiency, whereas in LED 3 the hole injection efficiency even should further improve due to the formation of two-hole accumulation regions as shown in Figure. 5.6(c). The boosted hole injection efficiency in LED 3 can be seen in Figure. 5.7(c). This is also because of the reduced electron overflow in LED 3 due to improved electron confinement in the active region. Moreover, the effective VBBHs, ϕ_{hn} due to each QB, are calculated and listed in Table 5.3.

Table 5.3 Effective VBBHs of QBs (ϕ_{hn}) for LED 1, LED 2, and LED 3

	LED 1	LED 2	LED 3
ϕ_{h2}	251.9 meV	367.1 meV	269.16 meV
ϕ_{h3}	250.3 meV	427.1 meV	321.19 meV
ϕ_{h4}	249.3 meV	471.4 meV	368.15 meV
ϕ_{h5}	248.1 meV	502.1 meV	406.93 meV

As ϕ_{hn} increases with the increase in Al composition in the QBs, the values of ϕ_{hn} are found to be high in LED 2 and LED 3 compared to LED 1. This supports the improved hole confinement and increased hole concentration in the active region. However, a very high ϕ_{hn} can also affect the hole transportation in the active region at the same time, which is in the case of LED 2. Moreover, already the hole injection efficiency is poor in LED 2, altogether the hole concentration is very low in LED 2, as shown in Figure 5.7(c). In this regard, LED 3 has a smaller value of ϕ_{hn} as compared to LED 2 due to again GSQB structures. Altogether, due to effective hole injection efficiency along with a comparable height of ϕ_{hn} in the active region, hole concentration in LED 3 is relatively evenly distributed as compared to other LEDs. Overall, the hole concentration in the active region of all three LEDs is $7.2 \times 10^{16}\,cm^{-3}$, $4.8 \times 10^{15}\,cm^{-3}$, and $7.8 \times 10^{16}\,cm^{-3}$, respectively.

Table 5.4 Values of the Electron and Hole Wave Function Spatial Overlap Levels in the Active Region for LED 1 and LED 3

	1^{st} QW (%)	2^{nd} QW (%)	3^{rd} QW (%)	4^{th} QW (%)	5^{th} QW (%)
LED 1	34.36	28.39	26.86	26.03	25.14
LED 3	33.77	34.96	34.94	32.77	29.32

Importantly, the overlap level of electron and hole wave functions in the active region for LED 1 and LED 3 are summarized in Table 5.4. It is seen that even though the hole concentration of LED 3 is close to LED 1, the proposed structure in LED 3 improves the

electron and hole wavefunctions overlap level as compared to LED 1. As a result, the radiative recombination is significantly increased in LED 3, as depicted in Figure 5.7(d).

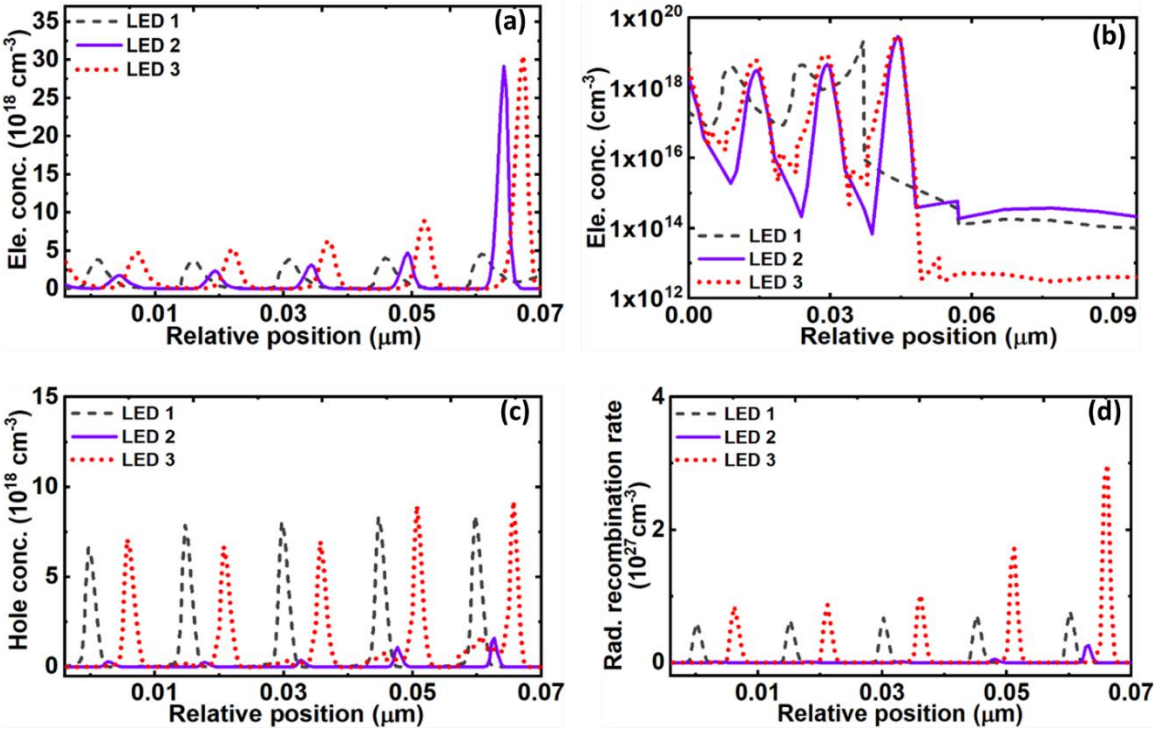

Figure 5.7 Calculated (a) electron concentration, (b) electron leakage, (c) hole concentration, and (d) radiative recombination of LED 1, LED 2, and LED 3.

Table 5.5 Comparison of IQE and Output Power of LED 1, LED 2, and LED 3

	LED 1	LED 2	LED 3
Max. IQE (%)	35.69 at 3.26 mA	29.46 at 0.04 mA	44.34 at 9.66 mA
IQE (%) at 60 mA	16.53	1.56	35.17
IQE (%) droop	53.68	94.7	20.68
Power at 60 mA (mW)	6.52	0.616	13.9

Figures. 5.8(a) and 5.8(b) show the IQE and output power of all three LEDs as a function of current injection. The electroluminescence (EL) spectra of the three LEDs are depicted in Figure 5.8(c). As shown in Figure 5.8(a), LED 3 exhibits the maximum IQE of 44.34%, whereas it is only 35.69% and 29.46% in the case of LED 1 and LED 2,

respectively. In addition, the droop in the IQE during 0 mA-60 mA injection current is remarkably reduced to 20.68% in the proposed structure as compared to 53.68% and 94.7% in LED 1 and LED 2, respectively. This is due to the enhanced carrier transportation and confinement in the active region, thereby reducing electron overflow into the *p*-region because of GSQBs in the proposed structure. As presented in Figure 5.8(b), the output power of LED 3 is 2.13 times higher than LED 1 and 22.56 times higher than LED 2. As shown in Figure 5.8(c), LED 3 depicts higher EL intensity as compared to LED 1 and LED 2 at the emission wavelength of ~284 nm due to improved radiative recombination in the active region. EL intensity of LED 3 is ~2.12 times higher than LED 1 and ~22.24 times higher than LED 2. Different parameters related to IQE and output power of three LED structures are summarized in Table 5.5.

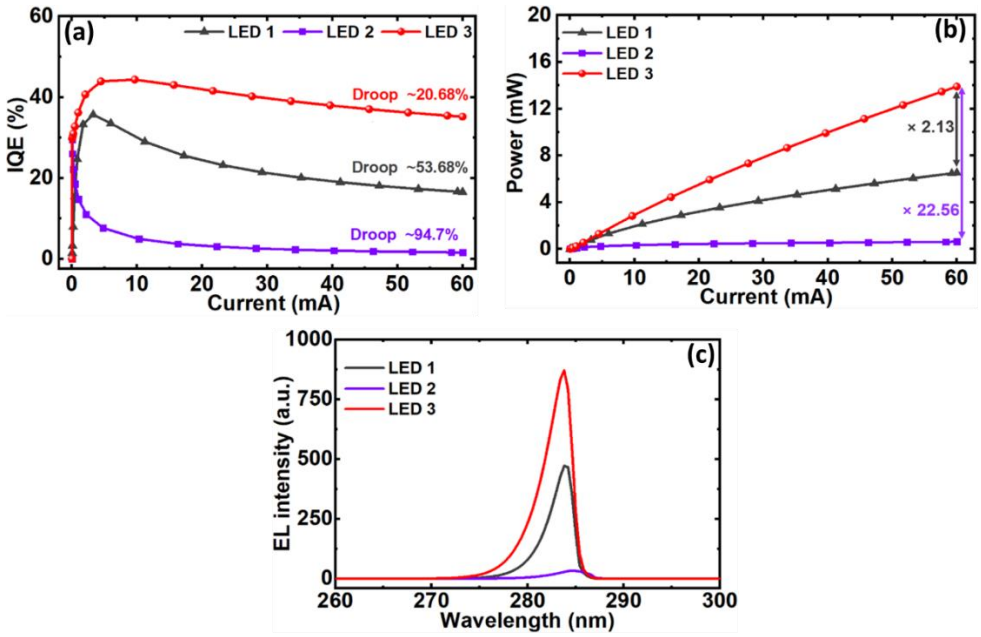

Figure 5.8 Calculated (a) IQE, (b) Output power, and (c) EL intensity of LED 1, LED 2, and LED 3.

5.6 Feasibility of Device Growth

The proposed AlGaN deep UV LEDs using graded staircase barriers can also be realized by experimentation due to a simple device architecture. As different AlGaN based UV LEDs with thinner epilayers than our proposed structure have already been grown by MOCVD [146-148] and MBE [149, 150]. Therefore, it is anticipated that the proposed structure can also be grown by both MBE and MOCVD.

5.7 Conclusion

In conclusion, with the incorporation of GSQB structures, we have successfully designed, demonstrated and investigated the performance of EBL-free AlGaN UV LEDs emitting light at ~284 nm wavelength. The reduced thermal velocity and MFP of electrons improved the electron capture efficiency in the multi QWs, thus electron overflow was suppressed eminently. Also, carefully engineered GSQBs promoted the hole injection by forming negative sheet polarization charges and improved the spatial overlap of the electron-hole wavefunction. Overall, the proposed LED design provides the solution for the electron leakage problem and opens a new path for the realization of high-power UV light emitters.

CHAPTER 6

IMPROVED LIGHT-EXTRACTION EFFICIENCY OF AlInN NANOWIRE DEEP-ULTRAVIOLET LIGHT-EMITTING DIODES

6.1 Introduction

AlGaN semiconductor is extensively studied for UV LED structure due to its direct energy bandgap in the wavelength range of ~200 nm to 365 nm. However, the performance of these UV LEDs is severely limited due to poor EQE. Electron leakage into the *p*-region [151], poor LEE [152] mainly due to the total internal reflection, and absorption of UV light in the *p*-GaN contact layer [153] are a few of the probable reasons for the low EQE. Moreover, as the high Al composition AlGaN quantum wells possess unique optical polarization properties, this results in dominant transverse-magnetic (TM) [E // c-axis] polarized output in the UV regime [62, 154]. As the TM polarized light propagates horizontally, LEE of light emitting from the top surface is severely limited. Due to these problems, the EQE of AlGaN based UV LEDs has been reported to be less than 10% for $\lambda < 300$ nm [63, 155]. Different techniques have been proposed for the improvement of the LEE of deep UV LEDs including patterned sapphire substrates, surface roughening, rolled-up nanotubes, photonic crystal patterns, and flip-chip design, but with very limited success [156-160].

Recently, nanowire-based UV LEDs have been demonstrated, which show significant improvement in the performance compared to the thin-film counterpart due to various reasons [161-165]. Large surface-to-volume ratio in nanowires can relax the lateral stress effectively through the sidewalls, thus the bulk region can be nearly dislocation free

and can be grown directly on different foreign substrates. Apart from this, reduced polarization fields defect densities in the active region and low strain-induced polarization fields are the key reasons leading to the achievement of significantly improved light extraction efficiency. There are studies available on enhancing the LEE of AlGaN nanowire UV emitters [64], emission from the lateral surfaces of nanowire ensembles [166], but the LEE of the TM polarized light emitting from the top surface is still low. Recently, the first AlInN nanowire LEDs emitting light in the UV range of 290 nm – 365 nm is reported. These AlInN nanowire UV LEDs exhibit high IQE and strong TM polarized emission [167]. It is worthwhile to mention that AlInN nanowire-based deep UV LEDs show better performance in terms of IQE and output power as compared to AlGaN based deep UV LEDs due to enhanced carrier transport and reduced electron leakage into the *p*-region [141]. It is highly desired to extract the TM polarized photons from the top surface for practical application. However, research on the polarization-dependent LEE for AlInN based nanowire UV LEDs is very limited to the best of our knowledge. In recent studies, it is shown that using the nanowire photonic crystals for GaN-based nanowires and by controlling the nanowire radius, spacing between the nanowires and morphology of nanowires through selective area epitaxy, luminescence emission intensity and stability can be enhanced significantly [166, 168, 169].

In this study, epitaxial growth using MBE, electrical and optical properties of randomly grown AlInN nanowires on Si (111) substrate is demonstrated. Further, a detailed study of ordered AlInN nanowire array UV LEDs is performed using FDTD simulation, which has been widely used in the analysis of optical properties of III-nitride light-emitters [63, 160, 170]. The light extraction properties of AlInN nanowire LEDs has been studied

at 299 nm for different photonic crystal structure arrangement with hexagon and square lattice of nanowires and compared the results with the random arrangement. The simulation results show that the dominant light emission direction is from the nanowire top surface albeit the light is TM polarized and the photonic crystal structures could improve the LEE much more than random structures by controlling the nanowire radius and spacing between the nanowires. The efficiency is low for random nanowire structures due to the light multipath scattering among adjacent nanowires. This may localize the light inside the nanowires or increase the length of the light escaping path [171].

6.2 Experiment and Results

Figure 6.1(a) illustrates the schematic of an AlInN nanowire LED structure. These nanowires were spontaneously formed on *n*-Si (111) substrates under nitrogen-rich conditions using a Veeco GEN II MBE system equipped with a radio-frequency plasma-assisted nitrogen source. GaN nanowires were *n*-type doped using Si and *p*-type doped using Mg. The growth conditions for GaN include a growth temperature of ~ 770 °C, nitrogen flow rate of 1 sccm, and forward plasma power of ~ 400 W. The device active region consists of a 40 nm undoped $Al_{0.75}In_{0.25}N$ well, sandwiched in between ~100 nm *n*-$Al_{0.78}In_{0.22}N$ and ~100 nm *p*-$Al_{0.78}In_{0.22}N$ barriers. To increase the In incorporation in AlInN segments, the active region was grown at a relatively low temperature of ~ 670 – 700 °C. Moreover, the nitrogen flow rate was kept at 2.5 sccm and plasma power was fixed at 400 W during the epitaxial growth of the active region. Further information regarding the growth condition for the AlInN nanowire LED structure can be found elsewhere [167]. After growing the nanowires using MBE, the LED sample was then fabricated using the standard lithography method and detailed methodology for the fabrication can be found

elsewhere [167]. The device characterization was performed on LED with area size of 500×500 μm^2.

Figure 6.1(b) illustrates a 45 degree-tilted scanning electron microscope (SEM) image of the grown AlInN nanowire LED sample. The nanowires exhibit relatively uniform morphology and size. The wire diameter is in the range of 80 nm to 100 nm. Further, to perform a photoluminescence (PL) experiment, a 266-nm laser (Kimmon Koha) was used as the excitation source. The signal from the nanowire LEDs is spectrally resolved by a high-resolution spectrometer and detected by a photomultiplier tube. As depicted in Figure 6.1(c), the AlInN nanowire LEDs exhibit strong emissions in the UV wavelength range. As presented in Figure 6.1(c), the peak emission at ~299 nm is responsible for the emission from the AlInN quantum well whereas the emission from the AlInN barriers is at ~280 nm and the emission from the GaN segment is recorded at ~368 nm.

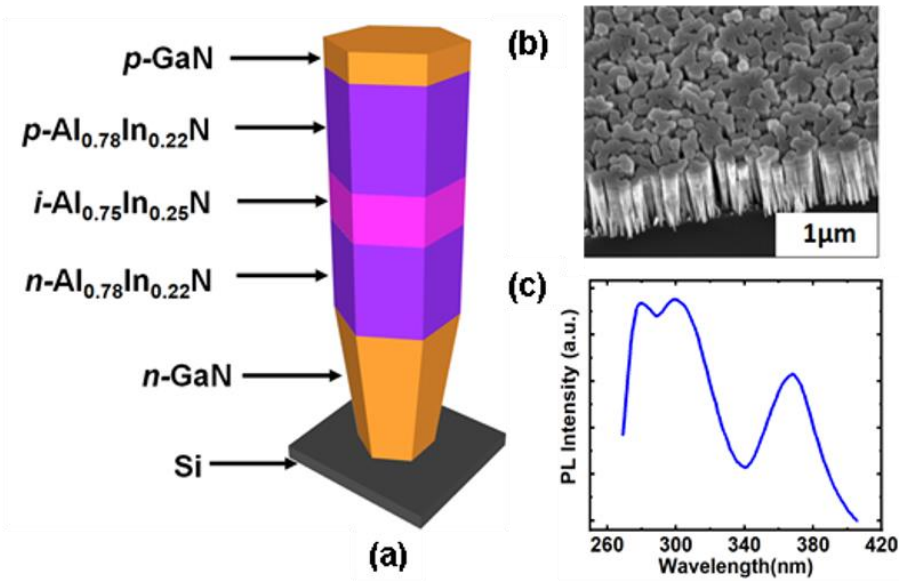

Figure 6.1 (a) Schematic structure of AlInN nanowire UV LED on Si substrate, (b) 45^o tilted scanning electron microscopy image of randomly grown AlInN nanowire UV LED sample on Si, (c) photoluminescence spectrum of AlInN nanowire UV LED. The emission peaks at 280 nm, 299 nm and 368 nm confirms $Al_{0.78}In_{0.22}N$, $Al_{0.75}In_{0.25}N$ quantum well, and GaN layers.

Next, current-voltage and electroluminescence (EL) characteristics were studied on fabricated nanowire UV LEDs as presented in Figure 6.2. From the current-voltage characteristics presented in Figure 6.2(a), it is found that turn-on voltage is ~5V and leakage current is less than 1 μA (at -8V). The optical microscopic image of the fabricated AlInN nanowire UV LEDs is shown in the inset of Figure 6.2(a). As illustrated in Figure 6.2(b), the AlInN nanowire UV LEDs have strong EL intensity with a peak wavelength at ~299 nm.

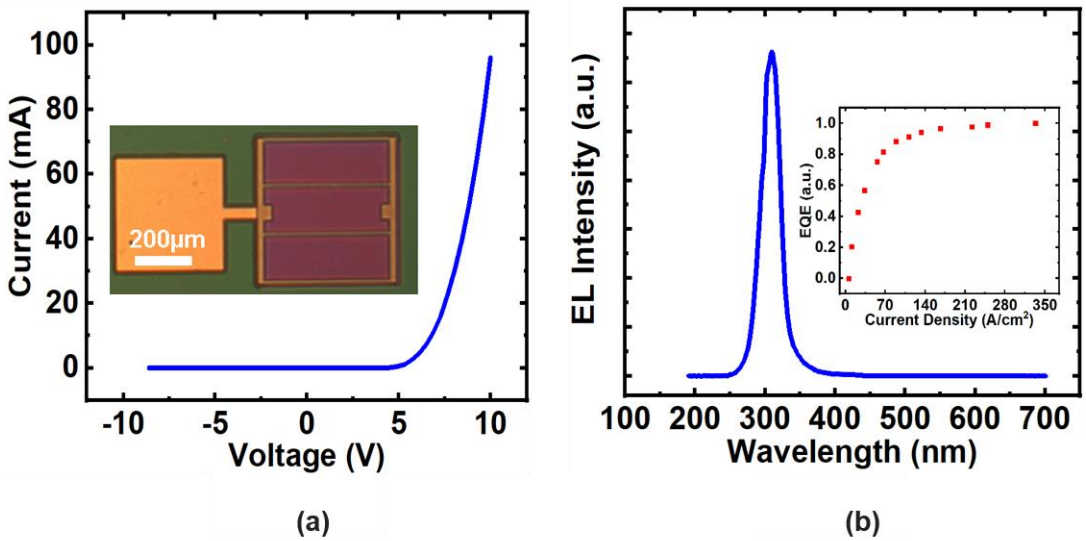

Figure 6.2 (a) I-V characteristic of AlInN nanowire UV LED. The inset figure shows picture of the fabricated device. (b) Electroluminescence spectrum of AlInN UV nanowire LED under 200 mA injection current and LED exhibit strong emission at 299 nm wavelength. The inset figure shows EQE as a function of current density of AlInN nanowire UV LED.

The inset of Figure 6.2(b) illustrates the EQE of the LED and it is observed that the EQE reaches its peak value at significantly higher current densities ~70 A/cm^2 which is attributed to the higher SRH recombination coefficient due to nonradiative surface recombination caused by the very large surface-to-volume ratio of nanowires [142]. However, there is no efficiency droop observed up to an injection current density of 350

A/cm^2. The relative EQE is measured at room temperature and under pulse biasing conditions (1% duty cycle) to eliminate the self-heating effect. Nanowires exhibit significantly reduced polarization field and dislocation density, compared to thin-film counterparts due to the effective strain relaxation. Therefore, efficiency droop-related mechanisms such as polarization field, electron and hole wave function separation in the quantum well, defect assisted Auger recombination, and electron leakage may be greatly reduced or eliminated [172-178].

6.3 Simulation & Results

Next, the LEE enhancement of the AlInN nanowire UV LEDs was studied using photonic crystal structures. To calculate the LEE of AlInN nanowire UV LEDs with different nanowire arrangements, FDTD analysis was done [179-181]. The LED structure used in the simulations consists of a random, square and hexagonal array of nanowires as depicted in Figure 6.3. Each nanowire in the array consists of 200 nm of *n*-GaN on Si substrate, 100 nm *n*-$Al_{0.78}In_{0.22}N$, 40 nm *i*-$Al_{0.75}In_{0.25}N$ quantum well, 100 nm *n*-$Al_{0.78}In_{0.22}N$ and 5 nm of *p*-GaN layer. Selective area growth approach, a well-establish technique can be used to grow hexagonal and square periodic nanowire arrays [182-185].

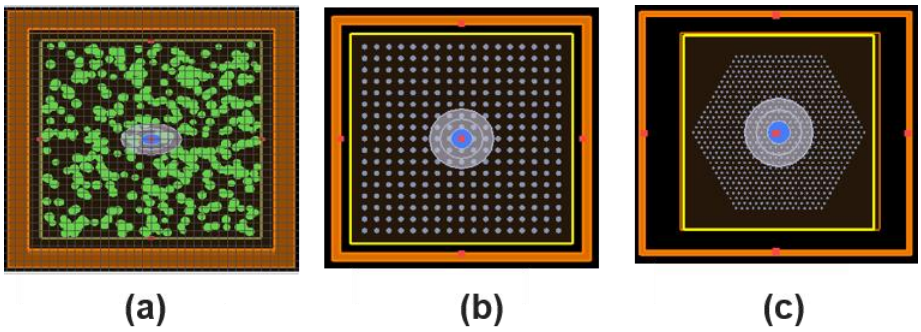

Figure 6.3 Top view of the simulated (a) Random array, (b) Square array, (c) Hexagonal array of AlInN nanowire UV LEDs.

The lattice constant and radius of the nanowires are defined as *a* and *r*, respectively. To avoid the reflection of outgoing waves back to the simulation space, the entire device with a side length of 2.5 μm is enclosed with 12 perfectly matched layers (PMLs) boundary conditions [186]. In the FDTD simulation, PML parameters such as attenuation factor (σ) and auxiliary attenuation coefficient (κ) are set to 0.25 and 2, respectively [166]. A minimum mesh step size of 0.25 nm and a maximum mesh step of 20 nm is used during the simulation. The refractive indices of the *n*-/*p*-$Al_{0.78}In_{0.22}N$, $Al_{0.75}In_{0.25}N$ and *n*-GaN/*p*-GaN regions considered in the simulations are 2.275, 2.266 and 2.625, respectively [187, 188]. The absorption coefficients of *n*-/*p*-$Al_{0.78}In_{0.22}N$, $Al_{0.75}In_{0.25}N$ and *n*-GaN/*p*-GaN regions considered in the simulations are 70000 cm^{-1}, 79000 cm^{-1} and 170000 cm^{-1}, respectively. For all the simulations, a single TM-polarized dipole source with the emission wavelength of 299 nm was positioned for estimating in the center of the active region. This is appropriate for estimating LEE for a large area LED device [170] as the previous study has shown that the use of multiple dipole sources results in a non-physical interference pattern which is undesirable for analysis of the optical properties of LEDs [189]. The source power monitors are used to measure the total power generated in the active region from the dipole source and these source power monitors are placed around the dipole source. To measure the total output power radiated out of the LED structure, output power monitors are placed around the UV LED nanowire structures. In this study, the absorption of light from the substrate is considered while calculating the LEE. Five output power monitors are used except the bottom monitor during calculations. The LEE is calculated as the ratio of the light output power measured by the output power monitors to the total

emitted power in the active region measured by the source power monitors. Table 6.1 summarizes the different parameters and their values used in the simulation.

Table 6.1 Different Parameters and Their Values Used During Simulation

Parameters	Considered values during simulation
Refractive index of *n*/*p*-GaN	2.625
Refractive index of *n*/*p*- $Al_{.78}In_{.22}N$	2.266
Refractive index of i-$Al_{.75}In_{.25}N$	2.275
Absorption coefficient of *n*/*p*-GaN	170000 cm^{-1}
Absorption coefficient of *n*/*p*- $Al_{.78}In_{.22}N$	70000 cm^{-1}
Absorption coefficient of i- $Al_{.75}In_{.25}N$	79000 cm^{-1}
Attenuation factor	0.25
Auxiliary attenuation coefficient	2
Mesh step size	0.25 – 20 nm
Temperature	300 K
Dipole source	TM mode
Center wavelength	299 nm
Simulation domain	2.5 µm × 2.5 µm

In the simulation study, first, the random nanowire UV LEDs are considered, which is a spontaneously grown nanowire array as shown in Figure 6.3(a). The structural randomness in this structure is introduced by dislocating the nanowires to random positions compared to periodic nanowire UV LEDs. The number of nanowires for random structure is the same as the number of nanowires in the hexagonal lattice structure for 2.5 µm of side length. The radius of the randomly grown nanowires varies from 40 nm to 64 nm, which is suitable for the MBE growth experiment. The average LEE for the randomly distributed nanowire array was observed to be around 20% to 33%. For every independent study, LEE was measured from both the top surface as well as the from the sides and found that out of

100%, around 75% of total LEE is being emitted from the top surface whereas around 25% is being emitted from the sidewalls of the nanowires. This suggests that, albeit the light is TM polarized, the dominant light emission direction is from the nanowire top surface, due to the strong light scattering effect [162]. However, the LEE for the random array of nanowires is found to be very low. Then, the variation of LEE for the square and hexagon topologies as shown in Figure 6.3(b) and Figure 6.3(c), respectively is investigated with respect to the key parameters for the periodic array such as nanowire radius and lattice constant. Here the light absorption from the top *p*-GaN and metal layer is not considered. During the simulation, the radius ranges of 40-64 nm and spacing ranges of 145-300 nm were considered. Spacing represents the center-to-center distance of adjacent nanowires.

To gain a complete understanding of the dependence of LEE on nanowires geometry, the contour plots of the LEE vs. nanowire radius and spacing for both the topologies of nanowire arrays are depicted in Figure 6.4. As shown in Figure 6.4(a), for the square array, the maximum LEE of ~56% was calculated at the spacing of 195 nm and radius of 40 nm. For hexagonal nanowire array, the maximum LEE is found to be ~63% at the spacing of 230 nm and radius of 60 nm as illustrated in Figure 6.4(b). It is understood that the geometry of the nanowire plays an important role in directing the generated photons from the active region to the air. It is also found that the maximum LEE of the hexagonal array of nanowire LED is higher than that of the square array. This could be related to the fact that the symmetry of the hexagonal array is higher than that of the square array, due to which guided modes in more directions can be transformed into radiation modes for hexagonal array [169, 190]. Therefore, optimized nanowire radius and spacing between the nanowires along with the arrangement of the nanowires could help to

overcome the total internal reflection at the semiconductor and air interface, improve the escape probability of the light and consequently increase the LEE. However, in the case of random nanowire UV LED design, multiple scattering of light inside the nanowires takes place due to spatially random and high contrast refractive index nanowires, which may localize the light inside the nanowires and causes the reduction of LEE. Therefore, the periodic array of nanowire LEDs are highly desired for light propagation through the structure to the surrounding air.

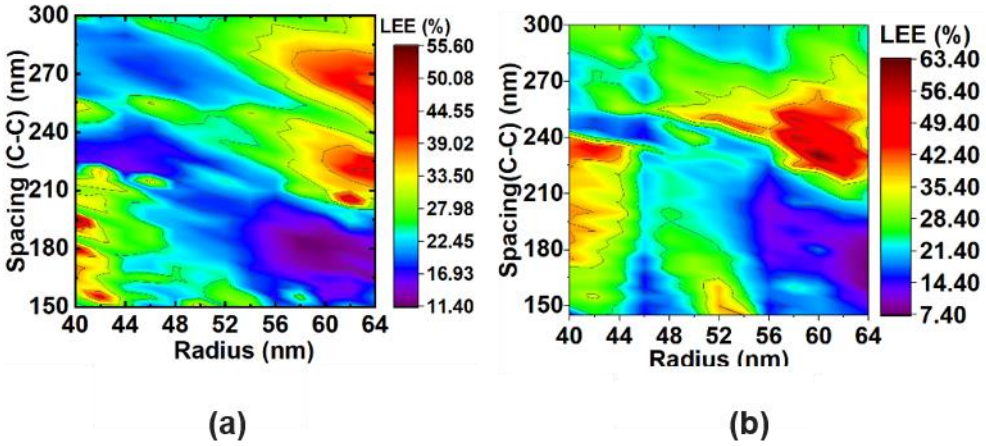

Figure 6.4 Contour plot of the LEE vs. nanowire radius and spacing for (a) square array, (b) hexagonal array of AlInN nanowire UV LEDs.

Photonic band structures of both these topologies were calculated based on the above-optimized parameters using MIT photonic-bands (MPB), which is an open-source, three-dimensional Eigen solver [191]. In Figure 6.5, the calculated photonic band structures of square and hexagonal arrays are plotted. The black line, known as the light line, separates the band diagram into two areas. The grey area above the light line corresponds to the continuum of radiation modes, while modes below the light line are guided modes that are confined within the nanowire arrays. In guided modes, light only propagates in the epitaxial layer because of satisfying the total internal reflection (TIR)

condition, however in radiated mode light can be emitted up or down to the outside of the LEDs because it does not satisfy the TIR condition [169, 192]. The red line, which represents the frequency of concern (a/λ) in this paper, lies at a location with few guided modes for the square array as shown in Fig. Figure 6.5(a), however, the red line lies in the gray area for the hexagonal array as shown in Figure 6.5(b), indicating the existence of radiated mode in the structure. This supports the vertical emission of the extracted light for TM polarized emission.

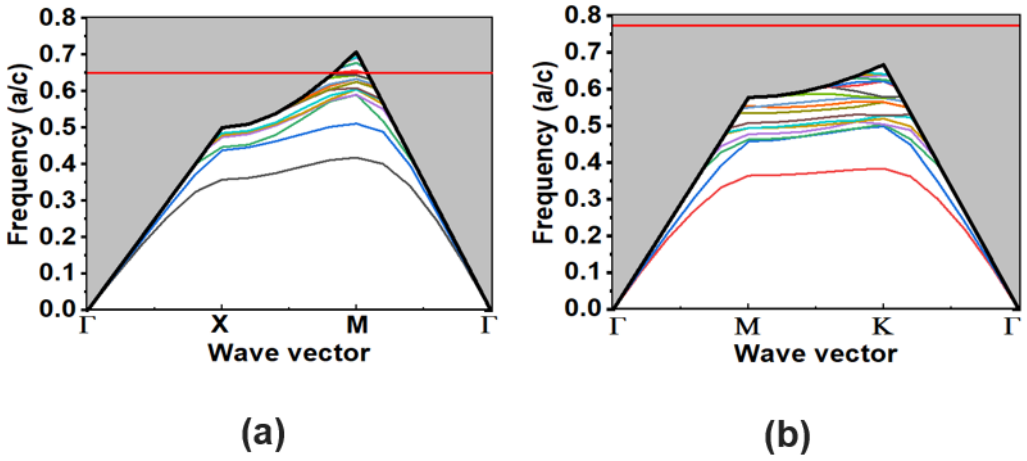

Figure 6.5 Photonic band diagrams of (a) square array and (b) Hexagonal array of AlInN nanowire UV LEDs. Horizontal red lines indicate the frequency of concern.

Next, the percentage of LEE for both the topologies was investigated from the top and sides of the nanowire and derived the contour plot of the LEE vs the nanowire radius and spacing as shown in Figure 6.6. The simulation results in both cases support the vertical emission of the LEE, although the nanowire structure favors highly TM-polarized emission [162]. For example, for the maximum LEE of ~56% in the case of a square array, ~41% of light extraction can be achieved from the top surface as shown in Figure 6.6(a), while ~15% of light extraction is obtained from the side walls of the nanowires as shown in Figure

6.6(b). Similarly, for the maximum LEE of ~63% in a hexagonal array, ~60% of light extraction can be achieved from the top surface as shown in Fig 6.6(c) while only ~3% of light extraction is obtained from the side walls of the nanowire as shown in Figure 6.6(d).

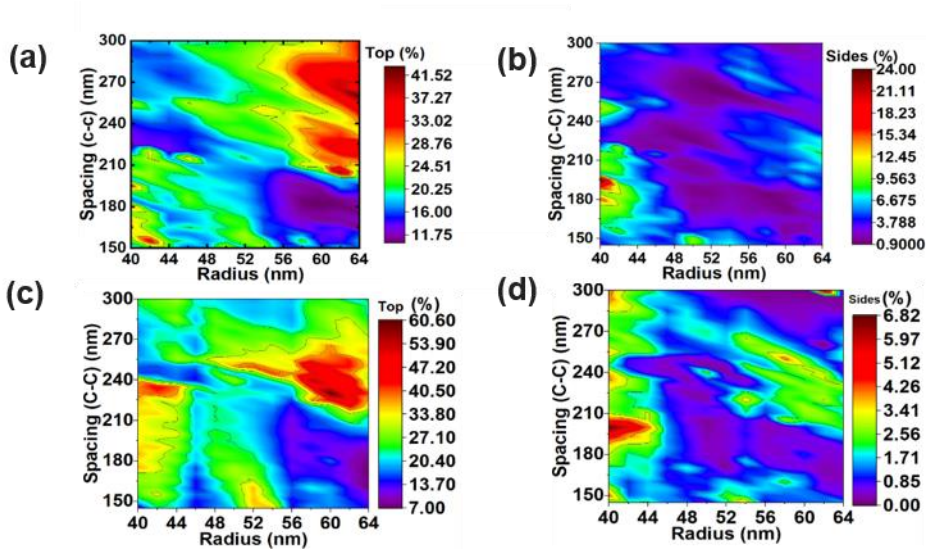

Figure 6.6 Contour plot of the LEE from top and sides vs. nanowire radius and spacing for square (a, b) and hexagonal (c, d) array structures of AlInN nanowire UV LEDs.

The vertical emission of TM polarized light can be affected by the top *p*-GaN contact layer as compared to the lateral side extraction of TM polarized emission. To further analyze the impact of the *p*-GaN layer, the variation of LEE vs thickness of the *p*-GaN layer is studied and plotted as depicted in Figure 6.7. The maximum LEE of the square lattice array for no *p*-GaN layer is observed to be ~55% at the radius of 40 nm and spacing of 195 nm and that of the hexagonal lattice array is observed to be ~63% for the radius of 60 nm and spacing of 230 nm, respectively. It is seen that with the increase in *p*-GaN thickness, LEE shows an overall decreasing trend due to the absorption in the thick *p*-GaN layer, which is like that observed in conventional planar LED structures. To achieve

maximum LEE, it is important to optimize the nanowire height and *p*-GaN thickness and/or replace *p*-GaN with a less absorptive and transparent *p*-AlGaN contact layer [59, 64].

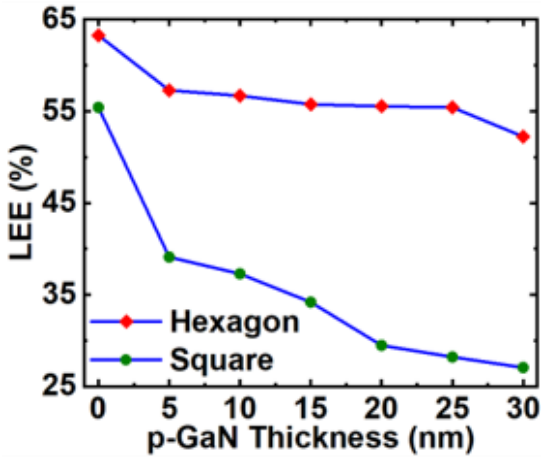

Figure 6.7 Variation of LEE vs. the thickness of *p*-GaN layer of AlInN UV LEDs.

6.4 Conclusion

In summary, we have demonstrated a high crystalline quality of AlInN nanowire LED structures with stable and strong EL emission at ~299 nm peak wavelength. Further, the light extraction characteristics are studied for different nanowire photonic crystal structure arrangements including hexagon and square lattices and compared the results with that of the random nanowire arrangement. Our simulation results show that the LEE of the square array and hexagonal array can reach ~56% and ~63%, respectively. However, for random nanowire arrays, the average LEE is around ~33% due to light multipath scattering among adjacent nanowires which localizes the light inside the nanowires. Therefore, ordered nanowire arrays exhibit higher LEEs compared to randomly arranged nanowire arrays. This work also provides a promising approach for fabricating high-efficiency UV nanowire LEDs using AlInN based semiconductors.

CHAPTER 7

DESIGN, FABRICATION, AND CHARACTERIZATION OF III-NITRIDE RESISTIVE RANDOM-ACCESS MEMORY (RRAM/ReRAM) DEVICES

7.1 Introduction

7.1.1 Motivation

In the present era, almost every electronic device has a memory element either attached externally or embedded with it and the requirement of memory devices is consistently increasing with the emerging of personal electronics including smartphones, digital cameras, computers etc. The ideal characteristics of a memory device are high density i.e., to store a large amount of data in a given die area so that the cost per bit of information stored can be minimized [193], good endurance (> 10^{16} cycles) i.e., the highest number of write/erase (or program/ erase) cycles that can be performed before the memory cell becomes unreliable, long retention i.e., the amount of time for which the information can be retained within the cell and must be at least 10 years for any practical application (>3 × 10^{8} s) [194], fast programming and access speed (< ns) so that the time spent on reading data from and writing data into the memory can be minimized and low power consumption. However, it is quite difficult to have a single memory device with all the above-mentioned properties. Based on the functionality and performance, the current memory system has a well-known classification such as static random-access memory (SRAM) and dynamic random-access memory (DRAM) volatile memories, and non-volatile memory like Flash Technology which is short for “flash electrically erasable programmable read-only memory”. The word “read-only” is a bit confusing since thesedays Flash memories can be

erased and programmed many times. Flash technology is a non-volatile memory storage medium that can be electrically erased and reprogrammed. The Flash technology has scaling limitations below 20 nm due to which several emerging memory technologies have been studied [195]. This is to continue the device scaling, further along, to achieve as many properties of an ideal memory device as possible to fulfill the future information storage requirements. Resistive random-access memory (RRAM/ReRAM) is one among those. RRAM is a promising alternative for Flash technology owing to its simple structure, high density, lower programming voltage and faster write/read speed, thus the initial target of RRAM technology development is to replace FLASH for mass storage applications.

7.1.2 Working principle of the RRAM device

RRAM device consists of a dielectric layer sandwiched in between the top and bottom electrodes as depicted in Figure 7.1(a) and works by changing the resistance across the dielectric layer by the application of external voltage. The pristine RRAM device is initially in a high resistance state (HRS) and relies on the formation, referred to low resistive state (LRS) and the rupture, referred to as HRS of conductive filament (CF). Based on the symmetry of I-V characteristics, RRAM can be classified into unipolar and bipolar devices. In unipolar device switching, the switching between LRS and HRS does not depend on the polarity of the applied voltage. i.e., switching can occur on applying a same polarity of voltage, but different magnitude. Here, during SET process compliance current (CC) needs to be applied to protect the filament generated during the process and no CC is applied during RESET to generate large current to break the CF. Thus, in unipolar devices, RESET current is usually higher than the SET current. On the other hand, in bipolar switching the LRS and HRS of the device depends on the polarity of the applied voltage, i.e., a transition

from HRS to LRS occurs at one polarity (either positive or negative) and the opposite polarity swiches the RRAM device back onto the HRS. In bipolar devices, the RESET current is much less as compared to unipolar devices, and thus it is more power efficient. In this work, bipolar RRAM devices are studied. Figure 7.1(b) depicts a sketch of I-V characteristics for a bipolar RRAM device. Here, for the SET operation, positive voltage is applied and negative voltage is applied for the RESET operation.

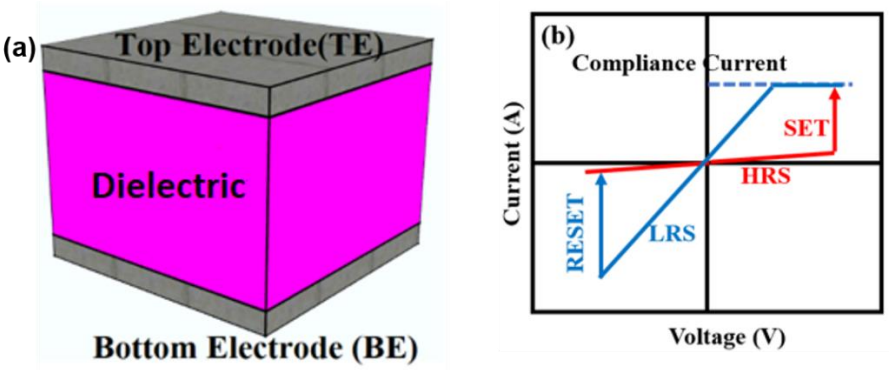

Figure 7.1 (a) Schematic of RRAM structure, (b) I-V characteristics of a bipolar RRAM

The working principle of the RRAM device is schematically shown in Figure 7.2. Upon the application of voltage to the top electrode, metal ions or defects get migrated through the dielectric layer where electric field, current density and local temperature are maximized within the device area. A string of vacancies forms a CF along with the oxide and switches the RRAM to a LRS, also called a SET process. Usually, the required voltage to switch from HRS to LRS for pristine devices is higher than the regular set voltage. This voltage is known as the forming voltage and the process is called the forming process. In bipolar devices, the subsequent application of opposite polarity of the voltage to the top electrode causes the metal ions or defects to migrate back to the top electrode that ruptures the CF, and eventually RRAM switches back to HRS, also known as the RESET process.

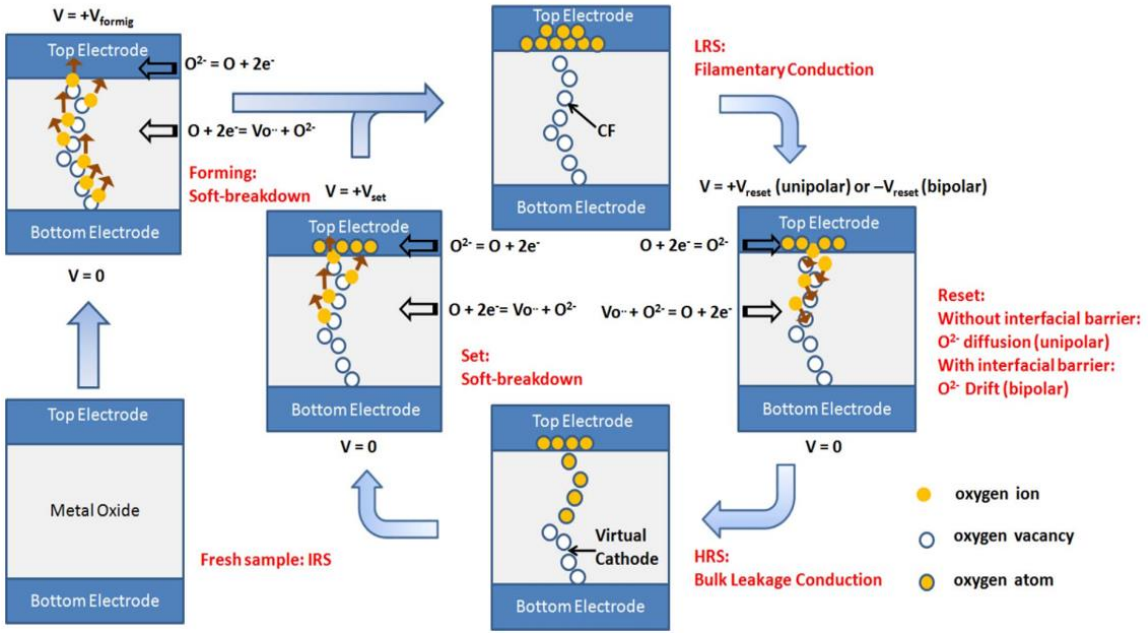

Figure 7.2 Working principle of RRAM device.
Source: [196]

7.1.3 Current State of the RRAM Technology for Different Dielectric Materials

In the early 1960s, few of the initial studies on the RRAM device using various oxide materials were already reported [197, 198]. Since Samsung demonstrated transition metal oxide (TMO) memory array integrated with the 0.18 µm silicon CMOS technology in 2004 [199], several studies have been focused on different binary oxides such as NiO_x [200], TiO_x [201], CuO_x [202], ZrO_x [203], ZnO_x [204], HfO_x [205, 206], TaO_x [207], AlO_x [208], and many others because of compatibility with silicon CMOS fabrication process. The switching behavior of the RRAM device is greatly affected by the choice of electrode materials. Different materials such as elementary substance electrodes (Al, Ti, Cu, Ag, W, Pt, etc), silicon-based electrodes (*n*-doped and *p*-doped Si), alloy electrodes (Cu-Ti, Cu-Te, Pt-Al, etc), nitride based electrodes (TiN, TaN), oxide based electrodes (Al doped ZnO, Ga doped ZnO, ITO) have been studied as electrodes for RRAM devices [209]. The list of

metal oxide materials along with different combination of top and bottom electrodes materials that have been used recently in the RRAM device fabrication are provided in Table 7.1.

Table 7.1 Various Oxide-based RRAM Studies

Year	TE	Dielectric	BE	Retention	Endurance (cycles)	V_f (V)	V_{set} (V)	V_{reset} (V)	I_{cc}
2007 [210]	Ti	ZrO_2	Pt	NS	$>10^4$	8.8	1	-	5 mA
2008 [211]	Pt	ZnO	Pt	NS	$>10^2$	3.3	-2	-1	NS
2008 [205]	TiN	TiO_x/HfO_x	TiN	~10^5 sec	$>10^6$	FF	1.5	-1.4	25µA
2008 [212]	Pt	NiO	Pt/Ti	NS	NS	5V	~1	~3.5	1mA
2009 [213]	Cu	TiO_2	Pt	NS	NS	NS	0.8	-1.5	300µA
2009 [214]	Ti	MnO_2	Pt	$>10^4$ sec	$>10^5$	NS	~0.7	~1.1	5mA
2010 [215]	Al/Ti	Al_2O_3	Pt	10^4 sec	$>10^3$	FF	1.5	~2	~1mA
2010 [216]	Au	ZrO_2	Ag	~10^4 sec	>500	FF	-0.5	0.6	1mA
2011 [217]	TiN	HfO_x/AlO_x	Pt	NS	10^6	~8	2.5	-3	300 µA
2012 [218]	Pt	ZnO	Pt	$>10^6$ sec	$>10^6$	4	1.2	-0.5	3mA
2013 [219]	Ta	TaO_x/TiO_2	Ti	$>10^4$ sec	$>10^{12}$	FF	5	-4 ~ -6	NS
2014 [220]	TiN	HfO_2	Pt	10^4 sec	NS	FF	-4.3	6	NS
2015 [221]	W/Zr	HfO_2	TiN	NS	$>10^6$	2	0.5	-	50µA
2015 [222]	Ti	HfO_2	TiN	10^4 sec	10^{10}	NS	3	-3.5	1mA
2016[223]	Ti/W	TiO_x/MgO	Ru	NS	$>10^3$	FF	1.4	-1.8	8mA
2017 [224]	TiN/Ti	TiO_{2-x}	Au	$>10^5$ sec	>50	FF	-0.5	< 1	1-200nA
2018 [225]	ITO	Zn_2TiO_4	Pt	$>10^4$sec	>500	25	0.6	-0.6	1-10mA
2019 [226]	Ni	AlO_x	Pt	$>10^4$sec	150	FF	<1.5	-1	1mA
2020 [227]	TiN/Al	AlO_x	Pt	10^4 sec	>100	3.3	1.4	-1.1	1mA, 5mA

7.1.4 Nitride-based RRAM Technology

The phase diagram of Al-N system is very simple and similar to that of the oxides [228]. Therefore ionic switching could also be possible in AlN material like in oxides [229]. AlN material can be considered as a potential candidate and alternative resistive switching (RS) layer for emerging non-volatile RRAM applications [230-239] due to their large energy bandgap (6.2 eV), high electrical resistivity (~10^{14} Ωcm), excellent dielectric properties (dielectric constant is 12.4), high hardness and good chemical and thermal stability [240, 241]. It is highly possible to achieve a large ON/OFF ratio in the case of AlN-based RRAM devices due to its wide bandgap, high electrical resistivity and high thermal conductivity

(134 W/cm K) which is desired. Another important point, metallic nitrides, such as TiN, WN and TaN, are commonly used as electrode materials in semiconductor fabrication foundries. This makes a semiconducting nitride such as AlN more attractive RS layer than oxides for RRAM. This approach reduces the chemical complexity and thermodynamic instability of an interface between an electrode nitride and a RS oxide layer by using all metal-nitride layers [242]. Also, the stable properties of AlN could be helpful in exhibiting high reliability in endurance and long retention periods [231]. III-nitride-based memory devices are also desirable with the integration of matured III-nitride high-electron-mobility transistors (HEMTs) and create a new generation of integrated circuits [243]. In addition, due to having a higher energy bandgap, thermal conductivity, thermal stability along a high breakdown field (0.95 MV/cm), emerging AlN is identified as an ideal candidate for memory applications in harsh electronics [244].

In this work, the switching capability of AlN as a RS layer is studied. Here, Ti (10 nm)/TiN (100 nm) acts as a bottom electrode (BE) and Ti (10 nm)/Pt (100 nm) works as a top electrode (TE). Here Ti is used as an adhesive layer. The AlN layer is sandwiched between the TE and BE; in which filament formation happens that is responsible for the switching. To find out the optimized AlN RS layer and the device size for high endurance, the thickness of the switching layer is varied from 2 nm to 100 nm and the considered device sizes are 10×10 μm^2, 20×20 μm^2, 50×50 μm^2, and 100×100 μm^2.

7.2 Fabrication

In this study, Pt/Ti/AlN/TiN/Ti devices are fabricated with multiple device sizes on SiO_2/Si substrates to study resistive switching behavior. The fabrication is started with a 2-inch silicon wafer covered by 270 nm thermally grown SiO_2 layer, which was used as the device

substrate. First, the wafer was cleaned using acetone and IPA to remove organic contamination. After that, Ti and TiN were sputter-deposited using the AJA sputter tool. The chamber pressure of around 1×10^{-8} torr was maintained during deposition. During the deposition process, first Argonne cleaning was done at a flow of 40sccm and pressure of 16mTorr for 60sec, followed by a 10 nm Ti layer was deposited to serve as an adhesion layer at a pressure of 3mTorr, power of 400W and Ar flow of 30sccm. Then a100 nm TiN layer was reactive sputtered which serves as the bottom electrode at a pressure of 3mTorr, power of 400W, Ar and N_2 flow of 15sccm.

After depositing the bottom electrode, different thicknesses of the switching layer i.e., AlN was deposited using both atomic layer deposition (ALD) and sputter deposition techniques. For AlN thicknesses with 2 nm, 5 nm, and 10 nm, ALD was used at 300°C temperature, 290W RF power and the deposition rate was 0.585A° per loop. To deposit 20 nm, 50 nm and 100 nm of AlN, AJA reactive sputtering was used at a pressure of 3mTorr, power of 400W, Ar and N_2 flow of 15sccm.

Next, a 50 nm of SiO_2 isolation layer was deposited using Oxford plasma-enhanced chemical vapor deposition (PECVD). For this, the wafer was loaded into the chamber, then the chamber pressure was pumped down and the chamber temperature was raised up to 300°C. At 140W power, the deposition rate was roughly 290 nm/min.

In the following steps, the SiO_2 layer was patterned. First, the priming process was done using liquid priming. For that, HMDS solution (typically 10%-20% HMDS in PGMEA) was applied to the static wafer. The solution was allowed to remain on the surface for 10secs, then spun off at a rate of 3000 rounds per minute (rpm) for 60sec to dry the wafer. PGMEA displaces the majority of any water on the surface of a bare wafer and

HMDS then displaces the silanol layer and binds to keep the surface dehydrated. Basically, HMDS improves the photoresist (PR) adhesion to the wafer surface. After primer, S1813 positive photoresist was applied and spun off at the rate of 3000 rpm for 60 sec followed by a one-minute soft bake at a temperature of 90°C. After soft bake, PR was exposed for 8sec using an ABM contact aligner. The exposed PR was then developed using MIF 726 positive PR developer for 60sec. After developing the PR, SiO_2 was removed using 6:1 buffer oxide etchant (BOE) to remove SiO_2.

Next, the wafer was loaded into the e-beam evaporator chamber for the top metal deposition. Ti and Pt sources were added into separate turrets. Then the cryopump was turned on to reach a base pressure around 2×10^{-6} Torr. During the evaporation, a 10 nm Ti layer was evaporated first to serve as an adhesion layer followed by a 100 nm Pt layer was deposited which serves as the top electrode.

Finally, after depositing Pt, the lift-off process was followed to remove the PR and get the final device. For lift-off, the wafer was kept in acetone for 30 minutes and ultrasonicated for 1 min, subsequently cleaned using IPA and DI, and dried using an N_2 gun. Figure 7.3(a) shows the schematic diagram of the flow of the fabrication procedure and Figure 7.3(b) shows the optical image of the top view of the fabricated devices with the device size of 20×20 μm^2.

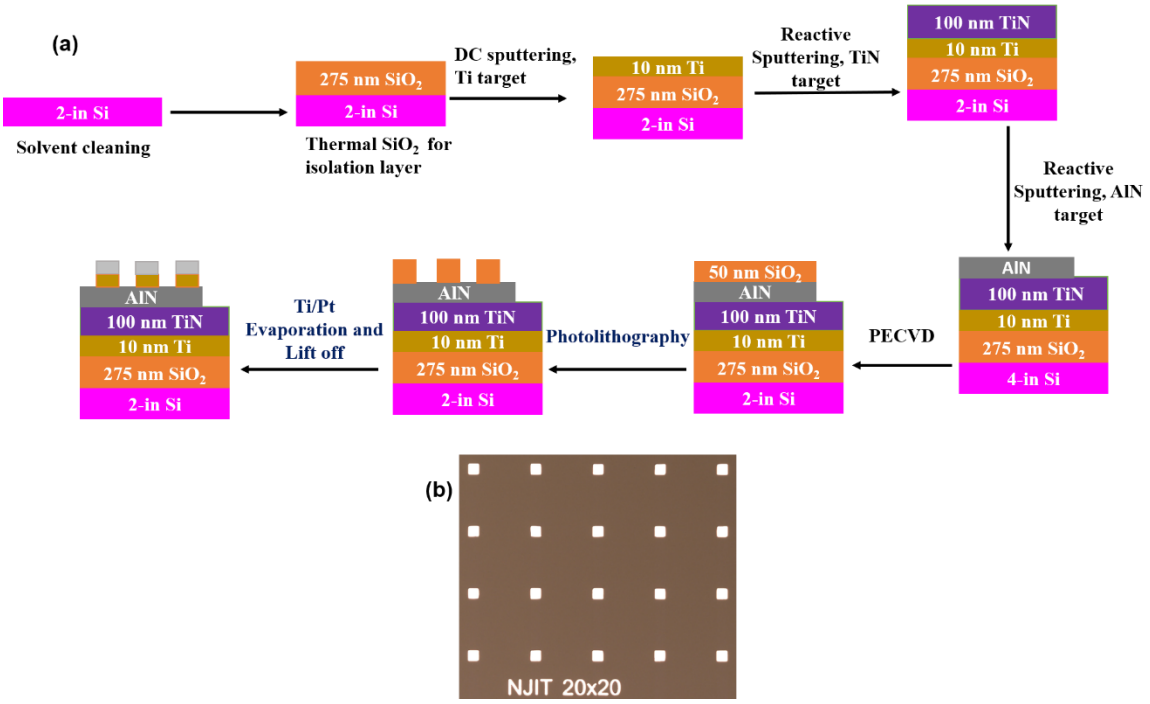

Figure 7.3 (a) Schematic diagram for different steps of device fabrication, (b) optical image of the top view of the fabricated devices with device size of 20×20 μm^2.

7.3 Characterization

The electrical properties of the fabricated RRAM devices were measured using Keysight B1500A semiconductor device parameter analyzer and cascade Microtech probe station. During measurements, CC was carefully chosen for each of the devices to avoid breakdown. Figure 7.4 illustrates an I-V characteristic of AlN based RRAM device with the device size of 10×10 μm^2 and AlN RS layer thicknesses including 5 nm, 10 nm, 15 nm, and 20 nm. The CC was set to 10 nA during the measurements. It is found that the set voltage is ~4V. It is expected that set voltage will be reduced by reducing the thickness of the AlN layer and it is indeed found that when the AlN thickness is reduced, the set voltage also reduced from ~4 V to ~2.3 V. This is because by reducing the RS layer thickness, the distance between the top and bottom electrodes will be reduced. This would reduce the

required voltage to accumulate sufficient vacancies for the switching. Further, the endurance of the RRAM device depends strongly on the cell size, wherein better endurance in RRAM devices with larger device sizes is reported [245].

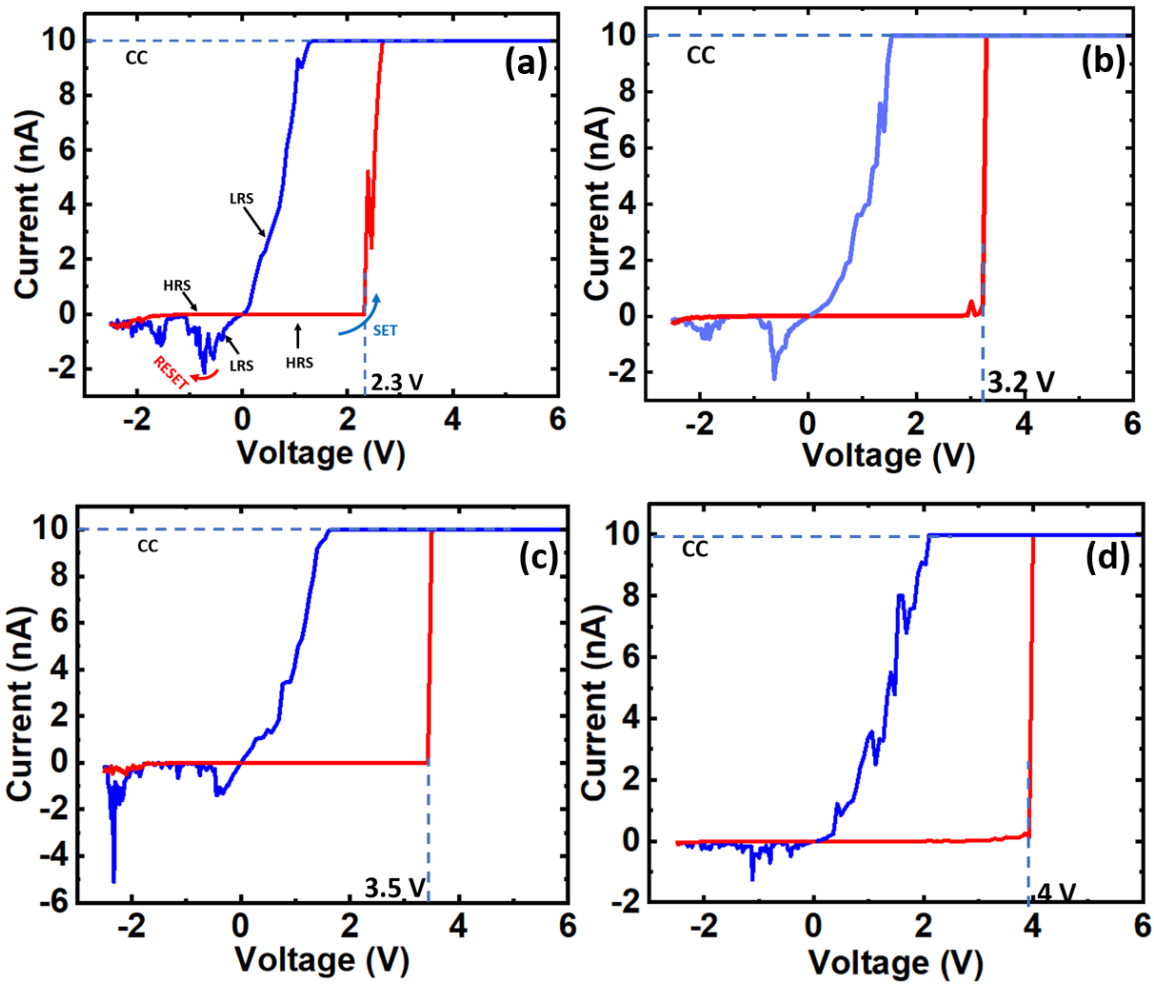

Figure 7.4 I-V characteristics of TiN/AlN/Pt RRAM device with AlN thickness of (a) 5 nm, (b) 10 nm, (c) 15 nm, and (d) 20 nm. HRS: High resistance state, LRS: Low resistance state, CC: Compliance current.

Our main objective is to build highly-stable ultra-low-power (few nano-Watts (nWs)) III-nitride RRAM devices which are a necessity for lower power computing applications. In this chapter, we have reported AlN RRAM devices which required only a few nWs of power to exhibit the device switching. However, the lower CC causes more

variability in SET and RESET characteristics and unstable conducting filament results to have not good endurance and retention properties [209]. In this regard, our next plan is to study the endurance and retention capabilities of our AlN RRAM devices. Further, it is also possible to reduce the SET voltage by creating more nitrogen vacancies in the AlN RS layer for a particular thickness. This could be achieved by integrating the optimized capping layer between AlN RS layer and TE.

7.4 Conclusion

In conclusion, we have carefully designed and fabricated the non-volatile AlN RRAM devices. Further, sharp resistive switching capabilities of the AlN RS layer are confirmed with the help of electrical characterization. It is observed that the SET voltage is reduced with the AlN RS layer thickness. Importantly, these AlN RRAM devices have a switching capability at a very low CC of 10 nA which is promising for low power applications.

CHAPTER 8

CONCLUSION & FUTURE OUTLOOK

In this dissertation, we have explored the design, fabrication, and characterization of III-nitride semiconductor devices for photonic and memory applications. We have reported highly stable, efficient, and truly white LEDs using InGaN/GaN dot-in-a-wire structure with the integration of two additional InGaN quantum wells grown using plasma-assisted molecular beam epitaxy. This special design of nanowire LED achieves the internal quantum efficiency of 58.5% without any virtual droop. Our developed theoretical model reveals that coupled QW before the active region reduces electron l_{MFP} thus boosting up the electron capture efficiency in the multiple quantum wells. It is also evident from the simulation results that integrated QW after the active region tremendously reduces electron leakage.

Electron leakage is one of the critical challenges in AlGaN deep UV LEDs which is severely limiting device performance. Different device design approaches have been presented here to address the electron leakage issue. First, we have band-engineered the EBL and optimized the device structure that is capable of mitigating the electron leakage from the active region and improving hole injection thus can emit bright light. We have proposed the replacement of conventional EBL with novel DSGS EBL which increases the effective CBBH without affecting the hole transportation. This specially designed UV LED improves power by ~3.54 times for ~254 nm wavelength UV LEDs and prevents electron leakage >10 times from the active region. Second, we have systematically designed QBs and introduced concave QBs in the AlGaN UV LED structure with ~284 nm wavelength emission. Our careful investigation of this structure has shown that specially designed

concave QBs are favorable for cooling down the hot electrons before entering into the QWs thus achieving lower electron l_{MFP} and velocity. This resulted in improving the electron capture capability in QWs, notably reducing electron leakage from the active region and output power by ~1.35 times. Third, we have designed the QBs with graded staircase structures and proposed EBL-free AlGaN UV LED. This EBL-free approach could successfully mitigate the electron leakage problem significantly without affecting the hole injection efficiency like in the conventional EBL approach. This structure exhibited significantly reduced thermal velocity, tremendously decreased electron leakage, reduced the quantum-confined Stark effect in the active region. As a result, both the internal quantum efficiency and output power of the GSQB structure are ~2.13 times higher than the conventional structure at 60 mA. Moving forward, these device design schemes presented here can be extended experimentally to investigate the improvement in the device performance for the nanowire AlGaN UV LEDs. The reported structure provides a promising approach for achieving high efficiency/power UV light emitters for practical applications.

Though $Al_xIn_{(1-x)}N$ semiconductor holds great potential applications in UV and visible light-emitting devices, it has not been widely explored due to difficulties in epitaxial growth. Going forward, we have demonstrated the high crystalline quality of the first AlInN nanowire UV LED structures grown using plasma-assisted molecular beam epitaxy with stable and strong EL emission at ~299 nm peak wavelength. Further, the light extraction characteristics are studied for different nanowire photonic crystal structure arrangements. Our calculations show that 63% of the light can be extracted using the optimized hexagonal photonic crystal array and the dominant light emission direction is

from the top surface of nanowires. This work also provides a promising approach for fabricating high-efficiency UV nanowire LEDs using AlInN based semiconductors.

We have further studied the resistive switching capabilities of AlN-based RRAM devices. These RRAM devices can be utilized for low power applications due to the switching capabilities at a very low CC of 10 nA. Moving forward, the impact of lateral and vertical scaling on the switching performance, endurance and reliability study on these devices can be done. Further, AlN RRAM devices can be studied using flexible substrates for wearable electronics applications and neuromorphic applications.

REFERENCES

[1] J. Piprek, "Efficiency droop in nitride-based light-emitting diodes," *Physica Status Solidi (a)*, vol. 207, no. 10, pp. 2217-2225, 2010.

[2] R. Haitz, F. Kish, J. Tsao, and J. Nelson, "The case for a national research program on semiconductor lighting," *Optoelectronics Industry Development Association*, pp. 1-24, 1999.

[3] T.-Y. Seong, J. Han, H. Amano, and H. Morkoç, "III-Nitride based light emitting diodes and applications," Dordrecht, Netherlands: Springer, 2013.

[4] E. F. Schubert and J. K. Kim, "Solid-state light sources getting smart," *Science*, vol. 308, no. 5726, pp. 1274-1278, 2005.

[5] D. Zhu and C. J. Humphreys, "Solid-state lighting based on light emitting diode technology," *Optics in our time*, Cham, Denmark: Springer 2016.

[6] N. Holonyak Jr and S. Bevacqua, "Coherent (visible) light emission from Ga (As1− x P x) junctions," *Applied Physics Letters*, vol. 1, no. 4, pp. 82-83, 1962.

[7] M. Gershenzon and R. Mikulyak, "Electroluminescence at p-n Junctions in Gallium Phosphide," *Journal of Applied Physics*, vol. 32, no. 7, pp. 1338-1348, 1961.

[8] H. á. Maruska and J. Tietjen, "The preparation and properties of vapor-deposited single-crystal-line GaN," *Applied Physics Letters*, vol. 15, no. 10, pp. 327-329, 1969.

[9] S. Yoshida, S. Misawa, and S. Gonda, "Improvements on the electrical and luminescent properties of reactive molecular beam epitaxially grown GaN films by using AlN-coated sapphire substrates," *Applied Physics Letters*, vol. 42, no. 5, pp. 427-429, 1983.

[10] H. Amano, N. Sawaki, I. Akasaki, and Y. Toyoda, "Metalorganic vapor phase epitaxial growth of a high quality GaN film using an AlN buffer layer," *Applied Physics Letters*, vol. 48, no. 5, pp. 353-355, 1986.

[11] H. Amano, M. Kito, K. Hiramatsu, and I. Akasaki, "P-type conduction in Mg-doped GaN treated with low-energy electron beam irradiation (LEEBI)," *Japanese Journal of Applied Physics*, vol. 28, no. 12A, p. L2112, 1989.

[12] S. Nakamura, T. Mukai, M. Senoh, and N. Iwasa, "Thermal annealing effects on p-type Mg-doped GaN films," *Japanese Journal of Applied Physics*, vol. 31, no. 2B, p. L139, 1992.

[13] S. Nakamura, T. Mukai, and M. Senoh, "High-power GaN pn junction blue-light-emitting diodes," *Japanese Journal of Applied Physics,* vol. 30, no. 12A, p. L1998, 1991.

[14] S. Nakamura, M. Senoh, and T. Mukai, "P-GaN/N-InGaN/N-GaN double-heterostructure blue-light-emitting diodes," *Japanese Journal of Applied Physics,* vol. 32, no. 1A, p. L8, 1993.

[15] S. Nakamura, T. Mukai, and M. Senoh, "Candela-class high-brightness InGaN/AlGaN double-heterostructure blue-light-emitting diodes," *Applied Physics Letters,* vol. 64, no. 13, pp. 1687-1689, 1994.

[16] S. Nakamura, M. Senoh, N. Iwasa, and S.-i. Nagahama, "High-brightness InGaN blue, green and yellow light-emitting diodes with quantum well structures," *Japanese Journal of Applied Physics,* vol. 34, no. 7A, p. L797, 1995.

[17] S. Nakamura, M. Senoh, N. Iwasa, S.-i. Nagahama, T. Yamada, and T. Mukai, "Superbright green InGaN single-quantum-well-structure light-emitting diodes," *Japanese Journal of Applied Physics,* vol. 34, no. 10B, p. L1332, 1995.

[18] S. Nakamura, S. Pearton, and G. Fasol, "The blue laser diode: the complete story," *Springer Science & Business Media,* 2000.

[19] E. F. Schubert, J. Cho, and J. K. Kim, "Light-emitting diodes," *Kirk-Othmer Encyclopedia of Chemical Technology,* pp. 1-20, 2000.

[20] J. Cho, J. H. Park, J. K. Kim, and E. F. Schubert, "White light-emitting diodes: history, progress, and future," *Laser & Photonics Reviews,* vol. 11, no. 2, p. 1600147, 2017.

[21] S. P. DenBaars, D. Feezell, K. Kelchner, S. Pimputkar, C.C. Pan, C. C. Yen, S. Tanaka, Y. Zhao, N. Pfaff, R. Farrell, and M. Iza,, "Development of gallium-nitride-based light-emitting diodes (LEDs) and laser diodes for energy-efficient lighting and displays," *Acta Materialia,* vol. 61, no. 3, pp. 945-951, 2013.

[22] S. Zhao, H. P. T. Nguyen, M. G. Kibria, and Z. Mi, "III-Nitride nanowire optoelectronics," *Progress in Quantum Electronics,* vol. 44, pp. 14-68, 2015,

[23] C. Wood and D. Jena, "Polarization effects in semiconductors: from ab initio theory to device applications," *Springer Science & Business Media,* 2007.

[24] T. Zhu and R. A. Oliver, "Unintentional doping in GaN," *Physical Chemistry Chemical Physics,* vol. 14, no. 27, pp. 9558-9573, 2012.

[25] J. Cho, E. F. Schubert, and J. K. Kim, "Efficiency droop in light-emitting diodes: Challenges and countermeasures," *Laser & Photonics Reviews,* vol. 7, no. 3, pp. 408-421, 2013.

[26] C.-C. Pan, S. Tanaka, F. Wu, Y. Zhao, J. S. Speck, S. Nakamura, S. P. DenBaars, S.P. and D. Feezell "High-power, low-efficiency-droop semipolar (2021) single-quantum-well blue light-emitting diodes," *Applied Physics Express,* vol. 5, no. 6, p. 062103, 2012.

[27] G. Li, W. Wang, W. Yang, Y. Lin, H. Wang, Z. Lin, and S. Zhou, "GaN-based light-emitting diodes on various substrates: a critical review," *Reports on Progress in Physics,* vol. 79, no. 5, p. 056501, 2016.

[28] G. Baraff and M. Schlüter, "Electronic structure, total energies, and abundances of the elementary point defects in GaAs," *Physical Review Letters,* vol. 55, no. 12, p. 1327, 1985.

[29] R. Longini and R. Greene, "Ionization interaction between impurities in semiconductors and insulators," *Physical Review,* vol. 102, no. 4, p. 992, 1956.

[30] W. Qian, G. Rohrer, M. Skowronski, K. Doverspike, L. Rowland, and D. Gaskill, "Open-core screw dislocations in GaN epilayers observed by scanning force microscopy and high-resolution transmission electron microscopy," *Applied Physics Letters,* vol. 67, no. 16, pp. 2284-2286, 1995.

[31] L. Romano, B. Krusor, and R. Molnar, "Structure of GaN films grown by hydride vapor phase epitaxy," *Applied Physics Letters,* vol. 71, no. 16, pp. 2283-2285, 1997.

[32] X. H. Wu, L. M. Brown, D. Kapolnek, S. Keller, B. Keller, S. P. DenBaars, and J. S. Speck, "Defect structure of metal-organic chemical vapor deposition-grown epitaxial (0001) GaN/Al2O3," *Journal of Applied Physics,* vol. 80, no. 6, pp. 3228-3237, 1996.

[33] Z. Liliental-Weber, C. Kisielowski, S. Ruvimov, Y. Chen, J. Washburn, I. Grzegory, M. Bockowski, J. Jun, and S. Porowski, "Structural characterization of bulk GaN crystals grown under high hydrostatic pressure," *Journal of Electronic Materials,* vol. 25, no. 9, pp. 1545-1550, 1996.

[34] H.-Y. Ryu, H.-S. Kim, and J.-I. Shim, "Rate equation analysis of efficiency droop in InGaN light-emitting diodes," *Applied Physics Letters,* vol. 95, no. 8, p. 081114, 2009.

[35] Q. Dai, Q. Shan, J. Wang, S. Chhajed, J. Cho, E. F. Schubert, M. H. Crawford, D. D. Koleske, M.-H. Kim, and Y. Park, "Carrier recombination mechanisms and efficiency droop in GaInN/GaN light-emitting diodes," *Applied Physics Letters,* vol. 97, no. 13, p. 133507, 2010.

[36] J. Piprek, *Semiconductor optoelectronic devices: introduction to physics and simulation*. Elsevier, 2013.

[37] A. Laubsch, M. Sabathil, J. Baur, M. Peter, and B. Hahn, "High-power and high-efficiency InGaN-based light emitters," *IEEE Transactions on Electron Devices,* vol. 57, no. 1, pp. 79-87, 2009.

[38] M. Meneghini, N. Trivellin, G. Meneghesso, E. Zanoni, U. Zehnder, and B. Hahn, "A combined electro-optical method for the determination of the recombination parameters in InGaN-based light-emitting diodes," *Journal of Applied Physics,* vol. 106, no. 11, p. 114508, 2009.

[39] M. Zhang, P. Bhattacharya, J. Singh, and J. Hinckley, "Direct measurement of auger recombination in In 0.1 Ga 0.9 N/GaN quantum wells and its impact on the efficiency of In 0.1 Ga 0.9 N/GaN multiple quantum well light emitting diodes," *Applied Physics Letters,* vol. 95, no. 20, p. 201108, 2009.

[40] J. Piprek, R. Farrell, S. DenBaars, and S. Nakamura, "Effects of built-in polarization on InGaN-GaN vertical-cavity surface-emitting lasers," *IEEE Photonics Technology Letters,* vol. 18, no. 1, pp. 7-9, 2005.

[41] H. P. T. Nguyen, K. Cui, S. Zhang, M. Djavid, A. Korinek, G. A. Botton, and Z. Mi, "Controlling electron overflow in phosphor-free InGaN/GaN nanowire white light-emitting diodes," *Nano Letters,* vol. 12, no. 3, pp. 1317-1323, 2012.

[42] J. Piprek and S. Li, "Electron leakage effects on GaN-based light-emitting diodes," *Optical and Quantum Electronics,* vol. 42, no. 2, pp. 89-95, 2010.

[43] J. Liu, J.-H. Ryou, R. Dupuis, J. Han, G. Shen, and H. Wang, "Barrier effect on hole transport and carrier distribution in In Ga N⁄ Ga N multiple quantum well visible light-emitting diodes," *Applied Physics Letters,* vol. 93, no. 2, p. 021102, 2008.

[44] X. Ni, Q. Fan, R. Shimada, Ü. Özgür, and H. Morkoç, "Reduction of efficiency droop in InGaN light emitting diodes by coupled quantum wells," *Applied Physics Letters,* vol. 93, no. 17, p. 171113, 2008.

[45] M.-C. Tsai, S.-H. Yen, Y.-C. Lu, and Y.-K. Kuo, "Numerical study of blue InGaN light-emitting diodes with varied barrier thicknesses," *IEEE Photonics Technology Letters,* vol. 23, no. 2, pp. 76-78, 2010.

[46] S. Nakamura, N. Iwasa, M. Senoh, and T. Mukai, "Hole compensation mechanism of p-type GaN films," *Japanese Journal of Applied Physics,* vol. 31, no. 5R, p. 1258, 1992.

[47] G. Namkoong, E. Trybus, K. K. Lee, M. Moseley, W. A. Doolittle, and D. C. Look, "Metal modulation epitaxy growth for extremely high hole concentrations above 10 19 cm− 3 in GaN," *Applied Physics Letters,* vol. 93, no. 17, p. 172112, 2008.

[48] M. Zhang, P. Bhattacharya, W. Guo, and A. Banerjee, "Mg doping of GaN grown by plasma-assisted molecular beam epitaxy under nitrogen-rich conditions," *Applied Physics Letters,* vol. 96, no. 13, p. 132103, 2010.

[49] E. Ertekin, P. A. Greaney, D. Chrzan, and T. D. Sands, "Equilibrium limits of coherency in strained nanowire heterostructures," *Journal of Applied Physics,* vol. 97, no. 11, p. 114325, 2005.

[50] S. D. Hersee, A. K. Rishinaramangalam, M. N. Fairchild, L. Zhang, and P. Varangis, "Threading defect elimination in GaN nanowires," *Journal of Materials Research,* vol. 26, no. 17, pp. 2293-2298, 2011.

[51] W. Guo, M. Zhang, A. Banerjee, and P. Bhattacharya, "Catalyst-free InGaN/GaN nanowire light emitting diodes grown on (001) silicon by molecular beam epitaxy," *Nano Letters,* vol. 10, no. 9, pp. 3355-3359, 2010.

[52] H. P. T. Nguyen, S. Zhang, K. Cui, X. Han, S. Fathololoumi, M. Couillard, G. A. Botton, and Z. Mi, "p-Type modulation doped InGaN/GaN dot-in-a-wire white-light-emitting diodes monolithically grown on Si (111)," *Nano Letters,* vol. 11, no. 5, pp. 1919-1924, 2011.

[53] S. D. Hersee, X. Sun, and X. Wang, "The controlled growth of GaN nanowires," *Nano Letters,* vol. 6, no. 8, pp. 1808-1811, 2006.

[54] H.-W. Lin, Y.-J. Lu, H.-Y. Chen, H.-M. Lee, and S. Gwo, "InGaN/GaN nanorod array white light-emitting diode," *Applied Physics Letters,* vol. 97, no. 7, p. 073101, 2010.

[55] C.-H. Chang, L.-Y. Chen, L.-C. Huang, Y.-T. Wang, T.-C. Lu, and J. J. Huang, "Effects of strains and defects on the internal quantum efficiency of InGaN/GaN nanorod light emitting diodes," *IEEE Journal of Quantum Electronics,* vol. 48, no. 4, pp. 551-556, 2012.

[56] S. E. Brinkley *et al.*, "Chip shaping for light extraction enhancement of bulk c-plane light-emitting diodes," *Applied Physics Express,* vol. 5, no. 3, p. 032104, 2012.

[57] H.-W. Huang, C. Kao, J. Chu, H. Kuo, S. Wang, and C. Yu, "Improvement of InGaN-GaN light-emitting diode performance with a nano-roughened p-GaN surface," *IEEE Photonics Technology Letters,* vol. 17, no. 5, pp. 983-985, 2005.

[58] Y.-C. Lee, C.-H. Ni, and C.-Y. Chen, "Enhancing light extraction mechanisms of GaN-based light-emitting diodes through the integration of imprinting

microstructures, patterned sapphire substrates, and surface roughness," *Optics Express,* vol. 18, no. 104, pp. A489-A498, 2010.

[59] X. Liu, K. Mashooq, T. Szkopek, and Z. Mi, "Improving the efficiency of transverse magnetic polarized emission from AlGaN based LEDs by using nanowire photonic crystal," *IEEE Photonics Journal,* vol. 10, no. 4, pp. 1-11, 2018.

[60] J. K. Kim, A. N. Noemaun, F. W. Mont, D. Meyaard, E. F. Schubert, D. J. Poxson, H. Kim, C. Sone, and Y. Park, "Elimination of total internal reflection in GaInN light-emitting diodes by graded-refractive-index micropillars," *Applied Physics Letters,* vol. 93, no. 22, p. 221111, 2008.

[61] K. Okamoto, I. Niki, A. Shvartser, Y. Narukawa, T. Mukai, and A. Scherer, "Surface-plasmon-enhanced light emitters based on InGaN quantum wells," *Nature Materials,* vol. 3, no. 9, p. 601, 2004.

[62] J. Shakya, K. Knabe, K. Kim, J. Li, J. Lin, and H. Jiang, "Polarization of III-nitride blue and ultraviolet light-emitting diodes," *Applied Physics Letters,* vol. 86, no. 9, p. 091107, 2005.

[63] H.-Y. Ryu, I.-G. Choi, H.-S. Choi, and J.-I. Shim, "Investigation of light extraction efficiency in AlGaN deep-ultraviolet light-emitting diodes," *Applied Physics Express,* vol. 6, no. 6, p. 062101, 2013.

[64] Y. K. Ooi, C. Liu, and J. Zhang, "Analysis of polarization-dependent light extraction and effect of passivation layer for 230-nm AlGaN nanowire light-emitting diodes," *IEEE Photonics Journal,* vol. 9, no. 4, pp. 1-12, 2017.

[65] B. W. D'Andrade and S. R. Forrest, "White organic light-emitting devices for solid-state lighting," *Advanced Materials,* vol. 16, no. 18, pp. 1585-1595, 2004.

[66] Y. Narukawa, "White-light LEDS," *Optics and Photonics News,* vol. 15, no. 4, pp. 24-29, 2004.

[67] S. Nakamura, "Current status of GaN-based solid-state lighting," *MRS Bulletin,* vol. 34, no. 2, pp. 101-107, 2009.

[68] N. Narendran and L. Deng, "Color rendering properties of LED light sources," in *Solid State Lighting II,* 2002, vol. 4776: International Society for Optics and Photonics, pp. 61-67.

[69] R. Mueller-Mach, G. Mueller, M. R. Krames, H. A. Höppe, F. Stadler, W. Schnick, T. Juestel, and P. Schmidt, "Highly efficient all-nitride phosphor-converted white

light emitting diode," *Physica Status Solidi (a)*, vol. 202, no. 9, pp. 1727-1732, 2005.

[70] H. P. T. Nguyen, K. Cui, S. Zhang, S. Fathololoumi, and Z. Mi, "Full-color InGaN/GaN dot-in-a-wire light emitting diodes on silicon," *Nanotechnology*, vol. 22, no. 44, p. 445202, 2011.

[71] W. Guo, A. Banerjee, P. Bhattacharya, and B. S. Ooi, "InGaN/GaN disk-in-nanowire white light emitting diodes on (001) silicon," *Applied Physics Letters*, vol. 98, no. 19, p. 193102, 2011.

[72] I. Rozhansky and D. Zakheim, "Analysis of the causes of the decrease in the electroluminescence efficiency of AlGaInN light-emitting-diode heterostructures at high pumping density," *Semiconductors*, vol. 40, no. 7, pp. 839-845, 2006.

[73] C. G. Van de Walle and D. Segev, "Microscopic origins of surface states on nitride surfaces," *Journal of Applied Physics*, vol. 101, no. 8, p. 081704, 2007.

[74] Ü. Ozgur, H. Liu, X. Li, X. Ni, and H. Morkoc, "GaN-based light-emitting diodes: Efficiency at high injection levels," *Proceedings of the IEEE*, vol. 98, no. 7, pp. 1180-1196, 2010.

[75] S.-H. Yen, M.-L. Tsai, M.-C. Tsai, S.-J. Chang, and Y.-K. Kuo, "Investigation of optical performance of InGaN MQW LED with thin last barrier," *IEEE Photonics Technology Letters*, vol. 22, no. 24, pp. 1787-1789, 2010.

[76] S.-H. Han, D. Y. Lee, S. J. Lee, C. Y. Cho, M. K. Kwon, S. P. Lee, D. Y. Noh, D. J. Kim, Y. C. Kim, and S. J. Park, "Effect of electron blocking layer on efficiency droop in InGaN/GaN multiple quantum well light-emitting diodes," *Applied Physics Letters*, vol. 94, no. 23, p. 231123, 2009.

[77] N. Wang, Y. A. Yin, B. Zhao, and T. Mei, "Performance Analysis of GaN-Based Light-Emitting Diodes With Lattice-Matched InGaN/AlInN/InGaN Quantum-Well Barriers," *Journal of Display Technology*, vol. 11, no. 12, pp. 1056-1060, 2015.

[78] B. Jain, R. T. Velpula, M. Tumuna, H. Q. T. Bui, J. Jude, T. T. Pham, A. V. Hoang, R. Wang, and H. P. T. Nguyen, "Enhancing the light extraction efficiency of AlInN nanowire ultraviolet light-emitting diodes with photonic crystal structures," *Optics Express*, vol. 28, no. 15, pp. 22908-22918, 2020.

[79] Ü. Özgür, X. Ni, X. Li, J. Lee, S. Liu, S. Okur, V. Avrutin, A. Matulionis, and C. H. Morkoç, "Ballistic transport in InGaN-based LEDs: impact on efficiency," *Semiconductor Science and Technology*, vol. 26, no. 1, p. 014022, 2010.

[80] K.-T. Tsen, R. P. Joshi, D. K. Ferry, A. Botchkarev, B. Sverdlov, A. Salvador, and H. Morkoç, "Nonequilibrium electron distributions and phonon dynamics in wurtzite GaN," *Applied Physics Letters,* vol. 68, no. 21, pp. 2990-2992, 1996.

[81] H. P. T. Nguyen, M. Djavid, S. Y. Woo, X. Liu, A. T. Connie, S. Sadaf, Q. Wang, G. A. Botton, I. Shih, and Z. Mi, "Engineering the carrier dynamics of InGaN nanowire white light-emitting diodes by distributed p-AlGaN electron blocking layers," *Scientific Reports,* vol. 5, p. 7744, 2015.

[82] Z.-H. Zhang, W. Liu, S. T. Tan, Z. Ju, Y. Ji, Z. Kyaw, X. Zhang, N. Hasanov, B. Zhu, S. Lu, and Y. Zhang, "On the mechanisms of InGaN electron cooler in InGaN/GaN light-emitting diodes," *Optics Express,* vol. 22, no. 103, pp. A779-A789, 2014.

[83] X. Ni, X. Li, J. Lee, S. Liu, V. Avrutin, Ü. Özgür, H. Morkoç, and A. Matulionis, "Hot electron effects on efficiency degradation in InGaN light emitting diodes and designs to mitigate them," *Journal of Applied Physics,* vol. 108, no. 3, p. 033112, 2010.

[84] X. Ni, X. Li, J. Lee, S. Liu, Vitaliy Avrutin, Ü. Özgür, H. Morkoç, A. Matulionis, T. Paskova, G. Mulholland, and K. R. Evans, "InGaN staircase electron injector for reduction of electron overflow in InGaN light emitting diodes," *Applied Physics Letters,* vol. 97, no. 3, p. 031110, 2010.

[85] M. F. Schubert and E. F. Schubert, "Effect of heterointerface polarization charges and well width upon capture and dwell time for electrons and holes above GaInN/GaN quantum wells," *Applied Physics Letters,* vol. 96, no. 13, p. 131102, 2010.

[86] S.-C. Ling, T.-C. Lu, S.-P. Chang, J.-R. Chen, H.-C. Kuo, and S.-C. Wang, "Low efficiency droop in blue-green m-plane InGaN/GaN light emitting diodes," *Applied Physics Letters,* vol. 96, no. 23, p. 231101, 2010.

[87] H. J. Chung, R. J. Choi, M. H. Kim, J. W. Han, Y. M. Park, Y. S. Kim, H. S. Paek, C. S. Sone, Y. J. Park, J. K. Kim, and E. F. Schubert, "Improved performance of GaN-based blue light emitting diodes with InGaN/GaN multilayer barriers," *Applied Physics Letters,* vol. 95, no. 24, p. 241109, 2009.

[88] K. Song, M. Mohseni, and F. Taghipour, "Application of ultraviolet light-emitting diodes (UV-LEDs) for water disinfection: A review," *Water Research,* vol. 94, pp. 341-349, 2016.

[89] N. G. Yeh, C.-H. Wu, and T. C. Cheng, "Light-emitting diodes—their potential in biomedical applications," *Renewable and Sustainable Energy Reviews,* vol. 14, no. 8, pp. 2161-2166, 2010.

[90] S.-W. Fan, A. K. Srivastava, and V. P. Dravid, "UV-activated room-temperature gas sensing mechanism of polycrystalline ZnO," *Applied Physics Letters,* vol. 95, no. 14, p. 142106, 2009.

[91] Y. Muramoto, M. Kimura, and S. Nouda, "Development and future of ultraviolet light-emitting diodes: UV-LED will replace the UV lamp," *Semiconductor Science and Technology,* vol. 29, no. 8, p. 084004, 2014.

[92] J. Zhang, X. Hu, A. Lunev, J. Deng, Y. Bilenko, T. M. Katona, M. S. Shur, R. Gaska, and M. A. Khan, "AlGaN deep-ultraviolet light-emitting diodes," *Japanese Journal of Applied Physics,* vol. 44, no. 10R, p. 7250, 2005.

[93] J. Simon, V. Protasenko, C. Lian, H. Xing, and D. Jena, "Polarization-induced hole doping in wide–band-gap uniaxial semiconductor heterostructures," *Science,* vol. 327, no. 5961, pp. 60-64, 2010.

[94] P. Dong, J. Yan, J. Wang, Y. Zhang, C. Geng, T. Wei, P. Cong,Y. Zhang, J. Zeng, Y. Tian, and L. Sun, "282-nm AlGaN-based deep ultraviolet light-emitting diodes with improved performance on nano-patterned sapphire substrates," *Applied Physics Letters,* vol. 102, no. 24, p. 241113, 2013.

[95] M. Zhang, Y. Li, S. Chen, W. Tian, J. Xu, X. Li, Z. Wu, Y. Fang, J. Dai, and C. Chen, "Performance improvement of AlGaN-based deep ultraviolet light-emitting diodes by using staggered quantum wells," *Superlattices and Microstructures,* vol. 75, pp. 63-71, 2014.

[96] R. Akaike, S. Ichikawa, M. Funato, and Y. Kawakami, "Al x Ga1− x N-based semipolar deep ultraviolet light-emitting diodes," *Applied Physics Express,* vol. 11, no. 6, p. 061001, 2018.

[97] B. Jain, R. T. Velpula, T. Bui, F. M. Shakiba, J. Jude, M. Tumuna, H.-D. Nguyen, T. R. Lenka, and H. P. T. Nguyen, "Improving Carrier Transport in AlGaN Deep UltravioletLight-Emitting Diodes Using a Strip-in-a-BarrierStructure," *Applied Optics,* vol. 59, no. 17, pp. 5276-5281, 2020.

[98] R. T. Velpula, B. Jain, H. Q. T. Bui, M. Tumuna, J. Jude, H. P. T. Nguyen, "Electron Blocking Layer Free AlGaN Deep-Ultraviolet Light Emitting Diodes," *Conference On Lasers and Electro Optics (CLEO),* pp. AF1I-3, 2020.

[99] H. P. T. Nguyen, M. Djavid, S. Y. Woo, X. Liu, A. T. Connie, S. Sadaf, Q. Wang, G. A. Botton, I. Shih, and Z. Mi, "Engineering the carrier dynamics of InGaN nanowire white light-emitting diodes by distributed p-AlGaN electron blocking layers," *Scientific Reports,* vol. 5, no. 1, pp. 1-7, 2015.

[100] C. S. Xia, ZM S. Li, W. Lu, Z. H. Zhang, Y. Sheng, W. D. Hu, and L. W. Cheng, "Efficiency enhancement of blue InGaN/GaN light-emitting diodes with an

AlGaN-GaN-AlGaN electron blocking layer," *Journal of Applied Physics*, vol. 111, no. 9, p. 094503, 2012.

[101] C. Chu, K. Tian, J. Che, H. Shao, J. Kou, Y. Zhang, Y. Li, M. Wang, Y. Zhu, and Z.-H. Zhang, "On the origin of enhanced hole injection for AlGaN-based deep ultraviolet light-emitting diodes with AlN insertion layer in p-electron blocking layer," *Optics Express*, vol. 27, no. 12, pp. A620-A628, 2019.

[102] E. Schubert, W. Grieshaber, and I. Goepfert, "Enhancement of deep acceptor activation in semiconductors by superlattice doping," *Applied Physics Letters*, vol. 69, no. 24, pp. 3737-3739, 1996.

[103] P. Kozodoy, M. Hansen, S. P. DenBaars, and U. K. Mishra, "Enhanced Mg doping efficiency in Al 0.2 Ga 0.8 N/GaN superlattices," *Applied Physics Letters*, vol. 74, no. 24, pp. 3681-3683, 1999.

[104] A. Saxler, W. Mitchel, P. Kung, and M. Razeghi, "Aluminum gallium nitride short-period superlattices doped with magnesium," *Applied Physics Letters*, vol. 74, no. 14, pp. 2023-2025, 1999.

[105] I. Goepfert, E. Schubert, A. Osinsky, and P. Norris, "Demonstration of efficient p-type doping in AlxGa1–xN/GaN superlattice structures," *Electronics Letters*, vol. 35, no. 13, pp. 1109-1111, 1999.

[106] S. Wu, V. Adivarahan, M. Shatalov, A. Chitnis, W.-H. Sun, and M. A. Khan, "Micro-pixel design milliwatt power 254 nm emission light emitting diodes," *Japanese Journal of Applied Physics*, vol. 43, no. 8A, p. L1035, 2004.

[107] I. Soloshenko, V. Y. Bazhenov, V. Khomich, V. Tsiolko, and N. Potapchenko, "Comparative research of efficiency of water decontamination by UV radiation of cold hollow cathode discharge plasma versus that of low-and medium-pressure mercury lamps," *IEEE Transactions on Plasma Science*, vol. 34, no. 4, pp. 1365-1369, 2006.

[108] J. Piprek, "Nitride semiconductor devices: principles and simulation," John Wiley & Sons 2007.

[109] C. Coughlan, S. Schulz, M. A. Caro, and E. P. O'Reilly, "Band gap bowing and optical polarization switching in Al Ga N alloys," *Physica Status Solidi (b)*, vol. 252, no. 5, pp. 879-884, 2015.

[110] S. Chuang and C. Chang, "k· p method for strained wurtzite semiconductors," *Physical Review B*, vol. 54, no. 4, p. 2491, 1996.

[111] J. Yun, J.-I. Shim, and H. Hirayama, "Analysis of efficiency droop in 280-nm AlGaN multiple-quantum-well light-emitting diodes based on carrier rate equation," *Applied Physics Express*, vol. 8, no. 2, p. 022104, 2015.

[112] K. Nam, M. Nakarmi, J. Li, J. Lin, and H. Jiang, "Mg acceptor level in AlN probed by deep ultraviolet photoluminescence," *Applied Physics Letters*, vol. 83, no. 5, pp. 878-880, 2003.

[113] M. Nakarmi, N. Nepal, J. Lin, and H. Jiang, "Photoluminescence studies of impurity transitions in Mg-doped AlGaN alloys," *Applied Physics Letters*, vol. 94, no. 9, p. 091903, 2009.

[114] R. Collazo, S. Mita, J. Xie, A. Rice, J. Tweedie, R. Dalmau, and Z. Sitar, "Progress on n-type doping of AlGaN alloys on AlN single crystal substrates for UV optoelectronic applications," *Physica Status Solidi (c)*, vol. 8, no. 7-8, pp. 2031-2033, 2011.

[115] V. Fiorentini, F. Bernardini, and O. Ambacher, "Evidence for nonlinear macroscopic polarization in III–V nitride alloy heterostructures," *Applied Physics Letters*, vol. 80, no. 7, pp. 1204-1206, 2002.

[116] S. Heikman, S. Keller, Y. Wu, J. S. Speck, S. P. DenBaars, and U. K. Mishra, "Polarization effects in AlGaN/GaN and GaN/AlGaN/GaN heterostructures," *Journal of Applied Physics*, vol. 93, no. 12, pp. 10114-10118, 2003.

[117] B. Cheng, S. Choi, J. E. Northrup, Z. Yang, C. Knollenberg, M. Teepe, T. Wunderer, C. L. Chua, and N. M. Johnson, "Enhanced vertical and lateral hole transport in high aluminum-containing AlGaN for deep ultraviolet light emitters," *Applied Physics Letters*, vol. 102, no. 23, p. 231106, 2013.

[118] S. Nakamura, "InGaN multiquantum-well-structure laser diodes with GaN-AlGaN modulation-doped strained-layer superlattices," *IEEE Journal of Selected Topics in Quantum Electronics*, vol. 4, no. 3, pp. 483-489, 1998.

[119] Z.-H. Zhang, W. Liu, Z. Ju, S. T. Tan, Y. Ji, Z. Kyaw, X. Zhang, L. Wang, X. W. Sun, and H. V. Demir, "Self-screening of the quantum confined Stark effect by the polarization induced bulk charges in the quantum barriers," *Applied Physics Letters*, vol. 104, no. 24, p. 243501, 2014.

[120] R. K. Mondal, V. Chatterjee, S. Prasad, and S. Pal, "Suppression of efficiency droop in AlGaN based deep UV LEDs using double side graded electron blocking layer," *Semiconductor Science and Technology*, vol. 35, no. 5, p. 055031, 2020.

[121] N. Maeda and H. Hirayama, "Realization of high-efficiency deep-UV LEDs using transparent p-AlGaN contact layer," *Physica Status Solidi (c)*, vol. 10, no. 11, pp. 1521-1524, 2013.

[122] B. So, J. Kim, E. Shin, T. Kwak, T. Kim, and O. Nam, "Efficiency Improvement of Deep-Ultraviolet Light Emitting Diodes with Gradient Electron Blocking Layers," *Physica Status Solidi (a),* vol. 215, no. 10, p. 1700677, 2018.

[123] J. Lang, F. J. Xu, W. K. Ge, B. Y. Liu, N. Zhang, Y. H. Sun, J. M. Wang, M. X. Wang, N. Xie, X. Z. Fang, and X. N. Kang, "Greatly enhanced performance of AlGaN-based deep ultraviolet light emitting diodes by introducing a polarization modulated electron blocking layer," *Optics Express,* vol. 27, no. 20, pp. A1458-A1466, 2019.

[124] Y.-K. Kuo, F.-M. Chen, B.-C. Lin, J.-Y. Chang, Y.-H. Shih, and H.-C. Kuo, "Simulation and experimental study on barrier thickness of superlattice electron blocking layer in near-ultraviolet light-emitting diodes," *IEEE Journal of Quantum Electronics,* vol. 52, no. 8, pp. 1-6, 2016.

[125] B. Jain, R. T. Velpula, S. Velpula, H.-D. Nguyen, and H. P. T. Nguyen, "Enhanced hole transport in AlGaN deep ultraviolet light-emitting diodes using a double-sided step graded superlattice electron blocking layer," *Journal of the Optical Society of America B,* vol. 37, no. 9, pp. 2564-2569, 2020.

[126] B. So, J. Kim, T. Kwak, T. Kim, J. Lee, U. Choi, and O. Nam, "Improved carrier injection of AlGaN-based deep ultraviolet light emitting diodes with graded superlattice electron blocking layers," *RSC Advances,* vol. 8, no. 62, pp. 35528-35533, 2018.

[127] R. T. Velpula, B. Jain, S. Velpula, H.-D. Nguyen, and H. P. T. Nguyen, "High-performance electron-blocking-layer-free deep ultraviolet light-emitting diodes implementing a strip-in-a-barrier structure," *Optics Letters,* vol. 45, no. 18, pp. 5125-5128, 2020.

[128] L. He, W. Zhao, K. Zhang, C. He, H. Wu, N. Liu, W. Song, Z. Chen, and S. Li, "Performance enhancement of AlGaN-based 365 nm ultraviolet light-emitting diodes with a band-engineering last quantum barrier," *Optics Letters,* vol. 43, no. 3, pp. 515-518, 2018.

[129] R. T. Velpula, B. Jain, H. Q. T. Bui, F. M. Shakiba, J. Jude, M. Tumuna, H.-D. Nguyen, T. R. Lenka, and H. P. T. Nguyen, "Improving carrier transport in AlGaN deep-ultraviolet light-emitting diodes using a strip-in-a-barrier structure," *Applied Optics,* vol. 59, no. 17, pp. 5276-5281, 2020.

[130] J. Yan, J. Wang, Y. Zhang, P. Cong, L. Sun, Y. Tian, C. Zhao, and J. Li, "AlGaN-based deep-ultraviolet light-emitting diodes grown on high-quality AlN template using MOVPE," *Journal of Crystal Growth,* vol. 414, pp. 254-257, 2015.

[131] Y. P. Varshni, "Temperature dependence of the energy gap in semiconductors," *Physica,* vol. 34, no. 1, pp. 149-154, 1967.

[132] X. Zhang, T. Taliercio, S. Kolliakos, and P. Lefebvre, "Influence of electron-phonon interaction on the optical properties of III nitride semiconductors," *Journal of Physics: Condensed Matter,* vol. 13, no. 32, p. 7053, 2001.

[133] M. Kuball, "Raman spectroscopy of GaN, AlGaN and AlN for process and growth monitoring/control," *Surface and Interface Analysis: An International Journal devoted to the development and application of techniques for the analysis of surfaces, interfaces and thin films,* vol. 31, no. 10, pp. 987-999, 2001.

[134] M. Mora-Ramos and L. Gaggero-Sager, "Electron-optical-phonon scattering rates in AlGaN/GaN-based single heterostructures," *Physica Status Solidi (c),* vol. 2, no. 8, pp. 3002-3005, 2005.

[135] Y. A. Yin, N. Wang, G. Fan, and Y. Zhang, "Investigation of AlGaN-based deep-ultraviolet light-emitting diodes with composition-varying AlGaN multilayer barriers," *Superlattices and Microstructures,* vol. 76, pp. 149-155, 2014.

[136] H. Hirayama, S. Fujikawa, N. Noguchi, J. Norimatsu, T. Takano, K. Tsubaki, and N. Kamata, "222–282 nm AlGaN and InAlGaN-based deep-UV LEDs fabricated on high-quality AlN on sapphire," *Physica Status Solidi (a),* vol. 206, no. 6, pp. 1176-1182, 2009.

[137] Y. Li, S. Chen, W. Tian, Z. Wu, Y. Fang, J. Dai, and C. Chen, "Advantages of AlGaN-based 310-nm UV light-emitting diodes with Al content graded AlGaN electron blocking layers," *IEEE Photonics Journal,* vol. 5, no. 4, pp. 8200309-8200309, 2013.

[138] Z.-H. Zhang, S.-W. H. Chen, C. Chu, K. Tian, M. Fang, Y. Zhang, W. Bi, and H.-C. Kuo, "Nearly efficiency-droop-free AlGaN-based ultraviolet light-emitting diodes with a specifically designed superlattice p-type electron blocking layer for high mg doping efficiency," *Nanoscale Research Letters,* vol. 13, no. 1, p. 122, 2018.

[139] B. M. Cheng Liu, Jing Zhang, "AlGaN-Delta-GaN Quantum Well for DUV LEDs," *Photonics,* vol. 7, no. 4, p. 13, 2020.

[140] Z. Ren, Y. Lu, H.-H. Yao, H. Sun, C.-H. Liao, J. Dai, C. Chen, J. H. Ryou, J. Yan, J. Wang, and J. Li, "III-nitride deep UV LED without electron blocking layer," *IEEE Photonics Journal,* vol. 11, no. 2, pp. 1-11, 2019.

[141] R. T. Velpula, B. Jain, H. Q. T. Bui, T. T. Pham, H.-D. Nguyen, T. R. Lenka, and H. P. T. Nguyen, "Numerical investigation on the device performance of electron

blocking layer free AlInN nanowire deep ultraviolet light-emitting diodes," *Optical Materials Express,* vol. 10, no. 2, pp. 472-483, 2020.

[142] B. Jain, R. T. Velpula, H.Q.T. Bui, H. D. Nguyen, T. R. Lenka, T. K. Nguyen, and H. P. T. Nguyen, "High performance electron blocking layer-free InGaN/GaN nanowire white-light-emitting diodes," *Optics Express,* vol. 28, no. 1, pp. 665-675, 2020.

[143] D. Caughey and R. Thomas, "Carrier mobilities in silicon empirically related to doping and field," *Proceedings of the IEEE,* vol. 55, no. 12, pp. 2192-2193, 1967.

[144] I. Vurgaftman and J. n. Meyer, "Band parameters for nitrogen-containing semiconductors," *Journal of Applied Physics,* vol. 94, no. 6, pp. 3675-3696, 2003.

[145] X. Ji, J. Yan, Y. Guo, L. Sun, T. Wei, Y. Zhang, J. Wang, F. Yang, and J. Li, "Tailoring of energy band in electron-blocking structure enhancing the efficiency of AlGaN-based deep ultraviolet light-emitting diodes," *IEEE Photonics Journal,* vol. 8, no. 3, pp. 1-7, 2016.

[146] B. K. SaifAddin, A. S. Almogbel, C. J. Zollner, F. Wu, B. Bonef, M. Iza, S. Nakamura, S. P. DenBaars, and J. S. Speck, "AlGaN deep-ultraviolet light-emitting diodes grown on SiC substrates," *ACS Photonics,* vol. 7, no. 3, pp. 554-561, 2020.

[147] J. Hu, J. Zhang, Y. Zhang, H. Zhang, H. Long, Q. Chen, M. Shan, S. Du, J. Dai, and C. Chen, "Enhanced performance of AlGaN-based deep ultraviolet light-emitting diodes with chirped superlattice electron deceleration layer," *Nanoscale Research Letters,* vol. 14, no. 1, pp. 1-8, 2019.

[148] R. Ni, C.-C. Chuo, K. Yang, Y. Ai, L. Zhang, Z. Cheng, Z. Liu, L. Jia, and Y. Zhang, "AlGaN-based ultraviolet light-emitting diode on high-temperature annealed sputtered AlN template," *Journal of Alloys and Compounds,* vol. 794, pp. 8-12, 2019.

[149] V. Jmerik, T. V. Shubina, A. M. Mizerov, K. G. Belyaev, A. V. Sakharov, M. V. Zamoryanskaya, A. A. Sitnikova, V. Y. Davydov, P. S. Kop'ev, E. V. Lutsenko, and N. V. Rzheutskii, "AlGaN quantum well structures for deep-UV LEDs grown by plasma-assisted MBE using sub-monolayer digital-alloying technique," *Journal of Crystal Growth,* vol. 311, no. 7, pp. 2080-2083, 2009.

[150] Y. Liao, C. Thomidis, C.-k. Kao, and T. D. Moustakas, "AlGaN based deep ultraviolet light emitting diodes with high internal quantum efficiency grown by molecular beam epitaxy," *Applied Physics Letters,* vol. 98, no. 8, p. 081110, 2011.

[151] X. Hai, R. Rashid, S. Sadaf, Z. Mi, and S. Zhao, "Effect of low hole mobility on the efficiency droop of AlGaN nanowire deep ultraviolet light emitting diodes," *Applied Physics Letters,* vol. 114, no. 10, p. 101104, 2019.

[152] K. Nam, J. Li, M. Nakarmi, J. Lin, and H. Jiang, "Unique optical properties of AlGaN alloys and related ultraviolet emitters," *Applied Physics Letters,* vol. 84, no. 25, pp. 5264-5266, 2004.

[153] M. Yamada, T. Mitani, Y. Narukawa, S. Shioji, I. Niki, S. Sonobe, K. Deguchi, M. Sano, and T. Mukai, "InGaN-based near-ultraviolet and blue-light-emitting diodes with high external quantum efficiency using a patterned sapphire substrate and a mesh electrode," *Japanese Journal of Applied Physics,* vol. 41, no. 12B, p. L1431, 2002.

[154] T. Kolbe, A. Knauer, C. Chua, Z. Yang, S. Einfeldt, P. Vogt, N. M. Johnson, M. Weyers, and M. Kneissl, "Optical polarization characteristics of ultraviolet (In)(Al) GaN multiple quantum well light emitting diodes," *Applied Physics Letters,* vol. 97, no. 17, p. 171105, 2010.

[155] M. Kneissl, T. Kolbe, C. Chua, V. Kueller, N. Lobo, J. Stellmach, A. Knauer, H. Rodriguez, S. Einfeldt, Z. Yang, and N. M. Johnson, "Advances in group III-nitride-based deep UV light-emitting diode technology," *Semiconductor Science and Technology,* vol. 26, no. 1, p. 014036, 2010.

[156] C. Lee, B. Cheng, Y. Lee, H. Kuo, T. Lu, and S. Wang, "Output power enhancement of vertical-injection ultraviolet light-emitting diodes by GaN-free and surface roughness structures," *Electrochemical and Solid-State Letters,* vol. 12, no. 2, pp. H44-H46, 2009.

[157] Y.-J. Lee, T. C. Hsu, H. C. Kuo, S.C. Wang, Y. L. Yang, S. N. Yen, Y. T. Chu, Y. J. Shen, M. H. Hsieh, M. J. Jou, and B. J. Lee, "Improvement in light-output efficiency of near-ultraviolet InGaN–GaN LEDs fabricated on stripe patterned sapphire substrates," *Materials Science and Engineering: B,* vol. 122, no. 3, pp. 184-187, 2005.

[158] M. Djavid, X. Liu, and Z. Mi, "Improvement of the light extraction efficiency of GaN-based LEDs using rolled-up nanotube arrays," *Optics Express,* vol. 22, no. 107, pp. A1680-A1686, 2014.

[159] J. Shakya, K. Kim, J. Lin, and H. Jiang, "Enhanced light extraction in III-nitride ultraviolet photonic crystal light-emitting diodes," *Applied Physics Letters,* vol. 85, no. 1, pp. 142-144, 2004.

[160] K. H. Lee, H. J. Park, S. H. Kim, M. Asadirad, Y.-T. Moon, J. S. Kwak, and J.-H. Ryou, "Light-extraction efficiency control in AlGaN-based deep-ultraviolet flip-chip light-emitting diodes: a comparison to InGaN-based visible flip-chip light-emitting diodes," *Optics Express,* vol. 23, no. 16, pp. 20340-20349, 2015.

[161] Q. Wang, A. T. Connie, H. P. T. Nguyen, M. G. Kibria, S. Zhao, S. Sharif, I. Shih, and Z. Mi, "Highly efficient, spectrally pure 340 nm ultraviolet emission from AlxGa1− xN nanowire based light emitting diodes," *Nanotechnology,* vol. 24, no. 34, p. 345201, 2013.

[162] S. Zhao, M. Djavid, and Z. Mi, "Surface emitting, high efficiency near-vacuum ultraviolet light source with aluminum nitride nanowires monolithically grown on silicon," *Nano Letters,* vol. 15, no. 10, pp. 7006-7009, 2015.

[163] S. Zhao, S. Sadaf, S. Vanka, Y. Wang, R. Rashid, and Z. Mi, "Sub-milliwatt AlGaN nanowire tunnel junction deep ultraviolet light emitting diodes on silicon operating at 242 nm," *Applied Physics Letters,* vol. 109, no. 20, p. 201106, 2016.

[164] H. Sun, S. Mitra, R. C. Subedi, Y. Zhang, W. Guo, J. Ye, M. K. Shakfa, T. K. Ng, B. S. Ooi, I. S. Roqan, and Z. Zhang, "Unambiguously enhanced ultraviolet luminescence of AlGaN wavy quantum well structures grown on large misoriented sapphire substrate," *Advanced Functional Materials,* vol. 29, no. 48, p. 1905445, 2019.

[165] Z. Ren, H. Yu, Z. Liu, D. Wang, C. Xing, H. Zhang, C. Huang, S. Long, and H. Sun, "Band engineering of III-nitride-based deep-ultraviolet light-emitting diodes: A review," *Journal of Physics D: Applied Physics,* vol. 53, no. 7, p. 073002, 2019.

[166] M. Djavid and Z. Mi, "Enhancing the light extraction efficiency of AlGaN deep ultraviolet light emitting diodes by using nanowire structures," *Applied Physics Letters,* vol. 108, no. 5, p. 051102, 2016.

[167] R. T. Velpula, B. Jain, M. R. Philip, H. D. Nguyen, R. Wang, and H. P. T. Nguyen, "epitaxial Growth and characterization of Alinn-Based core-Shell nanowire Light emitting Diodes operating in the Ultraviolet Spectrum," *Scientific Reports,* vol. 10, no. 1, pp. 1-10, 2020.

[168] Y. H. Ra, R. T. Rashid, X. Liu, J. Lee, and Z. Mi, "Scalable nanowire photonic crystals: Molding the light emission of InGaN," *Advanced Functional Materials,* vol. 27, no. 38, p. 1702364, 2017.

[169] P. Du, L. Rao, Y. Liu, and Z. Cheng, "Enhancing the light extraction efficiency of AlGaN LED with nanowire photonic crystal and graphene transparent electrode," *Superlattices and Microstructures,* vol. 133, p. 106216, 2019.

[170] P. Zhao, L. Han, M. R. McGoogan, and H. Zhao, "Analysis of TM mode light extraction efficiency enhancement for deep ultraviolet AlGaN quantum wells light-emitting diodes with III-nitride micro-domes," *Optical Materials Express,* vol. 2, no. 10, pp. 1397-1406, 2012.

[171] M. Djavid, "High Efficiency Nanowire-based Phosphor-free White and Deep Ultraviolet Light Sources," *McGill University Libraries*, 2016.

[172] W. Guo, M. Zhang, P. Bhattacharya, and J. Heo, "Auger Recombination in III-Nitride Nanowires and Its Effect on Nanowire Light-Emitting Diode Characteristics," *Nano Letters*, vol. 11, no. 4, pp. 1434-1438, 2011.

[173] H. P. T. Nguyen, K. Cui, S. Zhang, M. Djavid, A. Korinek, G. A. Botton, and Z. Mi, "Controlling Electron Overflow in Phosphor-Free InGaN/GaN Nanowire White Light-Emitting Diodes," *Nano Letters*, vol. 12, no. 3, pp. 1317–1323, 2012.

[174] H. P. T. Nguyen, S. Zhang, K. Cui, X. Han, S. Fathololoumi, M. Couillard, G. A. Botton, and Z. Mi, "p-Type Modulation Doped InGaN/GaN Dot-in-a-Wire White-Light-Emitting Diodes Monolithically Grown on Si(111)," *Nano Letters*, vol. 11, no. 5, pp. 1919-1924, 2011.

[175] R. T. Velpula, B. Jain, H. Q. T. Bui, and H. P. T. Nguyen, "Full-Color III-Nitride Nanowire Light-Emitting Diodes," *Journal of Advanced Engineering and Computation*, vol. 3, no. 4, p. 38, 2019.

[176] P. Renwick, H. Tang, and J. Bai, "Reduced longitudinal optical phonon-exciton interaction in InGaN/GaN nanorod structures," *Applied Physics Letters*, vol. 100, 2012.

[177] B. Janjua, H. Sun, C. Zhao, D. H. Anjum, D. Priante, A. A. Alhamoud, F. Wu, X. Li, A. M. Albadri, A. Y. Alyamani, and M. M. El-Desouki, "Droop-free Al x Ga 1-x N/Al y Ga 1-y N quantum-disks-in-nanowires ultraviolet LED emitting at 337 nm on metal/silicon substrates," *Optics Express*, vol. 25, no. 2, pp. 1381-1390, 2017.

[178] D. Priante, M. Tangi, J. W. Min, N. Alfaraj, J. W. Liang, H. Sun, H. H. Alhashim, X. Li, A. M. Albadri, A. Y. Alyamani, and T. K. Ng, "Enhanced electro-optic performance of surface-treated nanowires: origin and mechanism of nanoscale current injection for reliable ultraviolet light-emitting diodes," *Optical Materials Express*, vol. 9, no. 1, pp. 203-215, 2019.

[179] D. M. Sullivan, *Electromagnetic simulation using the FDTD method*. John Wiley & Sons, 2013.

[180] W. Choi, Q. H. Park, D. Kim, H. Jeon, C. Sone, and Y. Park, "FDTD simulation for light extraction in a GaN-based LED," *Journal of the Korean Physical Society*, vol. 49, no. 3, pp. 877-880, 2006.

[181] L. Zhang, N. Alexopoulos, D. Sievenpiper, and E. Yablonovitch, "An efficient finite-element method for the analysis of photonic band-gap materials," in *IEEE MTTS Int. Microw. Symp.*, 1999, vol. 4, pp. 1703-1706.

[182] X. Liu, B. H. Le, S. Y. Woo, S. Zhao, A. Pofelski, G. A. Botton, and Z. Mi, "Selective area epitaxy of AlGaN nanowire arrays across nearly the entire compositional range for deep ultraviolet photonics," *Optics Express*, vol. 25, no. 24, pp. 30494-30502, 2017.

[183] R. Wang, Y.-H. Ra, Y. Wu, S. Zhao, H. P. T. Nguyen, I. Shih, and Z. Mi, "Tunable, full-color nanowire light emitting diode arrays monolithically integrated on Si and sapphire," *Gallium Nitride Materials and Devices XI*, vol. 9748, pp. 97481S-97481S-9, 2016.

[184] K. Kishino, T. Hoshino, S. Ishizawa, and A. Kikuchi, "Selective-area growth of GaN nanocolumns on titanium-mask-patterned silicon (111) substrates by RF-plasma-assisted molecular-beam epitaxy," *Electronics Letters*, vol. 44, no. 13, pp. 819-U55, 2008.

[185] S. Ishizawa, K. Kishino, and A. Kikuchi, "Selective-area growth of GaN nanocolumns on Si(111) substrates using nitrided al nanopatterns by rf-plasma-assisted molecular-beam epitaxy," *Applied Physics Express*, vol. 1, no. 1, 2008.

[186] S. D. Gedney, "An anisotropic perfectly matched layer-absorbing medium for the truncation of FDTD lattices," *IEEE Transactions on Antennas and Propagation*, vol. 44, no. 12, pp. 1630-1639, 1996.

[187] A. B. Djurišić and E. H. Li, "Modeling the optical constants of hexagonal GaN, InN, and AlN," *Journal of Applied Physics*, vol. 85, no. 5, pp. 2848-2853, 1999.

[188] D. Brunner, H. Angerer, E. Bustarret, F. Freudenberg, R. Höpler, R. Dimitrov, O. Ambacher, and M. Stutzmann, "Optical constants of epitaxial AlGaN films and their temperature dependence," *Journal of Applied Physics*, vol. 82, no. 10, pp. 5090-5096, 1997.

[189] P. Zhu, "Frustrated total internal reflection in organic light-emitting diodes employing sphere cavity embedded in polystyrene," *Journal of Optics*, vol. 18, no. 2, p. 025403, 2016.

[190] A. David, "High-efficiency GaN-based light-emitting diodes: light extraction by photonic crystals and microcavities," Ecole Polytechnique X, 2006.

[191] S. G. Johnson and J. D. Joannopoulos, "Block-iterative frequency-domain methods for Maxwell's equations in a planewave basis," *Optics Express*, vol. 8, no. 3, pp. 173-190, 2001.

[192] R. Lin, S. V. Galan, H. Sun, Y. Hu, M. S. Alias, B. Janjua, T. K. Ng, B. S. Ooi, and X. Li, "Tapering-induced enhancement of light extraction efficiency of nanowire

deep ultraviolet LED by theoretical simulations," *Photonics Research,* vol. 6, no. 5, pp. 457-462, 2018.

[193] F. Pan, "Experimental and simulation study of resistive switches for memory applications," UC Berkeley, 2012.

[194] S. Bertolazzi, P. Bondavalli, S. Roche, T. San, S.-Y. Choi, L. Colombo, F. Bonaccorso, and P. Samori, "Nonvolatile Memories Based on Graphene and Related 2D Materials," *Advanced Materials,* vol. 31, no. 10, p. 1806663, 2019.

[195] K. Kinoshita, K. Tsunoda, Y. Sato, H. Noshiro, S. Yagaki, M. Aoki, and Y. Sugiyama, "Reduction in the reset current in a resistive random access memory consisting of Ni O x brought about by reducing a parasitic capacitance," *Applied Physics Letters,* vol. 93, no. 3, p. 033506, 2008.

[196] H.-S. P. Wong, H.-Y. Lee, S. Yu, Y.-S. Chen, Y. Wu, P.-S. Chen, B. Lee, F. T. Chen, and M.-J. Tsai, "Metal–oxide RRAM," *Proceedings of the IEEE,* vol. 100, no. 6, pp. 1951-1970, 2012.

[197] T. Hickmott, "Low-frequency negative resistance in thin anodic oxide films," *Journal of Applied Physics,* vol. 33, no. 9, pp. 2669-2682, 1962.

[198] J. Gibbons and W. Beadle, "Switching properties of thin NiO films," *Solid-State Electronics,* vol. 7, no. 11, pp. 785-790, 1964.

[199] I. G. Baek, M. S. Lee, S. Seo, M. J. Lee, D. H. Seo, D. S. Suh, J. C. Park, S. O. Park, H. S. Kim, I. K. Yoo, and U. I. Chung, "Highly scalable nonvolatile resistive memory using simple binary oxide driven by asymmetric unipolar voltage pulses," in *IEDM Technical Digest. IEEE International Electron Devices Meeting, 2004.*, 2004: IEEE, pp. 587-590.

[200] S. Seo, M. J. Lee, D. H. Seo, E. J. Jeoung, D. S. Suh, Y. S. Joung, I. K. Yoo, I. R. Hwang, S. H. Kim, I. S. Byun, and J. S. Kim, "Reproducible resistance switching in polycrystalline NiO films," *Applied Physics Letters,* vol. 85, no. 23, pp. 5655-5657, 2004.

[201] B. Choi, D. S. Jeong, S. K. Kim, C. Rohde, S. Choi, J. H. Oh, H. J. Kim, C. S. Hwang, K. Szot, R. Waser, and B. Reichenberg, "Resistive switching mechanism of TiO 2 thin films grown by atomic-layer deposition," *Journal of Applied Physics,* vol. 98, no. 3, p. 033715, 2005.

[202] A. Chen, S. Haddad, Y. C. Wu, T. N. Fang, Z. Lan, S. Avanzino, S. Pangrle, M. Buynoski, M. Rathor, W. Cai, and N. Tripsas, "Non-volatile resistive switching for advanced memory applications," in *IEEE International Electron Devices Meeting, 2005. IEDM Technical Digest.*, 2005: IEEE, pp. 746-749.

[203] C.-Y. Lin, C.-Y. Wu, C.-Y. Wu, T.-Y. Tseng, and C. Hu, "Modified resistive switching behavior of zr o 2 memory films based on the interface layer formed by using ti top electrode," *Journal of Applied Physics*, vol. 102, no. 9, p. 094101, 2007.

[204] N. Xu, L. Liu, X. Sun, X. Liu, D. Han, Y. Wang, R. Han, J. Kang, and B. Yu, "Characteristics and mechanism of conduction/set process in Ti N⁄ Zn O⁄ Pt resistance switching random-access memories," *Applied Physics Letters*, vol. 92, no. 23, p. 232112, 2008.

[205] H. Y. Lee, P. S. Chen, T. Y. Wu, Y. S. Chen, C. C. Wang, P. J. Tzeng, C. H. Lin, F. Chen, C. H. Lien, and M-J. Tsai, "Low power and high speed bipolar switching with a thin reactive Ti buffer layer in robust HfO2 based RRAM," in *2008 IEEE International Electron Devices Meeting*, 2008: IEEE, pp. 1-4.

[206] B. Jain, C.-S. Huang, D. Misra, K. Tapily, R. D. Clark, S. Consiglio, C. S. Wajda, and G. J. Leusink, "Multilevel resistive switching in Hf-based RRAM," *ECS Transactions*, vol. 89, no. 3, p. 39, 2019.

[207] Z. Wei, Y. Kanzawa, K. Arita, Y. Katoh, K. Kawai, S. Muraoka, S. Mitani, S. Fujii, K. Katayama, M. Iijima, and T. Mikawa, "Highly reliable TaOx ReRAM and direct evidence of redox reaction mechanism," in *2008 IEEE International Electron Devices Meeting*, 2008: IEEE, pp. 1-4.

[208] W. Kim, S. Il Park, Z. Zhang, Y. Y. Liauw, D. Sekar, H. S. P. Wong, and S. S. Wong. "Forming-free nitrogen-doped AlO X RRAM with sub-μA programming current," in *2011 Symposium on VLSI Technology-Digest of Technical Papers*, 2011: IEEE, pp. 22-23.

[209] F. Zahoor, T. Z. A. Zulkifli, and F. A. Khanday, "Resistive random access memory (RRAM): an overview of materials, switching mechanism, performance, multilevel cell (MLC) storage, modeling, and applications," *Nanoscale Research Letters*, vol. 15, no. 1, pp. 1-26, 2020.

[210] C.-Y. Lin, C.-Y. Wu, C.-Y. Wu, T.-C. Lee, F.-L. Yang, C. Hu, and T.-Y. Tseng "Effect of Top Electrode Material on Resistive Switching Properties of $\hbox {ZrO} _ {2} $ Film Memory Devices," *IEEE Electron Device Letters*, vol. 28, no. 5, pp. 366-368, 2007.

[211] W.-Y. Chang, Y.-C. Lai, T.-B. Wu, S.-F. Wang, F. Chen, and M.-J. Tsai, "Unipolar resistive switching characteristics of ZnO thin films for nonvolatile memory applications," *Applied Physics Letters*, vol. 92, no. 2, p. 022110, 2008.

[212] S. Lee, S. C. Chae, S. H. Chang, J. S. Lee, S. Seo, B. Kahng, and T. W. Noh, "Scaling behaviors of reset voltages and currents in unipolar resistance switching," *Applied Physics Letters*, vol. 93, no. 21, p. 212105, 2008.

[213] L. Yang, C. Kuegeler, K. Szot, A. Ruediger, and R. Waser, "The influence of copper top electrodes on the resistive switching effect in TiO 2 thin films studied by conductive atomic force microscopy," *Applied Physics Letters,* vol. 95, no. 1, p. 013109, 2009.

[214] M. K. Yang, J.-W. Park, T. K. Ko, and J.-K. Lee, "Bipolar resistive switching behavior in Ti/MnO 2/Pt structure for nonvolatile memory devices," *Applied Physics Letters,* vol. 95, no. 4, p. 042105, 2009.

[215] Y. Wu, B. Lee, and H.-S. P. Wong, "Al_2O_3 based RRAM using atomic layer deposition (ALD) with RESET current," *IEEE Electron Device Letters,* vol. 31, no. 12, pp. 1449-1451, 2010.

[216] Y. Li, S. Long, M. Zhang, Q. Liu, L. Shao, S. Zhang, Y. Wang, Q. Zuo, S. Liu, and M. Liu, "Resistive switching properties of Au/ZrO_2/Ag structure for low-voltage nonvolatile memory applications," *IEEE Electron Device Letters,* vol. 31, no. 2, pp. 117-119, 2009.

[217] S. Yu, Y. Wu, Y. Chai, J. Provine, and H.-S. P. Wong, "Characterization of switching parameters and multilevel capability in HfO_x/AlO_x bi-layer RRAM devices," in *IEEE Proceedings of 2011 International Symposium on VLSI Technology, Systems and Applications*, pp. 1-2, 2011.

[218] F.-C. Chiu, P.-W. Li, and W.-Y. Chang, "Reliability characteristics and conduction mechanisms in resistive switching memory devices using ZnO thin films," *Nanoscale Research Letters,* vol. 7, no. 1, pp. 1-9, 2012.

[219] C.-W. Hsu, I-T. Wang, C.-L. Lo, M.-C. Chiang, W.-Y. Jang, C.-H. Lin, and T.-H. Hou, "Self-rectifying bipolar TaO x/TiO 2 RRAM with superior endurance over 10 12 cycles for 3D high-density storage-class memory," *Symposium on VLSI Technology*, pp. T166-T167, 2011

[220] H.-S. PhilipáWong, "Multi-level control of conductive nano-filament evolution in HfO 2 ReRAM by pulse-train operations," *Nanoscale,* vol. 6, no. 11, pp. 5698-5702, 2014.

[221] W. Chen, W. Lu, B. Long, Y. Li, D. Gilmer, G. Bersuker, S. Bhunia, and R. Jha "Switching characteristics of W/Zr/HfO2/TiN ReRAM devices for multi-level cell non-volatile memory applications," *Semiconductor Science and Technology,* vol. 30, no. 7, p. 075002, 2015.

[222] U. Chand, C.-Y. Huang, J.-H. Jieng, W.-Y. Jang, C.-H. Lin, and T.-Y. Tseng, "Suppression of endurance degradation by utilizing oxygen plasma treatment in HfO2 resistive switching memory," *Applied Physics Letters,* vol. 106, no. 15, p. 153502, 2015.

[223] W. Lu, W. Chen, Y. Li, and R. Jha, "Self current limiting MgO ReRAM devices for low-power non-volatile memory applications," *IEEE Journal on Emerging and Selected Topics in Circuits and Systems*, vol. 6, no. 2, pp. 163-170, 2016.

[224] M. Tsigkourakos, P. Bousoulas, V. Aslanidis, E. Skotadis, and D. Tsoukalas, "Ultra-Low Power Multilevel Switching with Enhanced Uniformity in Forming Free TiO2− x-Based RRAM with Embedded Pt Nanocrystals,"*Physica Status Solidi (a)*, vol. 214, no. 12, p. 1700570, 2017.

[225] S.-X. Chen, S.-P. Chang, W.-K. Hsieh, S.-J. Chang, and C.-C. Lin, "Highly stable ITO/Zn 2 TiO 4/Pt resistive random access memory and its application in two-bit-per-cell," *RSC Advances*, vol. 8, no. 32, pp. 17622-17628, 2018.

[226] Z. Shen, Y. Qi, I. Z. Mitrovic, C. Zhao, S. Hall, L. Yang, T. Luo, Y. Huang, and C. Zhao, "Effect of annealing temperature for Ni/AlOx/Pt RRAM devices fabricated with solution-based dielectric," *Micromachines*, vol. 10, no. 7, p. 446, 2019.

[227] Y. F. Qi, Z. J. Shen, C. Zhao, I. Z. Mitrovic, W. Y. Xu, E. G. Lim, L. Yang, J. H. He, T. Luo, Y. B. Huang, and C. Z. Zhao, "Resistive switching behavior of solution-processed AlOx and GO based RRAM at low temperature," *Solid-State Electronics*, vol. 168, p. 107735, 2020.

[228] J. J. Yang, M-X. Zhang, J. P. Strachan, F. Miao, M. D. Pickett, R. D. Kelley, G. M.-Ribeiro, and R. S. Williams, "High switching endurance in TaO x memristive devices," *Applied Physics Letters*, vol. 97, no. 23, p. 232102, 2010.

[229] J. J. Yang, M. D. Pickett, X. Li, D. A. Ohlberg, D. R. Stewart, and R. S. Williams, "Memristive switching mechanism for metal/oxide/metal nanodevices," *Nature Nanotechnology*, vol. 3, no. 7, pp. 429-433, 2008.

[230] C. Chen, Y. Yang, F. Zeng, and F. Pan, "Bipolar resistive switching in Cu/AlN/Pt nonvolatile memory device," *Applied Physics Letters*, vol. 97, no. 8, p. 083502, 2010.

[231] H.-D. Kim, H.-M. An, E. B. Lee, and T. G. Kim, "Stable bipolar resistive switching characteristics and resistive switching mechanisms observed in aluminum nitride-based ReRAM devices," *IEEE Transactions on Electron Devices*, vol. 58, no. 10, pp. 3566-3573, 2011.

[232] H.-D. Kim, H.-M. An, Y. Seo, and T. G. Kim, "Transparent resistive switching memory using ITO/AlN/ITO capacitors," *IEEE Electron Device Letters*, vol. 32, no. 8, pp. 1125-1127, 2011.

[233] B. J. Choi, J. J. Yang, M-X. Zhang, K. J. Norris, D. A. Ohlberg, N. P. Kobayashi, G. M.-Ribeiro, and R. S. Williams "Nitride memristors," *Applied Physics A*, vol. 109, no. 1, pp. 1-4, 2012.

[234] M. Marinella, J. E. Stevens, E. Longoria, and P. G. Kotula, "Resistive switching in aluminum nitride," in IEEE *70th Device Research Conference*, pp. 89-90, 2012.

[235] C. Chen, S. Gao, G. Tang, H. Fu, G. Wang, C. Song, F. Zeng, and F. Pan, "Effect of electrode materials on AlN-based bipolar and complementary resistive switching," *ACS Applied Materials & Interfaces*, vol. 5, no. 5, pp. 1793-1799, 2013.

[236] J. Zhang, Q. Zhang, H. Yang, H. Wu, J. Zhou, and L. Hu, "Bipolar resistive switching properties of AlN films deposited by plasma-enhanced atomic layer deposition," *Applied Surface Science*, vol. 315, pp. 110-115, 2014.

[237] Z. Zhang, B. Gao, Z. Fang, X. Wang, Y. Tang, J. Sohn, H. -S. P. Wong, S. S. Wong, and G.-Q. Lo "All-metal-nitride RRAM devices," *IEEE Electron Device Letters*, vol. 36, no. 1, pp. 29-31, 2014.

[238] R. Prakash and D. Kaur, "Bipolar resistive switching behavior in Cu/AlN/Pt structure for ReRAM application," *Vacuum*, vol. 143, pp. 102-105, 2017.

[239] Y. Duan, H. Gao, J. Guo, M. Yang, Z. Yu, X. Shen, S. Wu, Y. Sun, X. Ma, and Y. Yang, "Effect of nitrogen capture ability of quantum dots on resistive switching characteristics of AlN-based RRAM," *Applied Physics Letters*, vol. 118, no. 1, p. 013501, 2021.

[240] D. Manova, V. Dimitrova, W. Fukarek, and D. Karpuzov, "Investigation of dc-reactive magnetron-sputtered AlN thin films by electron microprobe analysis, X-ray photoelectron spectroscopy and polarised infra-red reflection," *Surface and Coatings Technology*, vol. 106, no. 2-3, pp. 205-208, 1998.

[241] Z.-L. Tseng, L.-C. Chen, W.-Y. Li, and S.-Y. Chu, "Resistive switching characteristics of sputtered AlN thin films," *Ceramics International*, vol. 42, no. 8, pp. 9496-9503, 2016.

[242] B. J. Choi, N. Ge, J. J. Yang, M.-X. Zhang, R. S. Williams, K. J. Norris, and N. P. Kobayashi "New materials for memristive switching," in *2014 IEEE International Symposium on Circuits and Systems (ISCAS)*, 2014: IEEE, pp. 2808-2811.

[243] K. Fu, H. Fu, X. Huang, T.-H. Yang, H. Chen, I. Baranowski, J. Montes, C. Yang, J. Zhou, and Y. Zhao, "Threshold switching and memory behaviors of epitaxially regrown GaN-on-GaN vertical p-n diodes with high temperature stability," *IEEE Electron Device Letters*, vol. 40, no. 3, pp. 375-378, 2019.

[244] C. Ho, J. D. Retamal, P. K. Yang, C. P. Lee, M. L. Tsai, C. F. Kang, and Jr-Hau He, "Transparent memory for harsh electronics," *Scientific Reports*, vol. 7, no. 1, pp. 1-6, 2017.

[245] A. Fantini, L. Goux, A. Redolfi, R. Degraeve, G. Kar, Y. Y. Chen, and M. Jurczak "Lateral and vertical scaling impact on statistical performances and reliability of 10nm TiN/Hf (Al) O/Hf/TiN RRAM devices," in *IEEE Symposium on VLSI Technology (VLSI-Technology): Digest of Technical Papers*, pp. 1-2, 2014.